NGU Report 2010.058

The mantle under Africa: An overview of global and regional tomography models, lithosphere thickness models and their effect on present-day and past dynamic topography

NGU
Norges geologiske undersøkelse
Geological Survey of Norway

Geological Survey of Norway
Postboks 6315 Sluppen
NO-7491 Trondheim, Norway
Tel.: 47 73 90 40 00
Telefax 47 73 92 16 20

REPORT

Report no.: 2010.058	ISSN 0800-3416	Grading: Confidential until 01.12.2012

Title:
The mantle under Africa: An overview of global and regional tomography models, lithosphere thickness models and their effect on present-day and past dynamic topography

Authors:
Bernhard Steinberger, Susanne Buiter, Sergei Medvedev, Joya Tetreault

Client:
Statoil

County:

Commune:

Map-sheet name (M=1:250.000)

Map-sheet no. and -name (M=1:50.000)

Deposit name and grid-reference:

Number of pages: 106 Price (NOK): 455,-
Map enclosures:

Fieldwork carried out:	Date of report:	Project no.:	Person responsible:
	10.11.2010	326100	BHeidbach

Summary:

The African plate is affected less by subduction than other plates and, as a consequence its surface experienced less subduction-related deformation while its mantle contains fewer subducted slabs. This region therefore appears suitable to study the effect of large-scale mantle density anomalies and flow on both present-day dynamic topography and past surface uplift and subsidence events. Dynamic topography quantifies the mantle component to Earth's surface topography and as such influences the formation of basins and natural resources. It is computed here from a mantle flow model with density variations inferred from seismic tomography and radial mantle viscosity variations. In order to assess the robustness of tomography features, we have compiled here a total of 18 models (13 whole-mantle and 5 upper mantle). We have also computed a weighted mean tomography model that gives a fit between dynamic topography and observation-based "residual topography" substantially better than any individual model. To better understand discrepancies between dynamic and residual topography we compute their correlations and ratios (1) regionally in caps of 30 degrees of arc and (2) spectrally as a function of spherical harmonic degree up until degree 31. We compare the observed correlation and ratio of geoid and residual topography with the values "expected" from a geodynamic model. Correlations between residual and dynamic topography are typically high in a region centred on northeastern Africa. Ratios tend to be higher in the oceans than the continent, indicating substantial lateral viscosity variations in the asthenosphere. We compute models of past dynamic topography by backward advection of density anomalies. Combining these with models of African plate motion, we compute uplift and subsidence of points moving with the plate. However, when interpreting these results it needs to be carefully considered at what depth the density anomalies that cause these uplift and subsidence are located. Results can only be considered if those density anomalies are not advected in or out of thermal boundary layers, such that the neglect of diffusion backward in time does not introduce a substantial error. To study the effects of including a deformable lithosphere with a pressure- and temperature-dependent rheology and a free surface, we apply pressures and velocities from the mantle flow computations at the base of a model lithosphere. Results indicate little deformation in the African basins, such that the treatment with a pure mantle flow code appears valid there.

Keywords: Africa	Tomography	Dynamic topography
Mantle-Lithosphere interaction	Sedimentary basins	

TABLE OF CONTENTS

1. INTRODUCTION

As any other continent, Africa's topography shows high and low areas of various ages (*Fig. 1*). But there are a number of intriguing aspects to Africa's topography. The East African Rift basin, for example, is an extensional feature, but this extension occurs on a continent that should to large degree be in compression as it is surrounded by mid-ocean ridges. Several other sedimentary basins, such as the Taoudeni, Murzuq, Kufrah and Congo basins, are long-lived, recording slow subsidence since the (Pre) Cambrian, but have no clear indications of basin-forming mechanisms (such as extensional faults). Similar anomalous behaviour of such large-scale intracratonic basins elsewhere has been explained by underlying old rifts (e.g. Michigan Basin on the North American plate), cooling after intrusion of dense material, slow extension of thick lithosphere, phase changes or mantle down-welling (mantle cold spots) (e.g., Middleton, 1989; Quinlan, 1987; Kaus et al., 2005; Armitage and Allen, 2010). The mechanisms proposed for the Congo Basin illustrate the ongoing debate nicely. The Congo Basin contains up to 9 km of unconformity-bounded sedimentary layers of Pre-Cambrian to Cenozoic ages (Daly et al., 1992). The older sediments may have been deposited in response to thermal contraction after a late Proterozoic rift event (Daly et al., 1992), but the upper 1-km thick sediment fill of Mesozoic-Cenozoic age cannot be linked to clear basin-forming processes (Giresse, 2005). Hartley and Allen (1994) have suggested that a downward dynamic force at the base of the lithosphere could explain the negative gravity anomaly over the basin and create the subsidence that allowed deposition of the uppermost sediments. The origin of this force is however an open question. Downey and Gurnis (2009) place it at relatively shallow depths and propose that the gravity and topography signal may be explained by an anomalous body within the lithosphere. Crosby et al. (2010) and Forte et al. (2010) invoke a downward mantle flow beneath the basin driven by small plumes rising up below the basin flanks. An alternative hypothesis by Burke and Gunnell (2008) suggests that the Congo Basin is only a relatively recent feature that came into existence at about 30 Ma as the area around the basin uplifted by several mainly non-volcanic swells. As many of the proposed mechanisms place (part of) the cause of basin subsidence in the mantle, insight into the mantle structure under Africa would help place first order constraints on the scenarios.

Several of the uplifted areas pose interesting questions related to the partitioning between lithosphere versus mantle support and the depth of magma source areas. Low seismic velocities beneath the Afar region appear to be linked to an extensive low-velocity anomaly at the core-mantle boundary (CMB) more than 45 degrees away by a tilted anomaly (Ritsema et al., 1999). It therefore appears that upward flow all the way from the lowermost mantle supplies heat to volcanoes in East Africa. In Northern Africa, links have been proposed between the volcanic centre of Darfur and the Afar hotspot (Ebinger and Sleep, 1998), but the recent debate seems to conclude that the Cenozoic volcanic centres of Tibesti, Hoggar and Darfur are probably all underlain by shallow mantle plumes (Wilson and Guiraud, 1992; Sebai et al., 2006; Montagner et al., 2007). Volcanism in the Cameroon Volcanic Line is possibly consistent with a model invoking edge-flow convection along the northern boundary of the Congo Craton lithosphere (Reusch et al., 2010). The High Atlas Mountains have a high mean elevation of 2600 m with the highest peak at 4165 m, but this high elevation is underlain by an average thickness crust of not more than 40 km (Wigger et al., 1992; Ayarza et al., 2005) which is only a few kilometres thicker than the crust of the surrounding areas. This lack of a mountain root indicates that the High Atlas Mountains are isostatically undercompensated. In combination with indications for a thin lithosphere (Seber et al., 1996; Teixell et al., 2005), this has raised the strongly debated question of how the elevation of the High Atlas Mountains is maintained. At least part of the uplift is caused by inversion by shortening of a failed rift, but several authors have argued for an additional contribution from

a warm mantle source (Teixell et al., 2003; Missenard et al., 2006). Therefore, also for these regions, information on the thermal structure of the mantle may help to understand the underlying tectonic processes.

a)

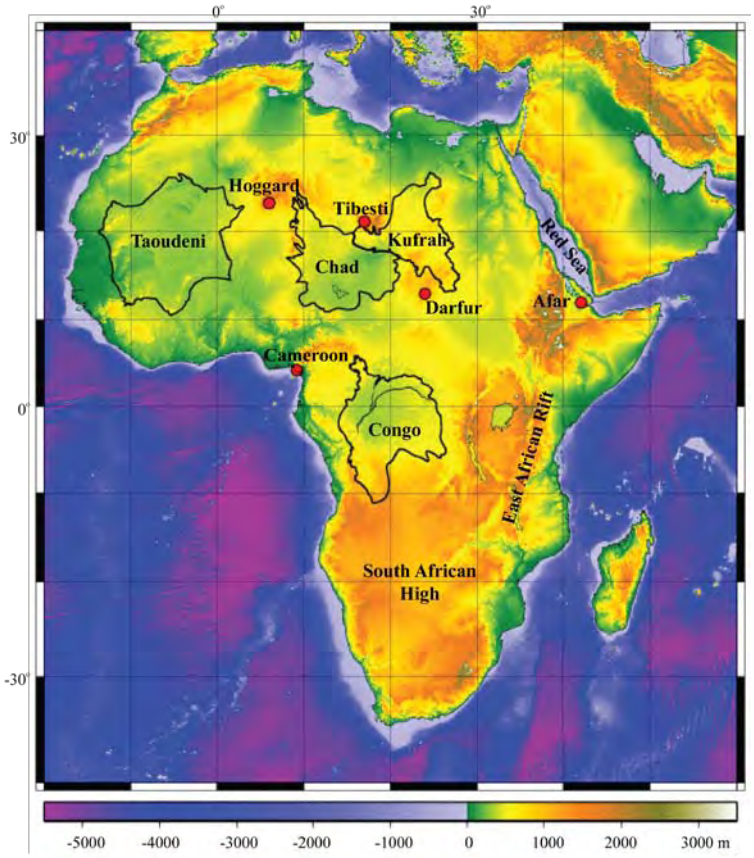

Figure 1: a) Topographic map of Africa with selected sedimentary basins and volcanic centres. Topography from Amante and Eakins (2009).

b)

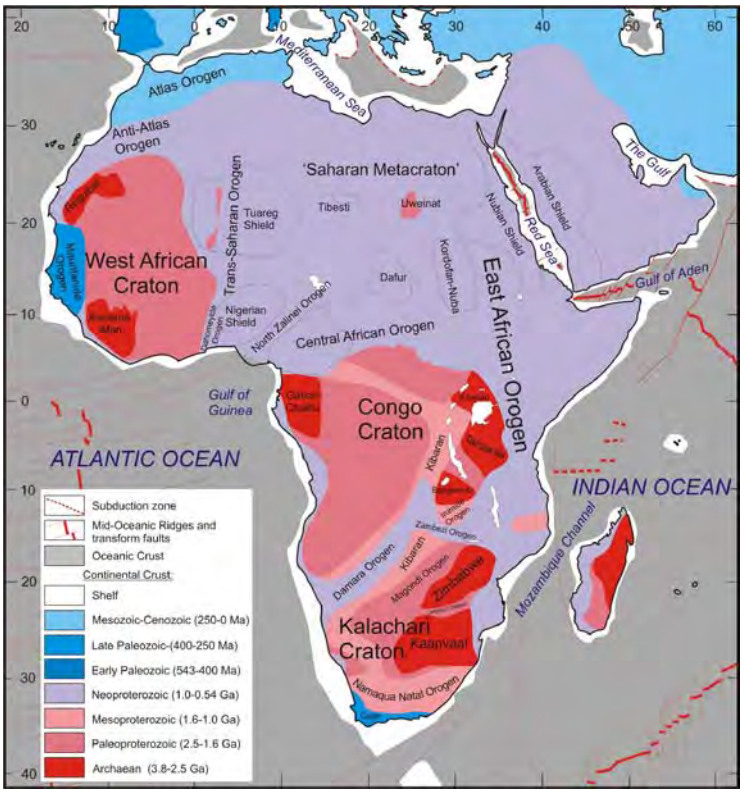

b) Outlines of cratonic areas in Africa based on age of the crustal basement (Gubanov and Mooney, 2009).

Southern and Eastern Africa differs from other continents in that it is substantially elevated above sea level, without recent mountain building. This is often explained as “dynamic topography”, i.e., as caused by an upstream of hot material in the mantle. However, to date there is no agreement on what part of the topography is in this sense “dynamic”, and how dynamic topography has changed with time, although this subject has been addressed by a number of studies (e.g., Gurnis et al., 2000; Conrad and Gurnis, 2003; Forte et al., 2010). Uplift and subsidence of the African plate, caused by flow and advection of density anomalies in the underlying mantle, determines which areas are below sea level, and at what depth. It is therefore of great importance for understanding of past environments and formation of natural resources. Before trying to model such mantle-derived uplift and subsidence, we first have to try to understand which parts of present-day topography are “dynamic”, i.e., supported by density anomalies and the flow they cause in the Earth's mantle.

In this report we present an overview of the mantle structure underneath Africa by analysing 18 tomography models of almost all main tomography groups. Most of the models are global (16) and on the scale of the whole mantle (12). Only 2 models are both regional and on the scale of the uppermost mantle. We then use the information in the tomography models to compute present-day dynamic topography for Africa. We also show that the contribution of lithosphere processes to topography changes is expected to be minor for intracratonic basins.

2. TOMOGRAPHY MODELS

2.1 General information about the 18 tomography models

Tomography models contain valuable information about the present-day state of the Earth's mantle. The models are built from delay-times that seismic waves experience on their route from a source (e.g., an earthquake) to a receiver. Unfortunately, the receiver coverage on the African continent is rather sparse, though recent campaigns (e.g., Africa Array, http://africaarray.psu.edu) are improving this situation somewhat. As a result of the sparse coverage, the resolution of tomography models may not be sufficient everywhere. We decided not to rely on one tomography model, but instead to analyse 13 whole mantle and 5 upper mantle tomography models (*Tables 1 and 2*). More detailed background information for each model can be found in Appendix A.

Table 1
List of tomography models

Name	Wave-type	Group	Reference	Website
Whole mantle				
MITP08	P	MIT	Li et al. (2008)	http://eapsweb.mit.edu/research/MITP08.txt.g
P362D28	P	Harvard	Antolik et al. (2003)	
PRI-P05	P	Princeton	Montelli et al. (2006)	http://www.spice-rtn.org/research/planetaryscale/tomography/
PRI-S05	S	Princeton	Montelli et al. (2006)	http://www.spice-rtn.org/research/planetaryscale/tomography/
S20RTSb	S	Michigan	Ritsema et al. (2004)	http://www.geo.lsa.umich.edu/~jritsema/Research.html
S362ANI	S	Harvard	Kustowski et al. (2008a)	http://www.seismology.harvard.edu/~kustowsk/MODELS/models.html
S362D28	S	Harvard	Antolik et al. (2003)	
SAW24B16	S	Berkely	Mégnin and Romanowicz (2000)	http://seismo.berkeley.edu/~pepe/saw24b16.html
SAW642AN	S	Berkely	Panning and Romanowicz (2006)	http://www.clas.ufl.edu/users/mpanning/SAW642AN.html
SB4L18	S	Scripps	Masters et al. (2000)	http://igppweb.ucsd.edu/~gabi/3dmodels.html
SG06	S	Texas		ftp://bratsche.geo.utexas.edu/outgoing/steveg
TOPOS362D1	S	Harvard	Gu et al. (2003)	
TX2007	S	Texas	Simmons et al. (2007)	www.spice-rtn.org/research/planetaryscale/tomography
MIX-A	P, S	NGU	This report	
Upper mantle				
CU_STD1.0	S	CU Boulder	Shapiro and Ritzwoller (2002)	http://ciei.colorado.edu/~nshapiro/MODEL/
CU_SRT1.0	S	CU Boulder	Shapiro and Ritzwoller (2002)	http://ciei.colorado.edu/~nshapiro/MODEL/
KP08	S	Cambridge	Priestley et al. (2008)	
LH08	S	MIT	Lebedev and van der Hilst (2008)	
SF09	S	Leicester	Fishwick (2010)	

Table 2
Information content of tomography models

Name	Nr of layers	Min depth (km)	Max depth (km)	Min Diff[a] (%)	Max Diff[a] (%)	Mean Diff[a] (%)	Standard deviation[a]
MITP08	64	23	2869	-3.45	1.86	-0.05	0.229
P362D28	43	50	2889	-2.16	1.92	0.01	0.377
PRI-P05	30	26	2800	-2.35	1.72	-0.08	0.322
PRI-S05	30	26	2800	-4.30	2.53	-0.14	0.597
S20RTSb	31	26	2800	-4.39	5.76	-0.05	0.814
S362ANI	25	25	2890	-6.26	5.87	-0.07	1.271
S362D28	43	50	2890	-4.53	8.61	-0.04	1.162
SAW24B16	58	25	2875	-6.53	5.24	-0.14	0.841
SAW642AN	44	25	2890	-7.53	7.57	-0.02	0.967
SB4L18	19	67	2798	-4.32	5.20	-0.08	0.971
SG06	22	50	2770	-5.28	6.01	-0.10	0.921
TOPOS362D1	44	25	2890	-4.50	7.49	-0.03	1.005
TX2007	22	50	2775	-4.27	6.75	-0.05	0.902
MIX-A	57	50	2850	-3.48	3.47	-0.13	0.515
CU_STD1.0	12	72	352	-7.17	9.69	-0.03	2.261
CU_SRT1.0	12	72	352	-7.00	8.53	0.02	2.105
KP08	16	40	400	-7.69	7.54	-0.14	1.529
LH08	16	7	661	-8.32	8.70	0.19	1.696
SF09	8	75	250	-11.19	8.73	-0.90	2.519

[a] Difference from reference model (see also Appendix A)

We have analysed the depth-dependence of variations within each model by calculating the standard deviation of the data for each depth slice. *Fig. 2* shows that we can separate the models into three groups: (1) shallow models, (2) general deep models, and (3) deep models with low resolution at upper lithosphere depths (models MITP08, P362D28, PRI-P05, PRI-S05, *Table 1*). This analysis is an aid to choose models to illustrate the lithosphere and upper mantle (groups 1 and 2) and the lower part of lithosphere, down from 400 km (groups 2 and 3). It also helps us to choose contour values for the isosurfaces in the 3D views: We have used ±3.5% for shallow models, ±3.5% (at lithosphere depth) and ±0.75% (at greater depth) for general deep models, and ±0.5% for deep models with low resolution at upper lithosphere depths. The 3-D plots generally do not include the entire mantle depth (depth range is shown in the figures) and may be vertically exaggerated (in particular at lithosphere depths).

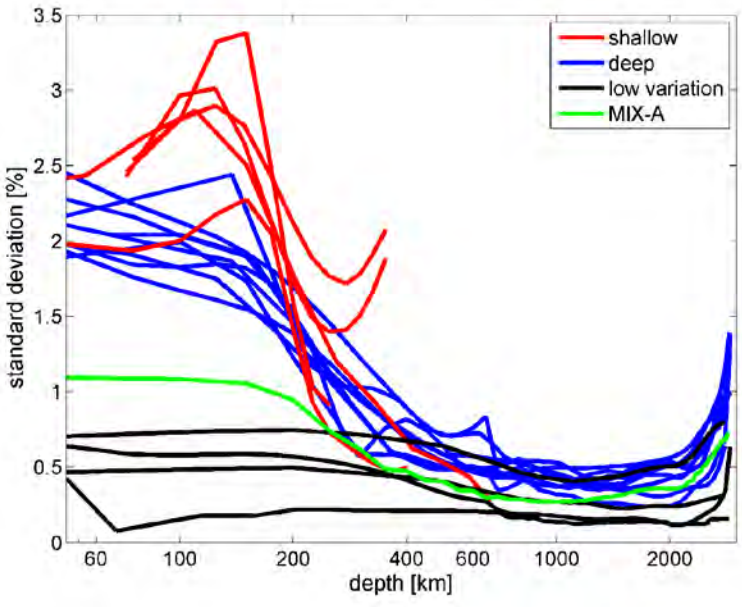

Figure 2: Standard deviation of tomography models versus depth shows a division into three groups: shallow, deep, and deep with low resolution at lithosphere depths. Note that the x-axis is logarithmic.

2.2 Whole mantle tomography models

In this section we visualise 10 S-wave and 3 P-wave whole mantle tomography models (*Table 1 and 2, Figs. 3-16*). These represent the most recent models of the main university groups working on imaging of the Earth with global tomography. For each model we present the following:

- Horizontal map views at 200 km depth (at or through the base of the lithosphere), 500 km depth (above the base of the upper mantle) and 800 km depth (below the 660 km discontinuity).
- Five cross-sections along great-circles (*Fig. 3*): 1) a N-S cross-section through the Kufrah and Congo Basins, the Congo and Kalahari Cratons and the South Africa high, 2) a NE-SW cross-section through Afar, the East African Rift and South Africa, 3) a W-E cross-section through the Taoudeni, Chad and Kufrah Basins, the West African Craton and the Red Sea, 4) a W-E cross-section through the Congo Basin, the Congo Craton and the East African Rift and 5) a NW-SE cross-section through the Atlas, the Tibesti, Hoggar and Darfur volcanic centres, and the East African Rift.
- 3D iso-surfaces at ±0.5%,/±0.75% and 3.5% velocity anomaly. Vertical exaggeration is 4.5 times for whole mantle models and 7 times for upper mantle models.

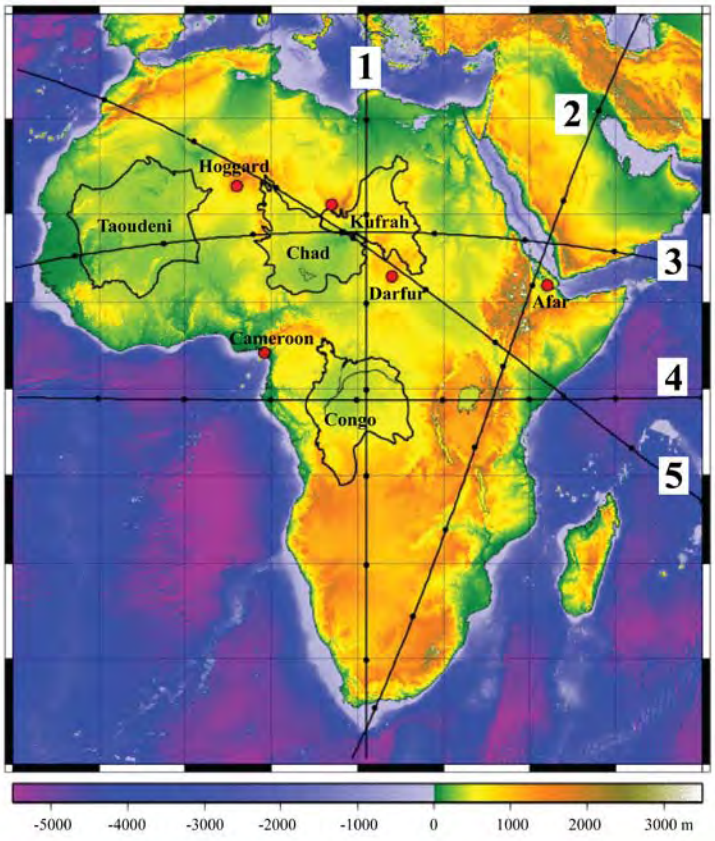

Figure 3: Locations of cross-sections through the tomography models.

Global tomography models present differences in measured velocities from radially symmetric models for compressional (P-wave) and shear (S-wave) wave velocities. Shear wave models utilize one or more of the following: body waves, surface waves (Rayleigh and Love), normal mode waveforms, and anisotropy (delay times in arrivals of surface waves). Each of these wave types have their strengths and weaknesses in imaging the Earth's structure. In general, P-wave tomography models are best at imaging regions with numerous events, such as subduction zones or plumes (Romanowicz, 2003). Shear wave tomography models that use body waves or long period waves are more effective at imaging lower mantle structure or topography of discontinuities. Models that are calculated from surface waves or

anisotropy are best at imaging structure in the upper mantle, as mantle anisotropy is strongest in those depths. It is difficult to strictly compare tomography models because they use different inversion methods, data sources, and reference models. Besides the ISC bulletin, numerous other seismic catalogues may be used which contain information recorded at various other permanent or temporary arrays, such as IRIS/PASSCAL, GEOSCOPE, and GSN. Different methods are employed, primarily because numerous different types of seismic waves are used. Therefore travel time calculations, grid parameterization, and inversion methods will vary in order to best suit the data. Unfortunately, all global tomography models are plagued by a lack of sufficient data under Africa. Of the three P-wave tomography models we have used, MIT-P08 has the greatest amount of data sources and therefore best resolution under Africa. Shear wave models S20RTSb and SG06 image smaller features in the African mid-lower mantle than other models, but the reliability in these regions are questionable due to poor ray coverage. The three models from the Harvard group, S362ANI, S362D28, and TOPOS362, nicely image large-scale structures in the mantle, but are unable to image the smaller scale features seen in S20RTSb and SG06. Surprisingly, anisotropy tomography models S362ANI and SAW642AN do not image the African cratons (Fig. 1b) as well as other shear wave models. The tomography models from Princeton seem less suitable for African mantle. Their resolution is rather poor, and the fast and slow anomalies do not match well with other models.

All models show low velocities under Afar and in the lowermost mantle under Southern Africa. The latter is part of the African Large Low Shear Velocity Province (LLSVP). These two regions of low velocities are more or less clearly connected in all models, indicating a causal relationship, i.e., a hot upwelling reaching all the way from the lowermost mantle to Afar and leading to volcanism there and in the East African Rift. Also the models (S-wave models more than P-wave) usually show high seismic velocities beneath the cratons (West Africa, Congo, Kalahari, Fig. 1b). Yet the depth extent of the high velocities varies considerably among models, indicating the possibility of substantial vertical smearing. Other features are less well resolved. There is little consistent structure imaged in the mid-mantle and in many regions of the shallow mantle, including beneath the Atlas Mountains and the volcanic centres at Hoggar, Tibesti and Darfur (Fig. 1a).

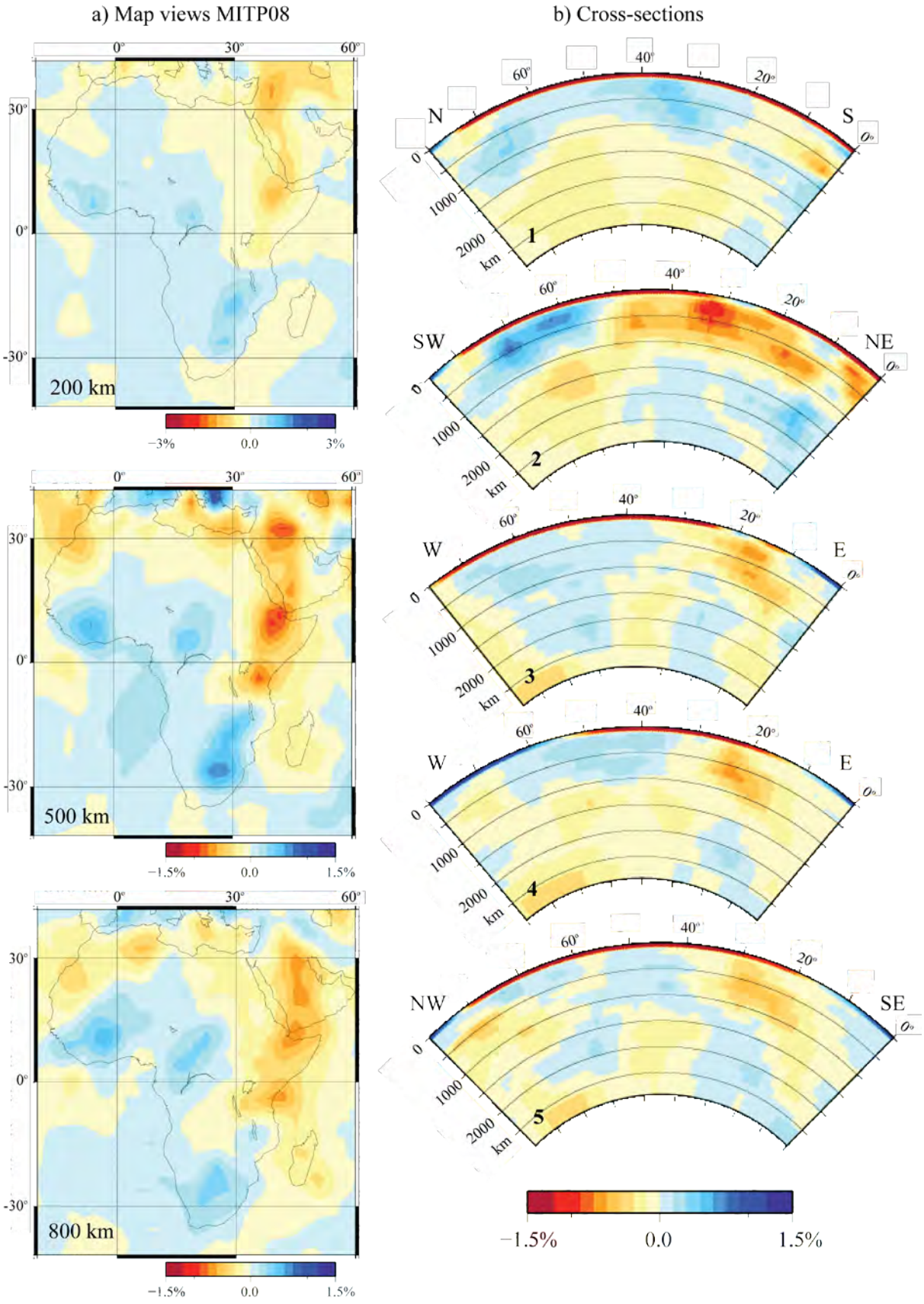
a) Map views MITP08
b) Cross-sections
200 km
500 km
800 km
−3%
0.0
3%
−1.5%
0.0
1.5%
N
S
SW
NE
W
E
W
E
NW
SE
1
2
3
4
5
km

c) 3D view

d) Location of cross-sections

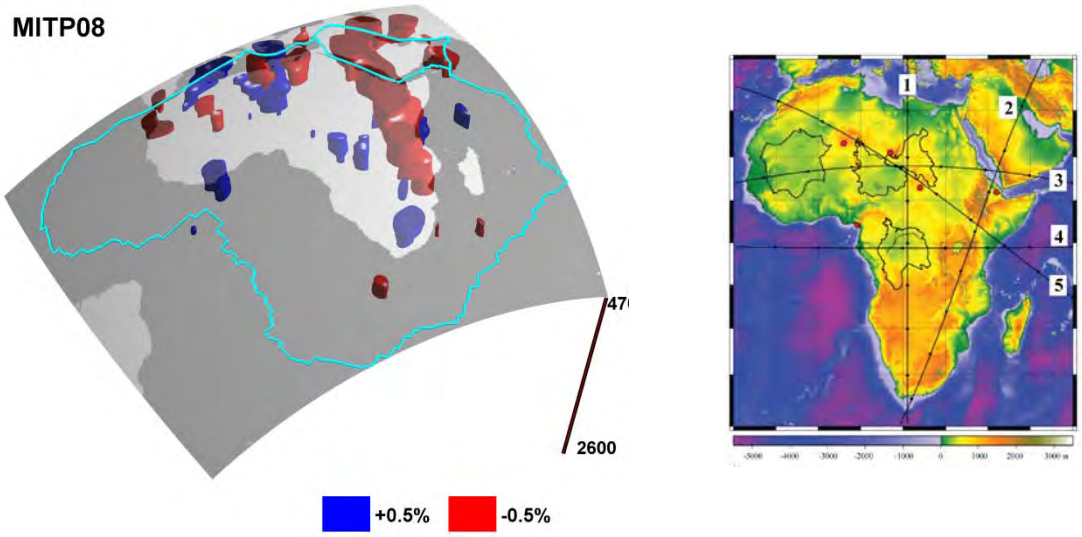

Figure 4: MITP08 (P-wave model). a) Map views, b) cross-sections, c) 3D view, and d) locations of cross-sections.

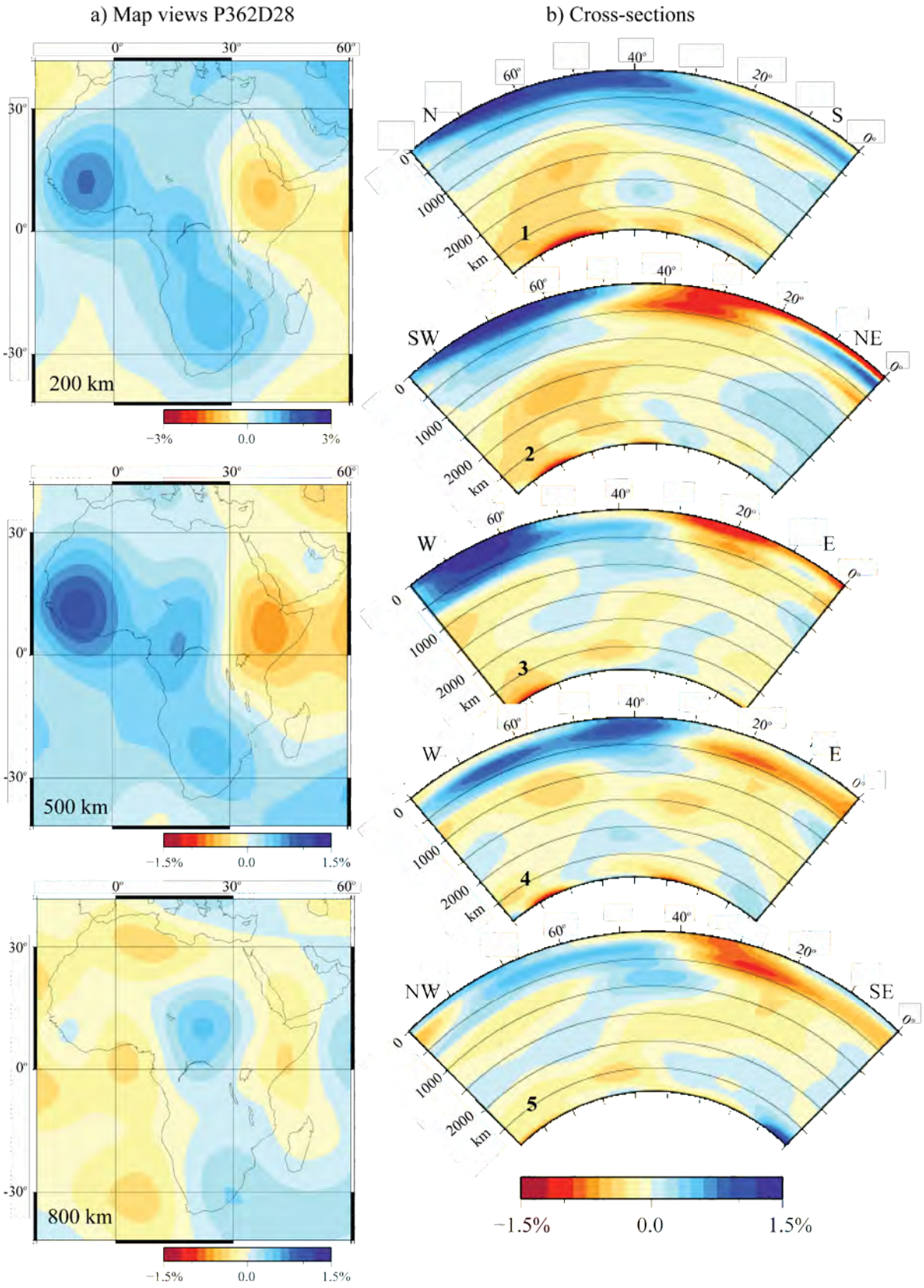
a) Map views P362D28
b) Cross-sections
200 km
500 km
800 km
−3%
0.0
3%
−1.5%
0.0
1.5%
N
S
SW
NE
W
E
W
E
NW
SE
1
2
3
4
5
0
1000
2000
km
0°
30°
60°
40°
20°
−30°

c) 3D view

d) Location of cross-sections

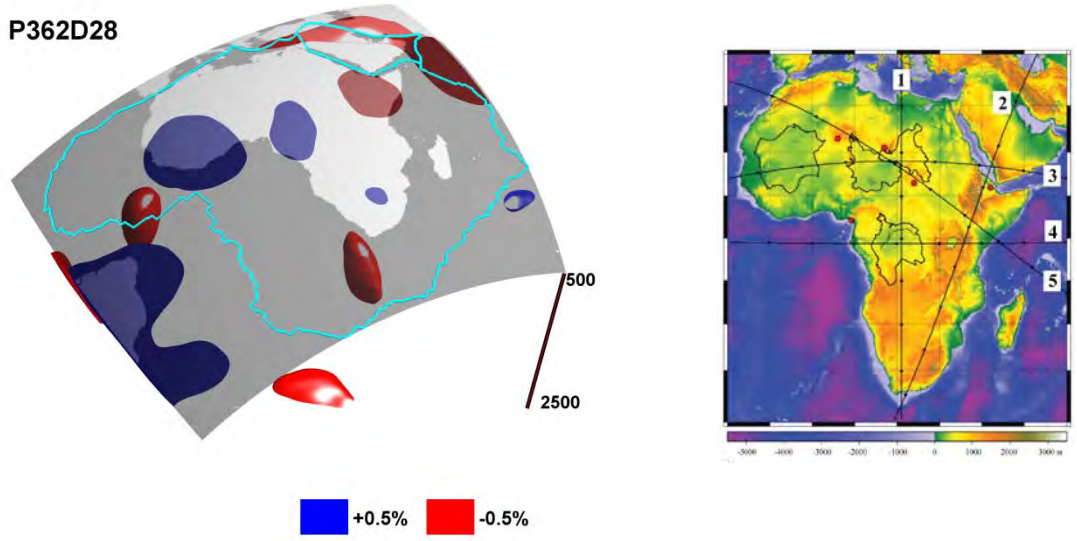

Figure 5: P362D28 (P-wave model). a) Map views, b) cross-sections, c) 3D view, and d) locations of cross-sections.

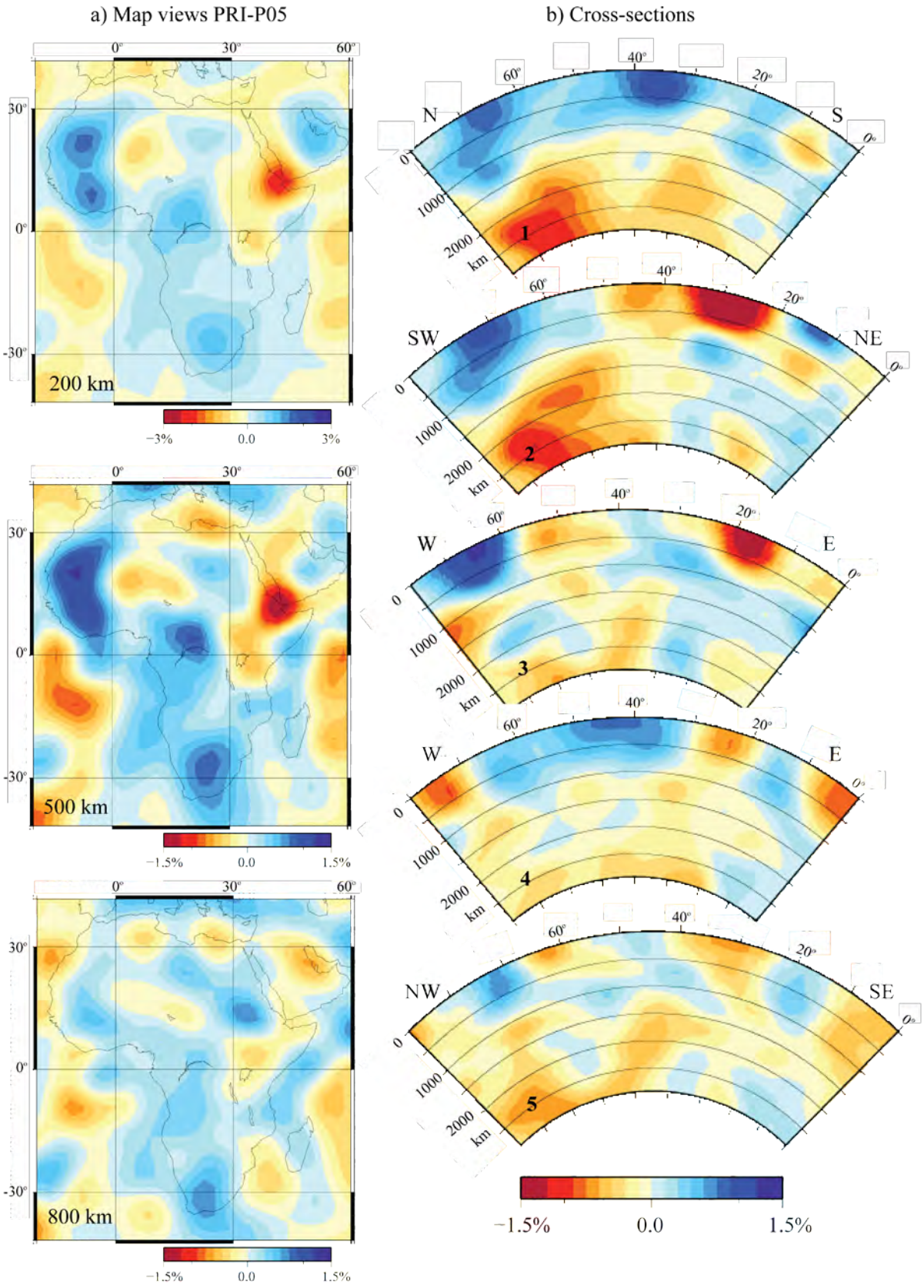
a) Map views PRI-P05
b) Cross-sections
200 km
500 km
800 km
−3%
0.0
3%
−1.5%
0.0
1.5%
N
S
SW
NE
W
E
W
E
NW
SE
1
2
3
4
5
km

c) 3D view

d) Location of cross-sections

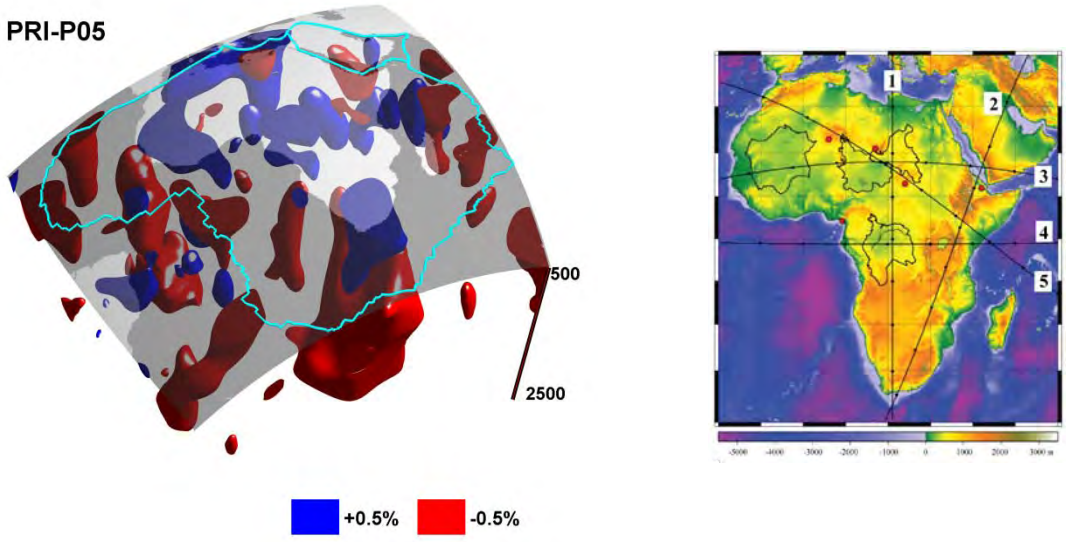

Figure 6: PRI-P05 (P-wave model). a) Map views, b) cross-sections, c) 3D view, and d) locations of cross-sections.

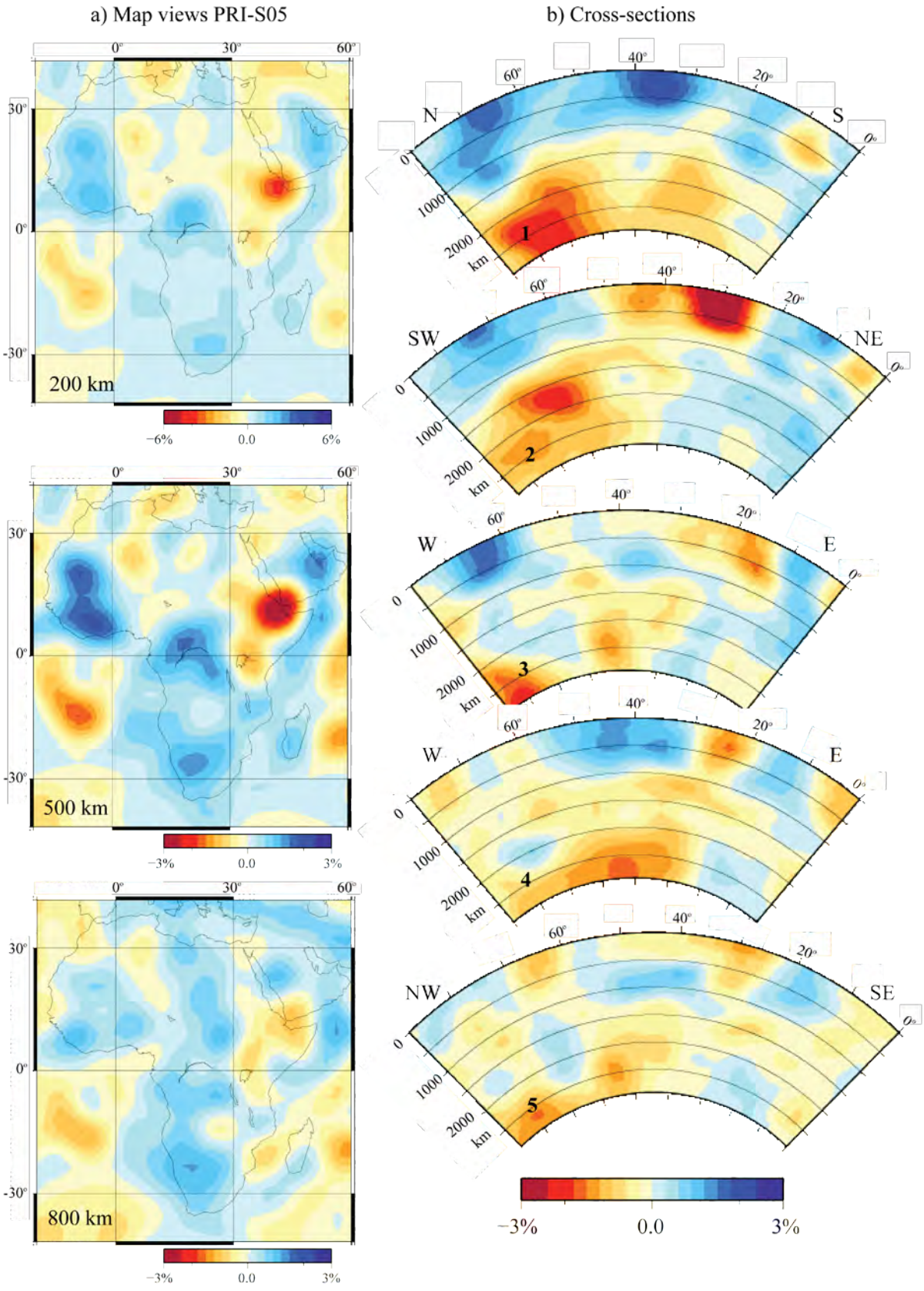
a) Map views PRI-S05
b) Cross-sections
200 km
500 km
800 km
−6%
0.0
6%
−3%
0.0
3%
N
S
SW
NE
W
E
W
E
NW
SE
1
2
3
4
5
km

c) 3D view

d) Location of cross-sections

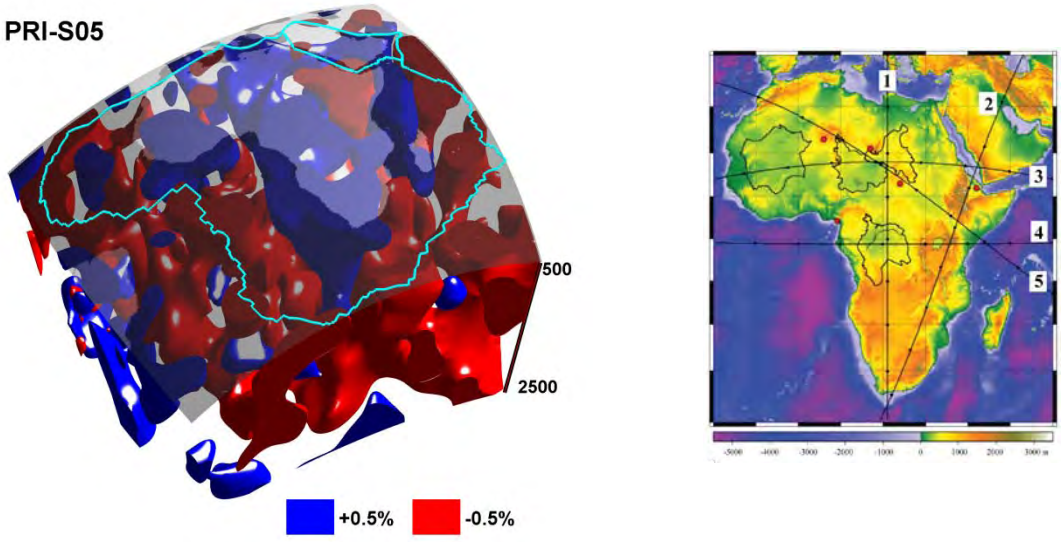

Figure 7: PRI-S05 (S-wave model). a) Map views, b) cross-sections, c) 3D view, and d) locations of cross-sections.

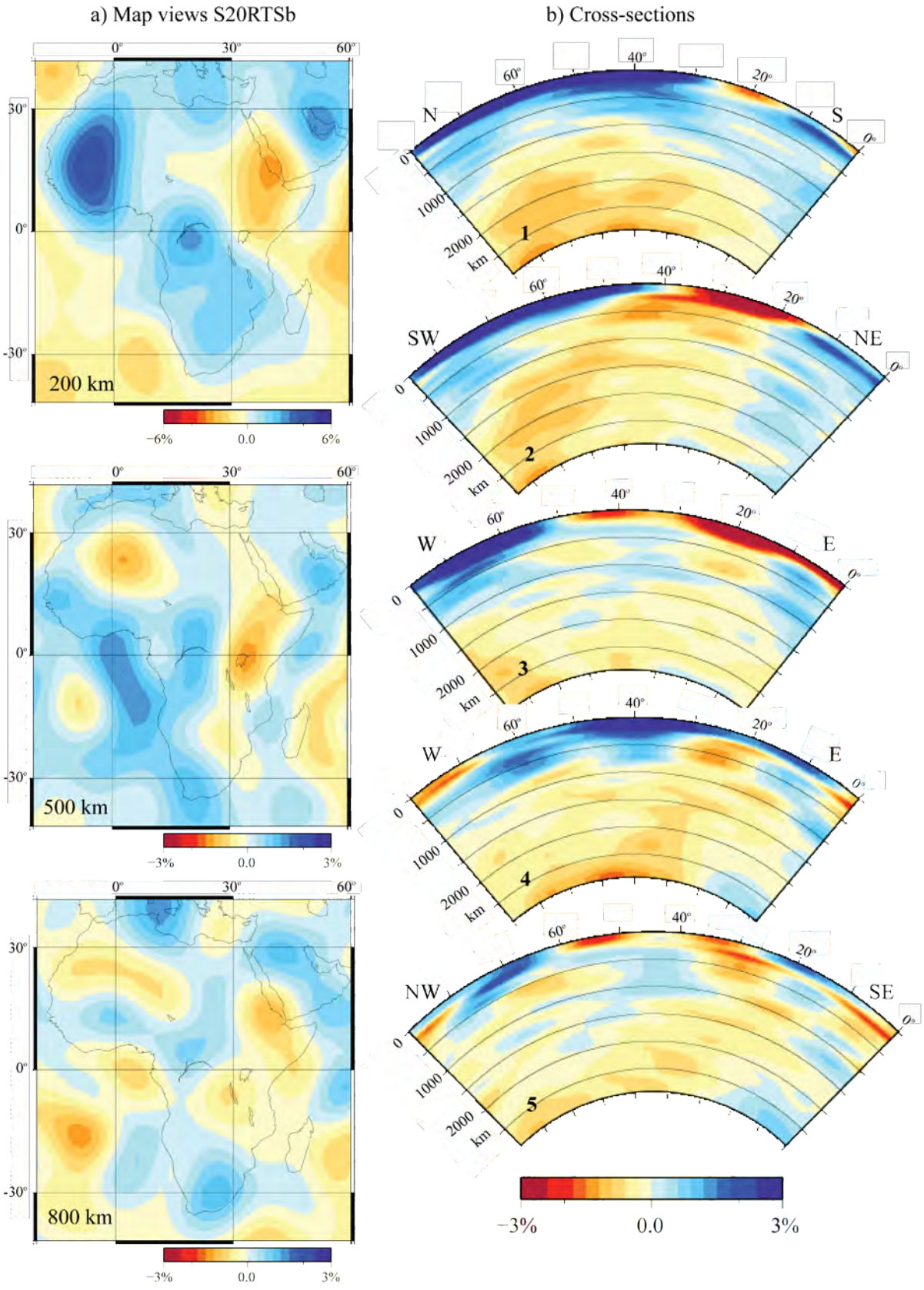
a) Map views S20RTSb
b) Cross-sections
200 km
500 km
800 km
−6%
0.0
6%
−3%
0.0
3%
N
S
SW
NE
W
E
W
E
NW
SE
1
2
3
4
5
km

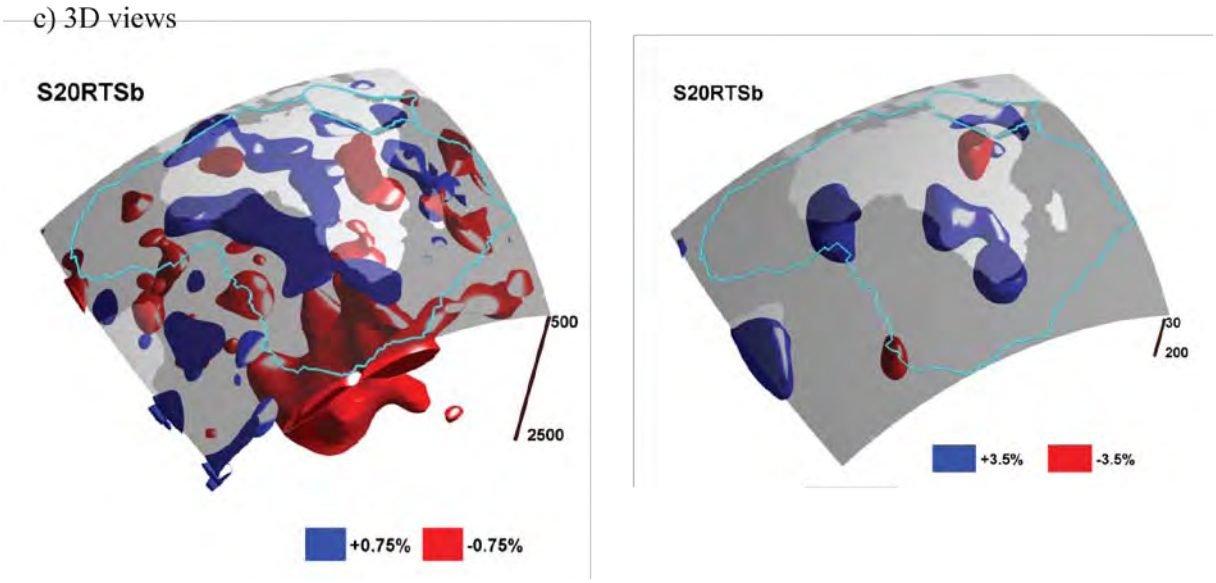

d) Location of cross-sections

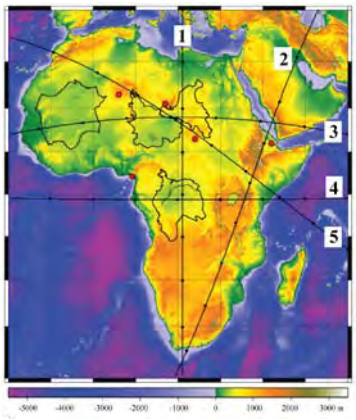

Figure 8: S20RTSb (S-wave model). a) Map views, b) cross-sections c) 3D views, and d) locations of cross-sections.

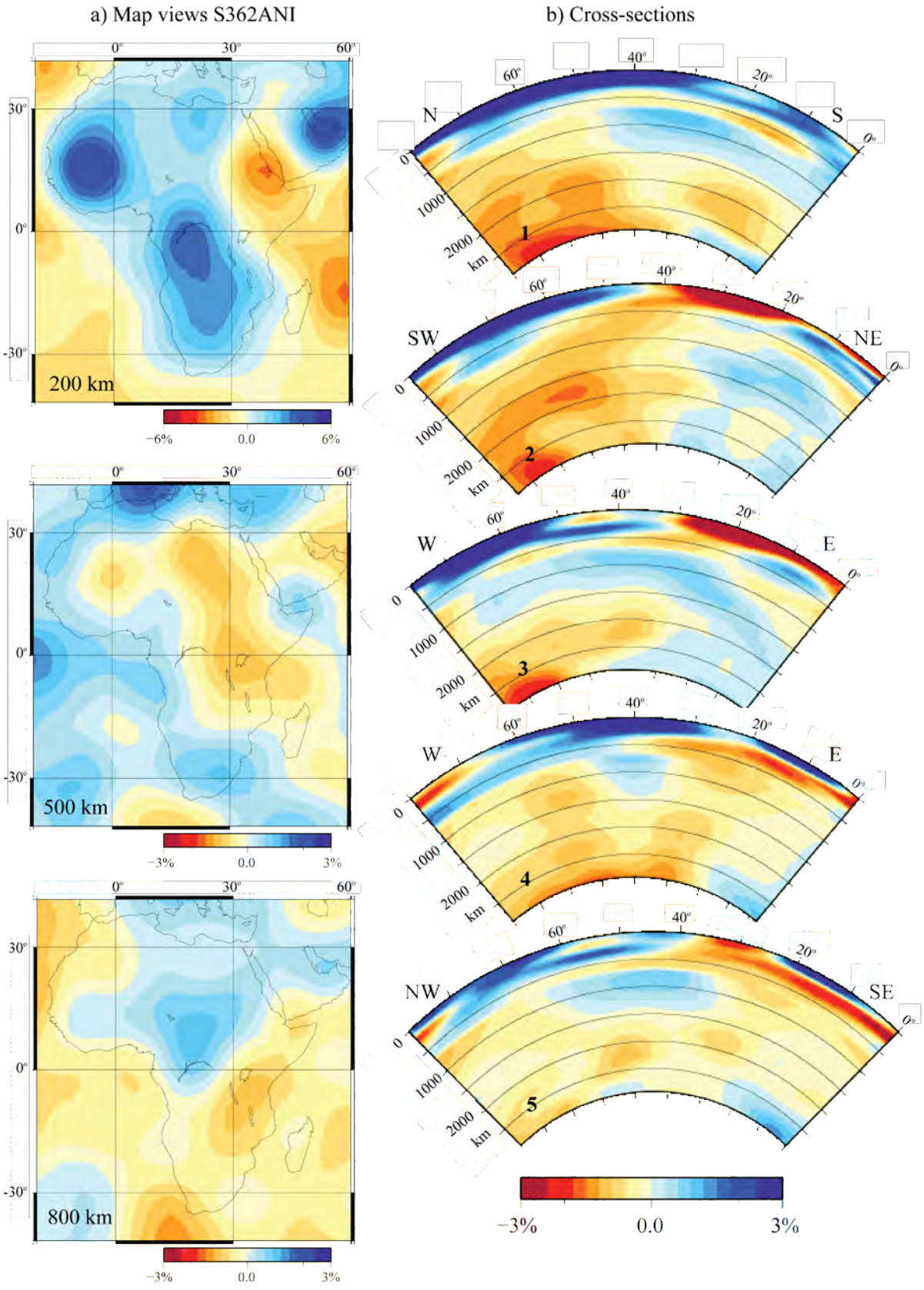
a) Map views S362ANI
b) Cross-sections
200 km
500 km
800 km
−6%
0.0
6%
−3%
0.0
3%
N
S
SW
NE
W
E
W
E
NW
SE
1
2
3
4
5
0
1000
2000
km
0°
30°
60°
40°
20°
−30°

c) 3D views

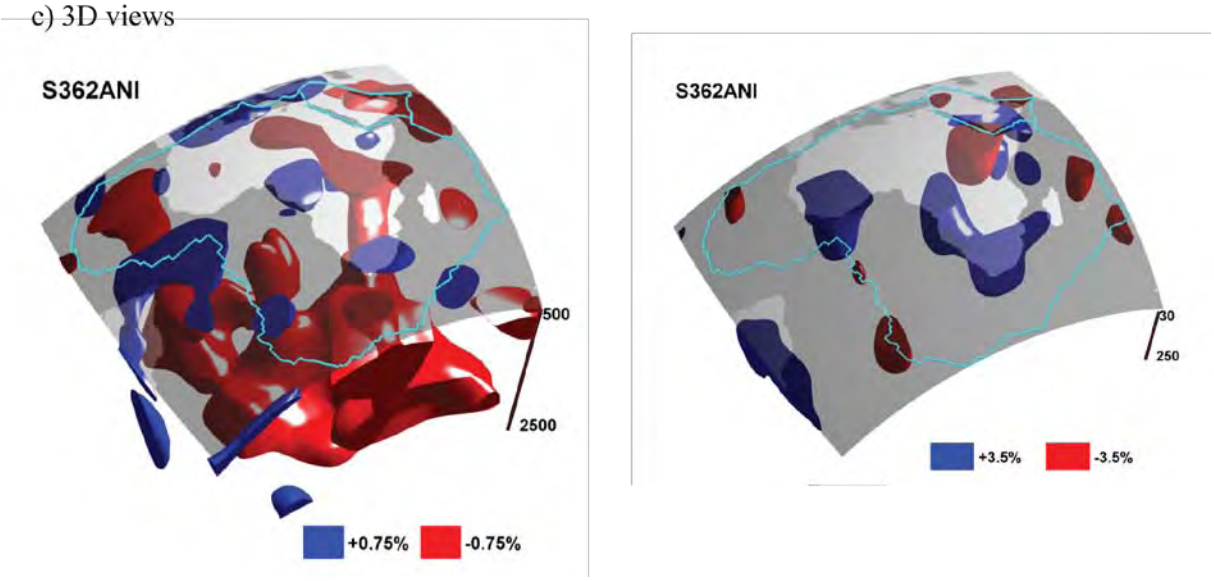

d) Location of cross-sections

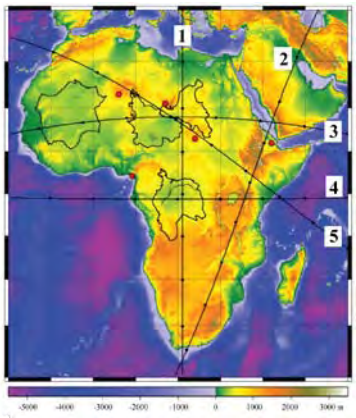

Figure 9: S362ANI (S-wave model). a) Map views, b) cross-sections c) 3D views, and d) locations of cross-sections.

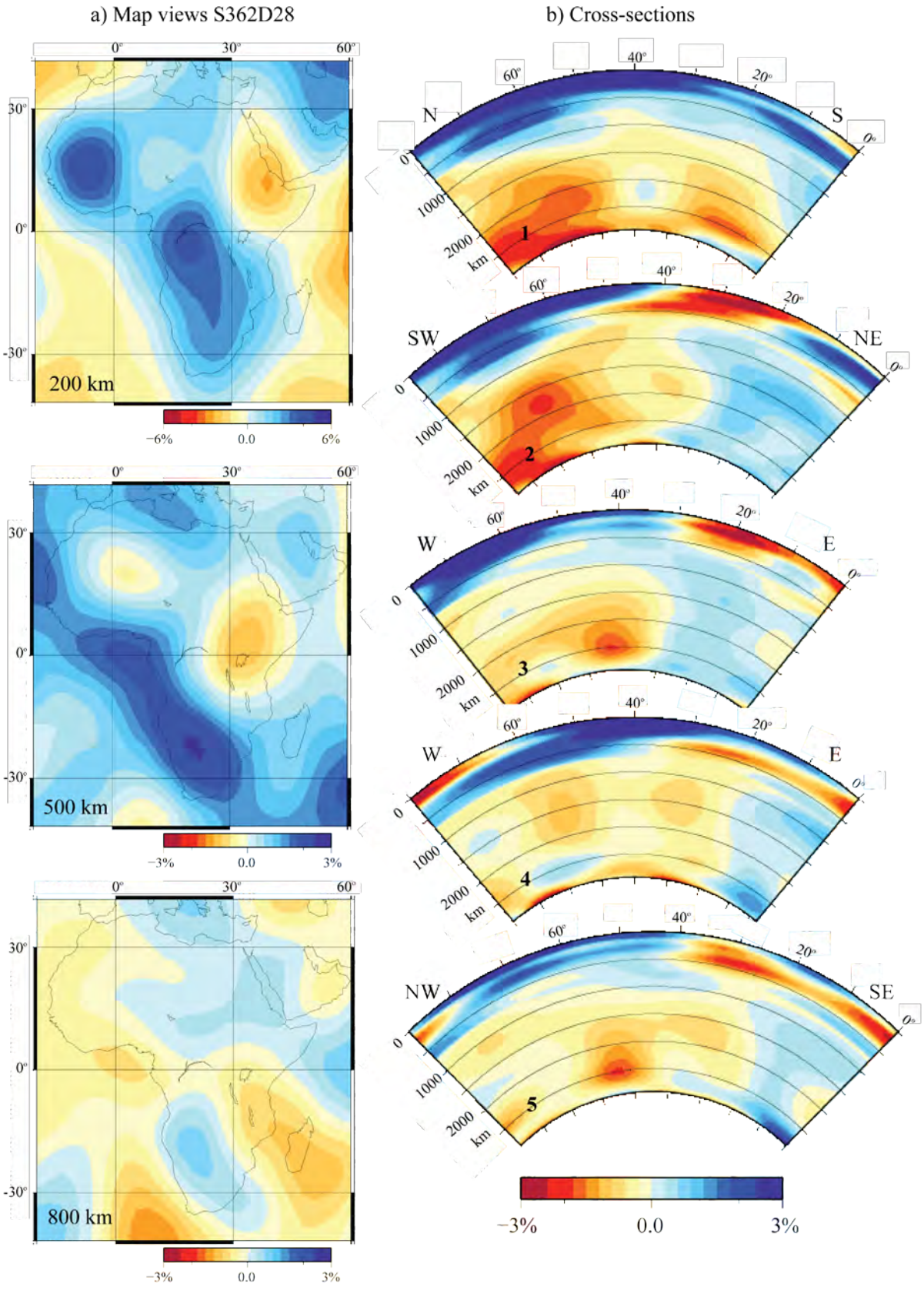
a) Map views S362D28
b) Cross-sections
200 km
500 km
800 km
−6%
0.0
6%
−3%
0.0
3%
N
S
SW
NE
W
E
W
E
NW
SE
1
2
3
4
5
km

c) 3D views

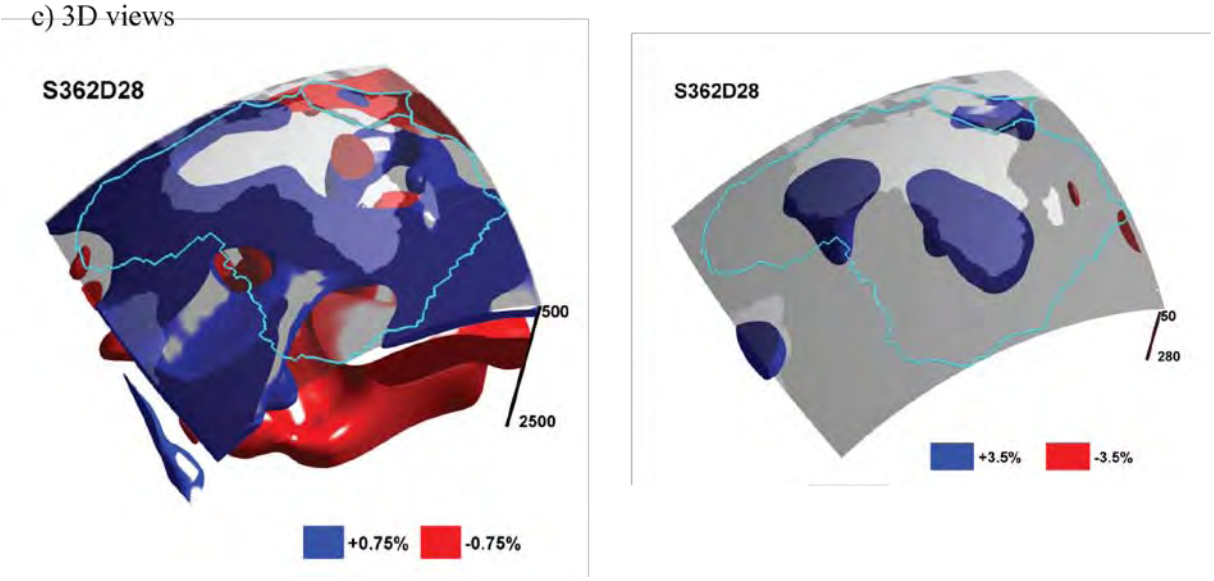

d) Location of cross-sections

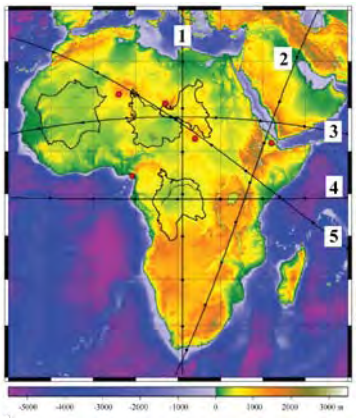

Figure 10: S362D28 (S-wave model). a) Map views, b) cross-sections c) 3D views, and d) locations of cross-sections.

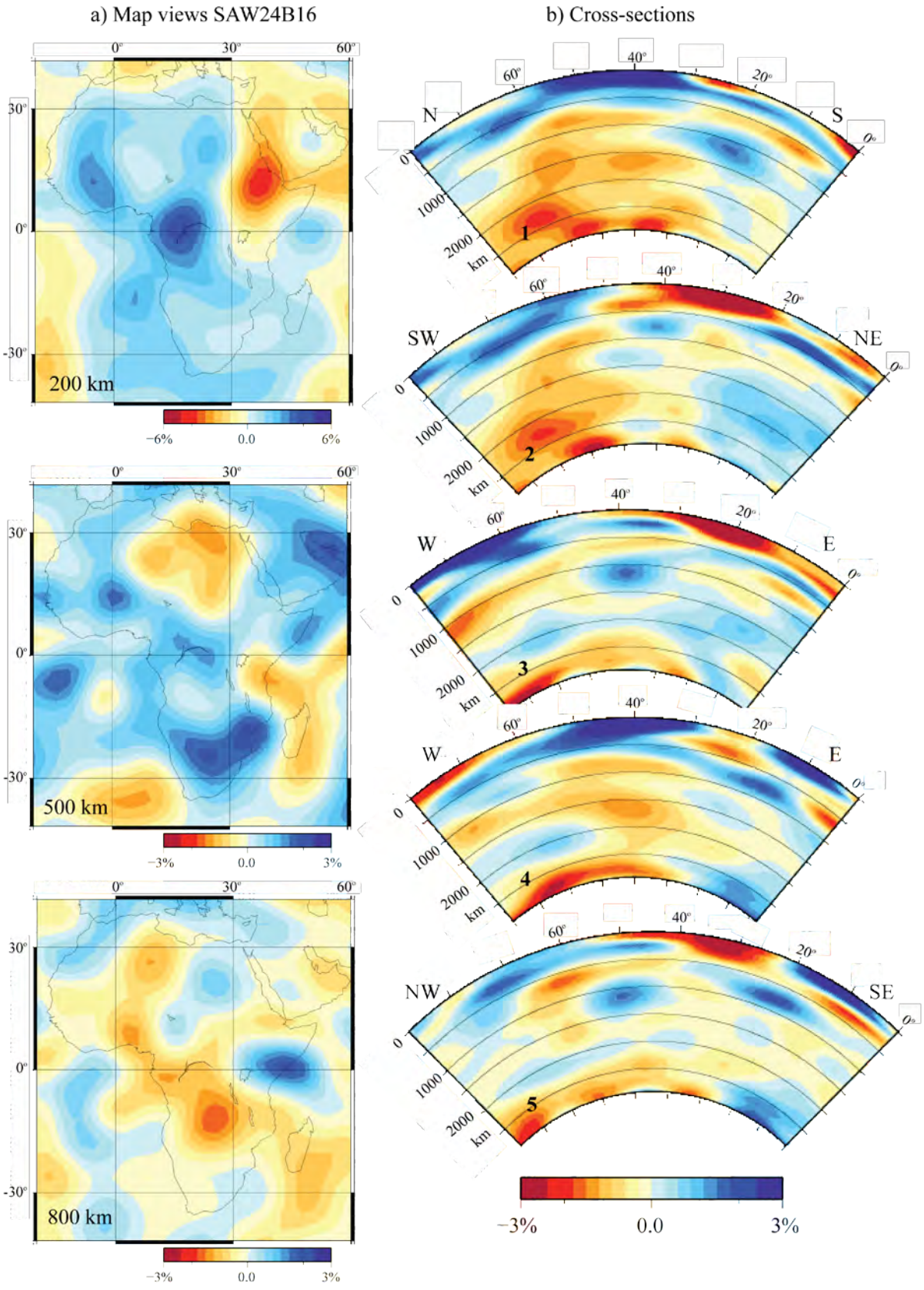
a) Map views SAW24B16
b) Cross-sections
200 km
500 km
800 km
−6%
0.0
6%
−3%
0.0
3%
N
S
SW
NE
W
E
W
E
NW
SE
1
2
3
4
5
0
1000
2000
km
40°
60°
20°
0°
30°
−30°

c) 3D views

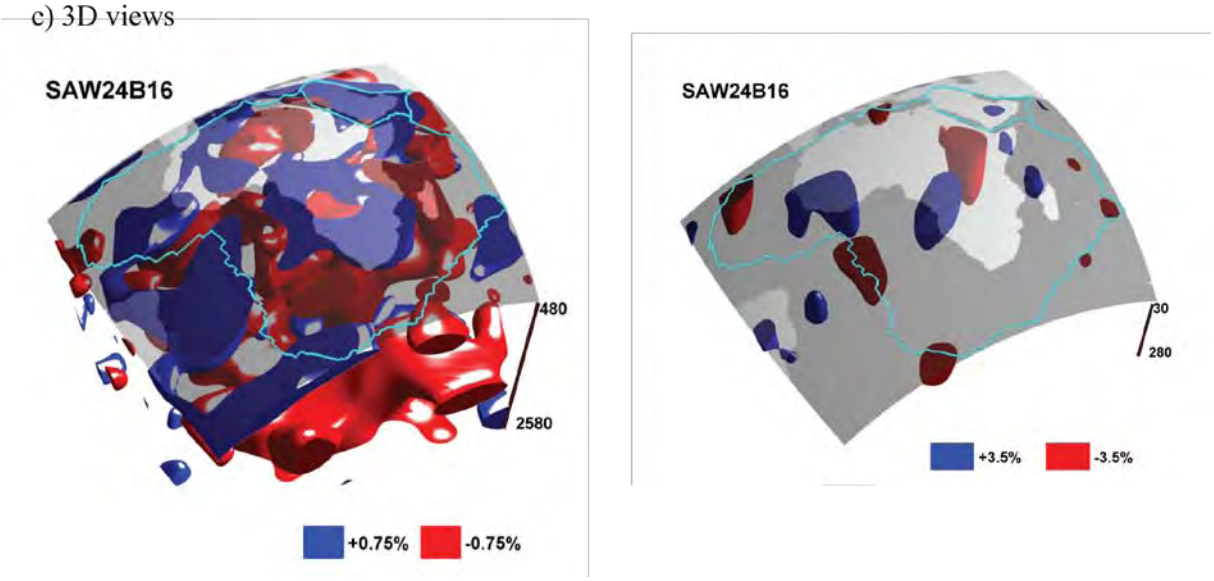

d) Location of cross-sections

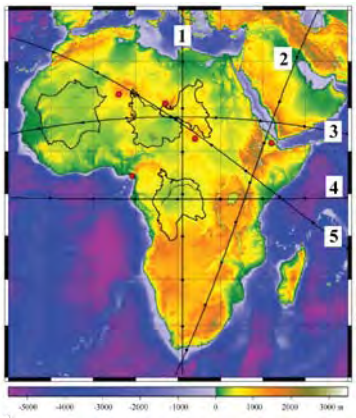

Figure 11: SAW24B16 (S-wave model). a) Map views, b) cross-sections c) 3D views, and d) locations of cross-sections.

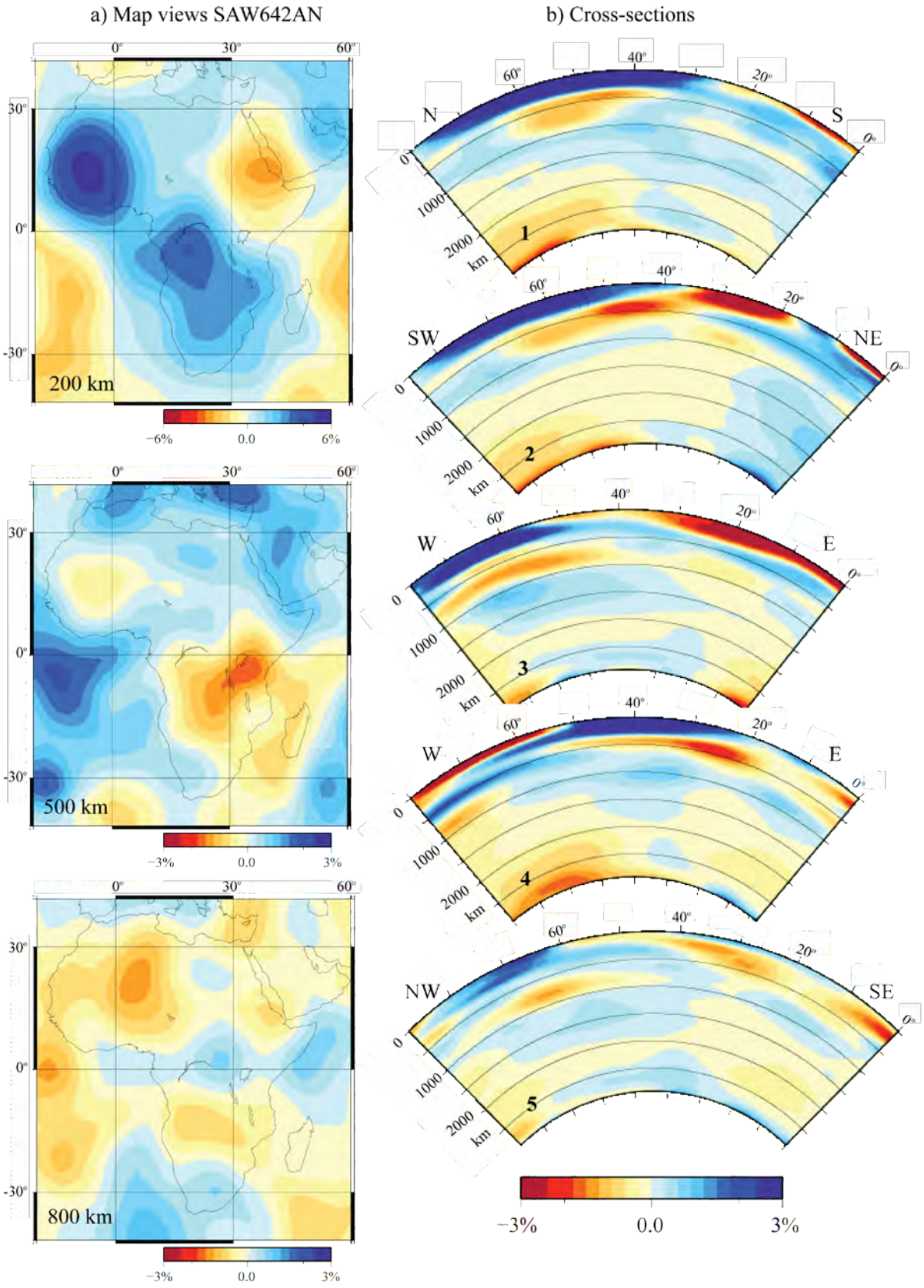
a) Map views SAW642AN
b) Cross-sections
200 km
500 km
800 km
−6%
0.0
6%
−3%
0.0
3%
N
S
SW
NE
W
E
W
E
NW
SE
1
2
3
4
5
km

c) 3D views

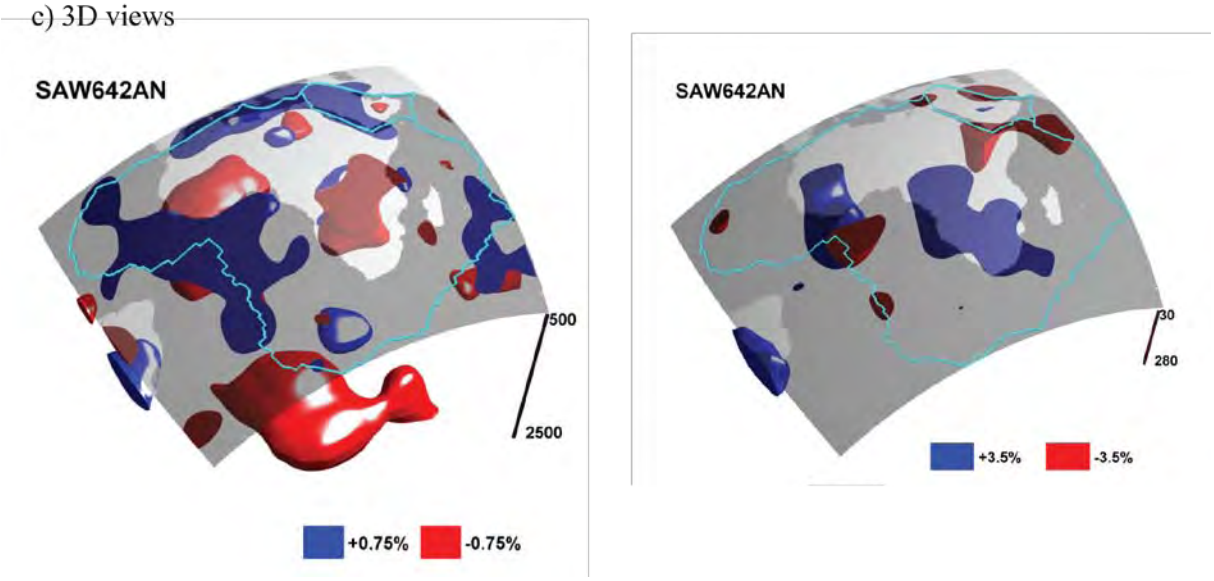

d) Location of cross-sections

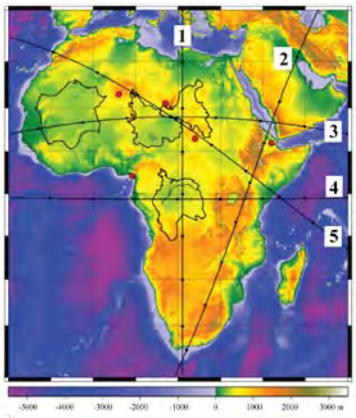

Figure 12: SAW642AN (S-wave model). a) Map views, b) cross-sections c) 3D views, and d) locations of cross-sections.

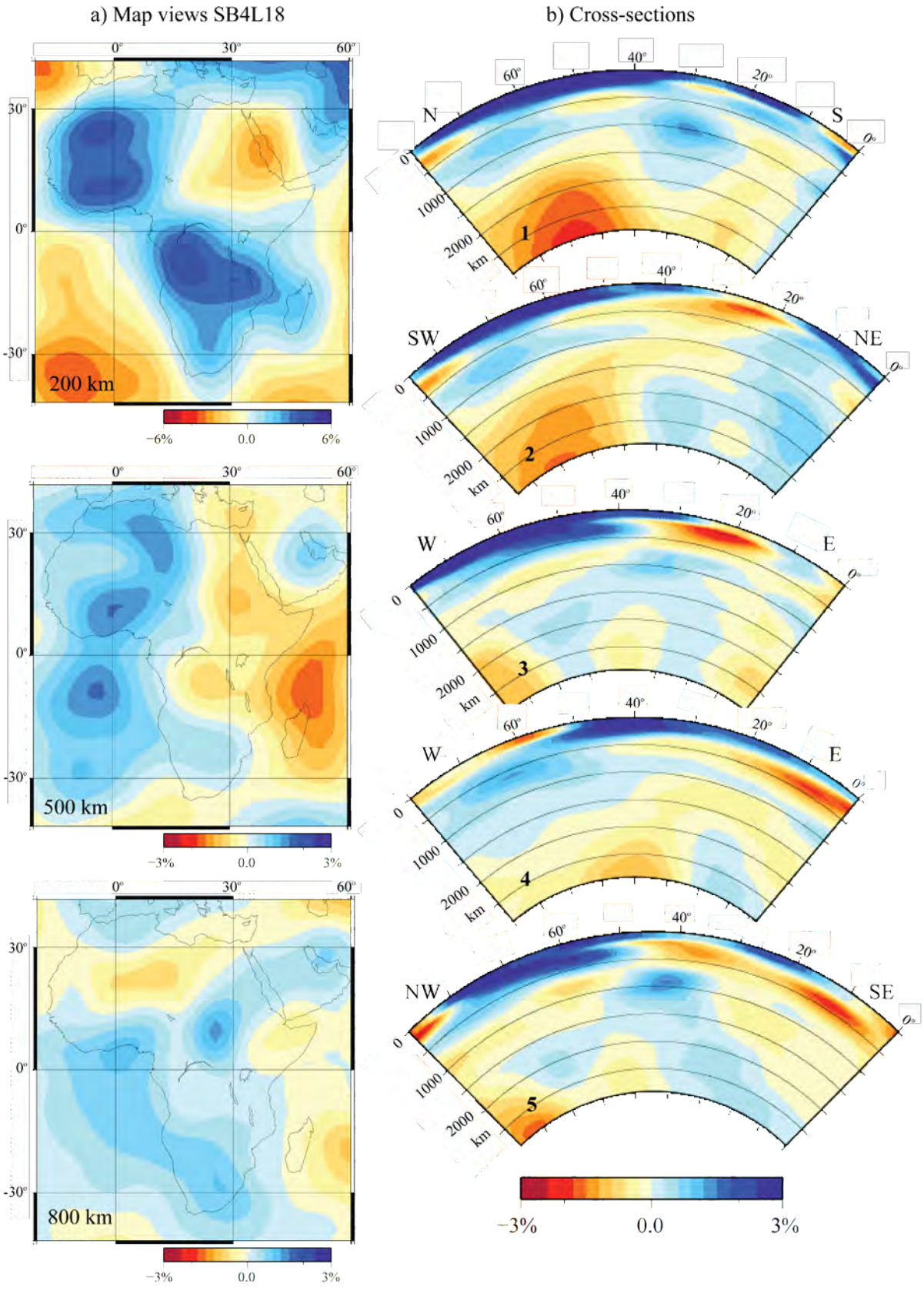
a) Map views SB4L18
b) Cross-sections
200 km
500 km
800 km
−6%
0.0
6%
−3%
0.0
3%
N
S
SW
NE
W
E
W
E
NW
SE
1
2
3
4
5
km

c) 3D views

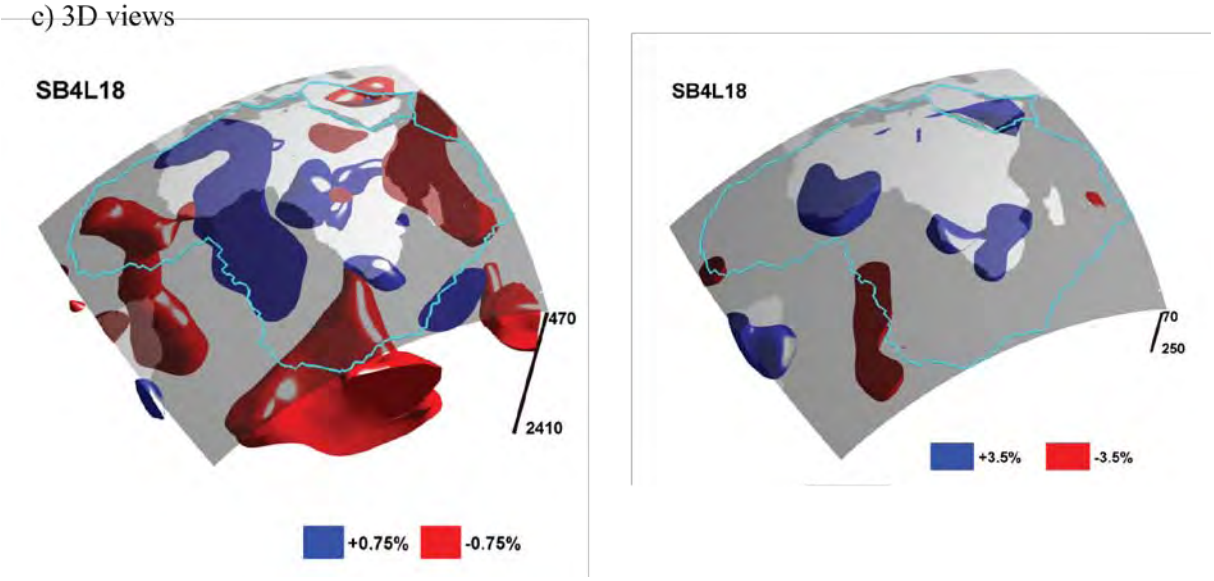

d) Location of cross-sections

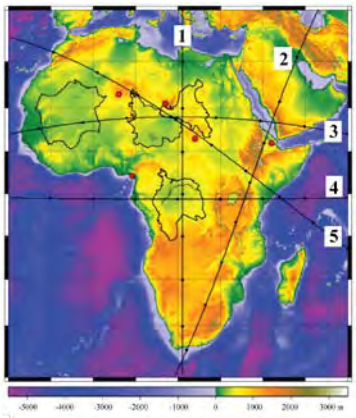

Figure 13: SB4L18 (S-wave model). a) Map views, b) cross-sections c) 3D views, and d) locations of cross-sections.

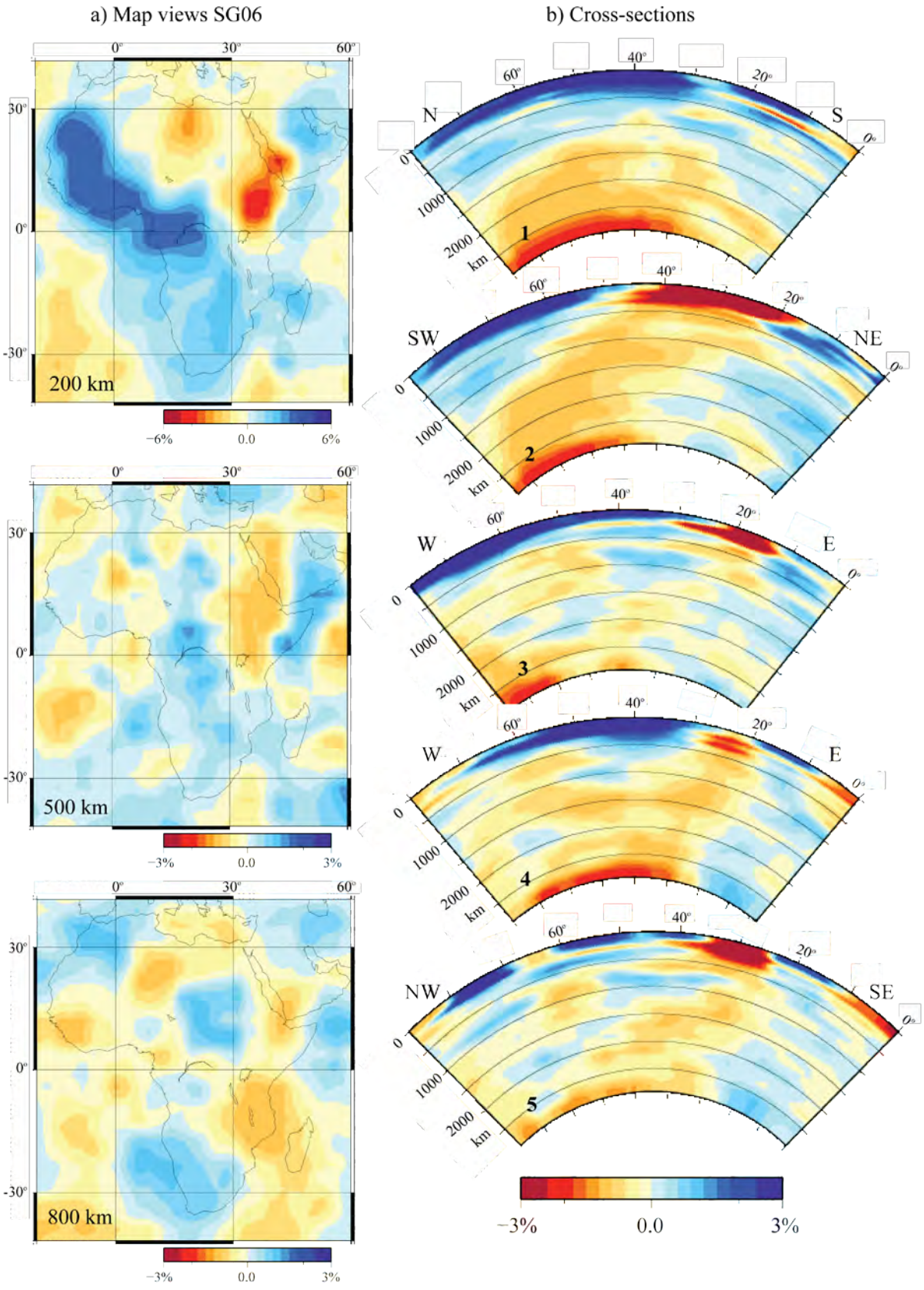
a) Map views SG06
b) Cross-sections
200 km
500 km
800 km
−6%
0.0
6%
−3%
0.0
3%
N
S
SW
NE
W
E
W
E
NW
SE
1
2
3
4
5
km

c) 3D views

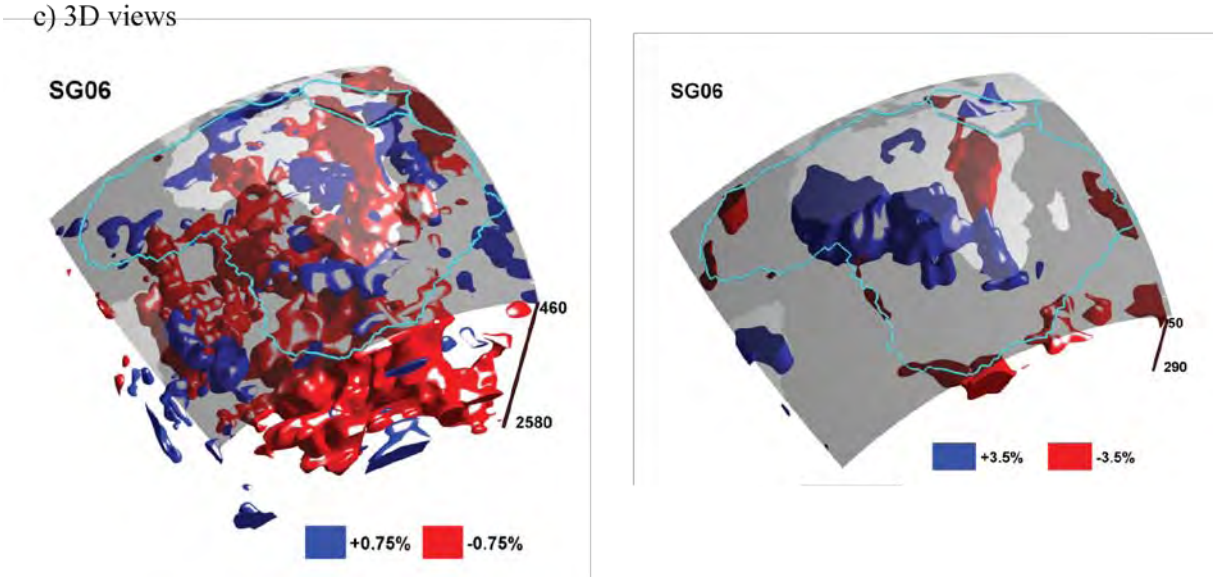

d) Location of cross-sections

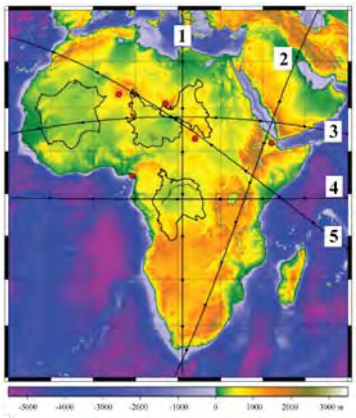

Figure 14: SG06 (S-wave model). a) Map views, b) cross-sections c) 3D views, and d) locations of cross-sections.

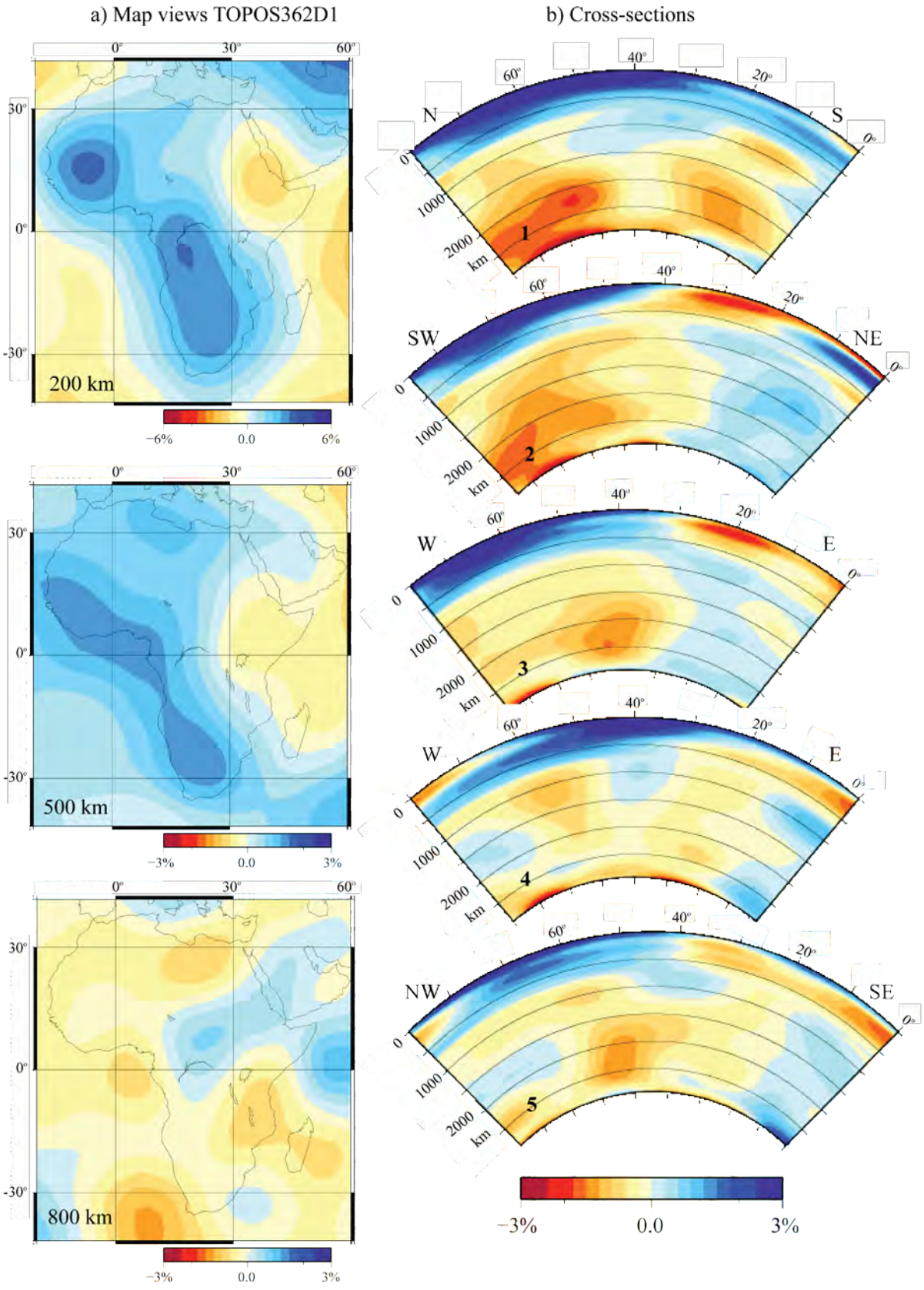
a) Map views TOPOS362D1
b) Cross-sections
200 km
500 km
800 km
−6%
0.0
6%
−3%
0.0
3%
N
S
SW
NE
W
E
W
E
NW
SE
1
2
3
4
5
km

c) 3D views

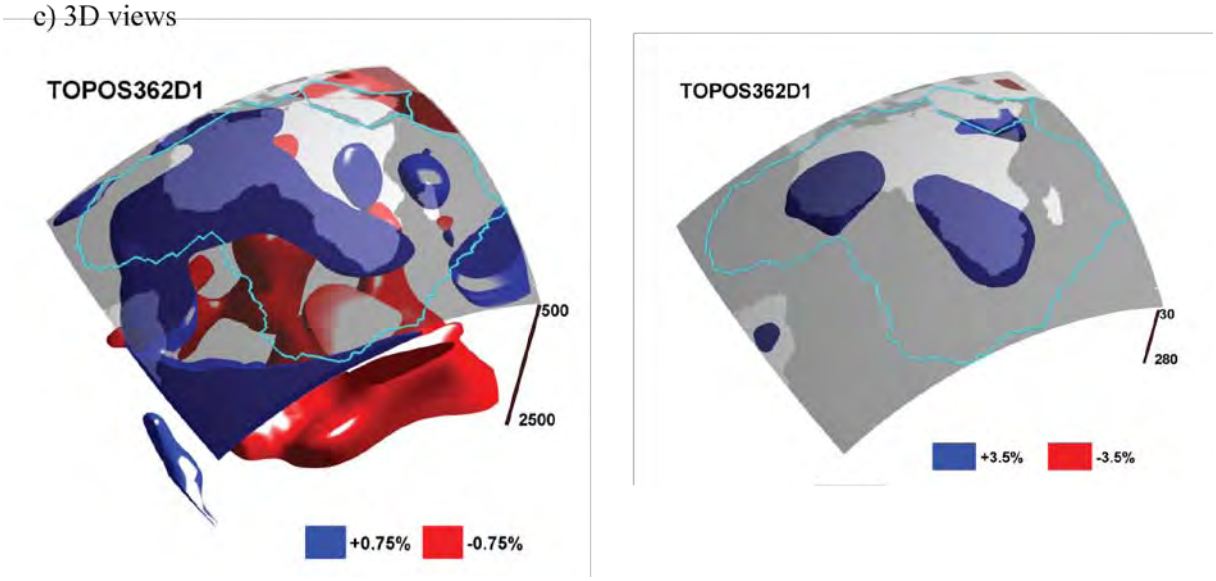

d) Location of cross-sections

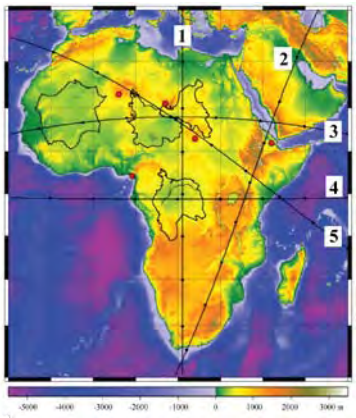

Figure 15: TOPOS362D1 (S-wave model). a) Map views, b) cross-sections c) 3D views, and d) locations of cross-sections.

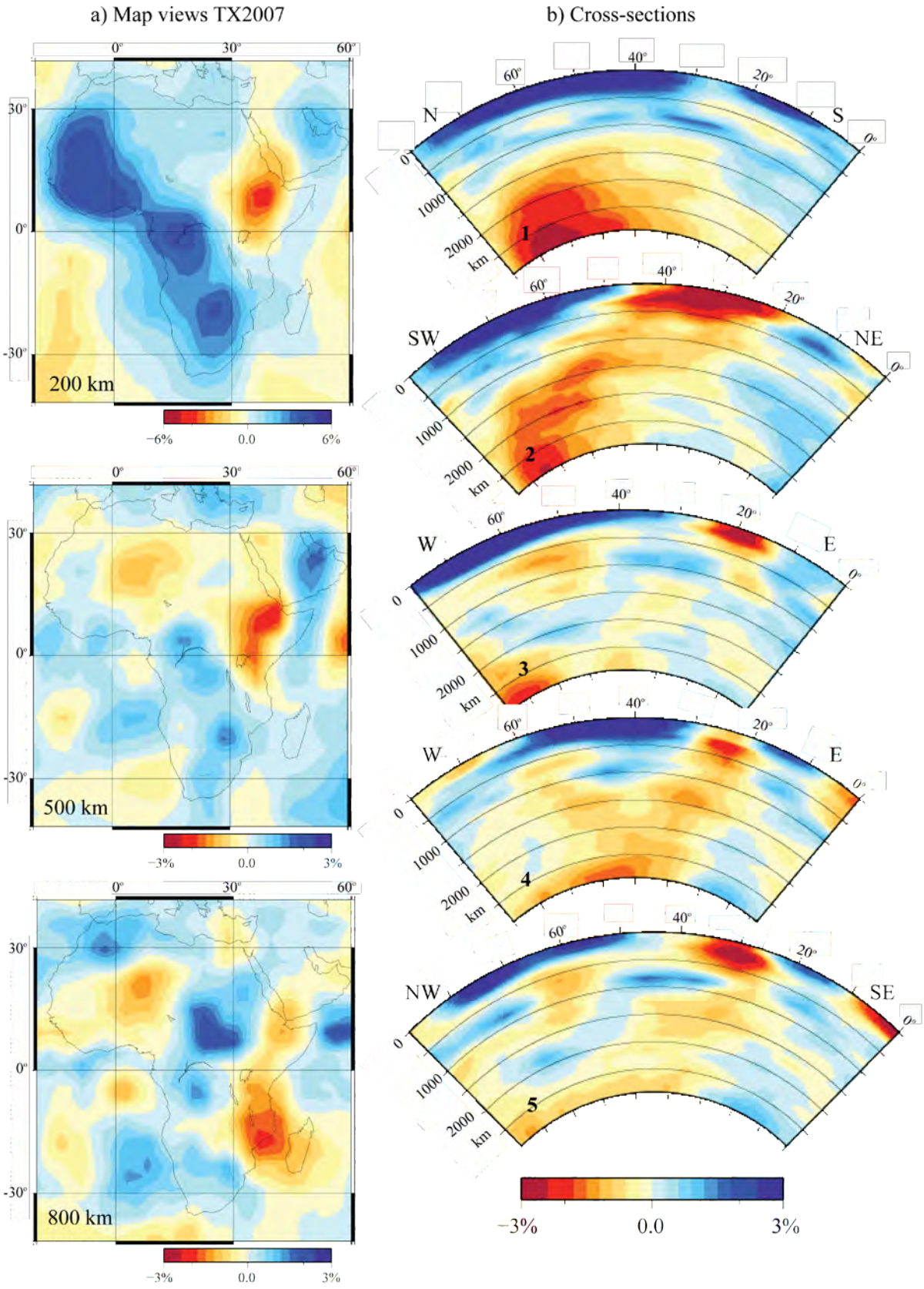
a) Map views TX2007
b) Cross-sections
200 km
500 km
800 km
−6%
0.0
6%
−3%
0.0
3%
N
S
SW
NE
W
E
W
E
NW
SE
1
2
3
4
5
km

c) 3D views

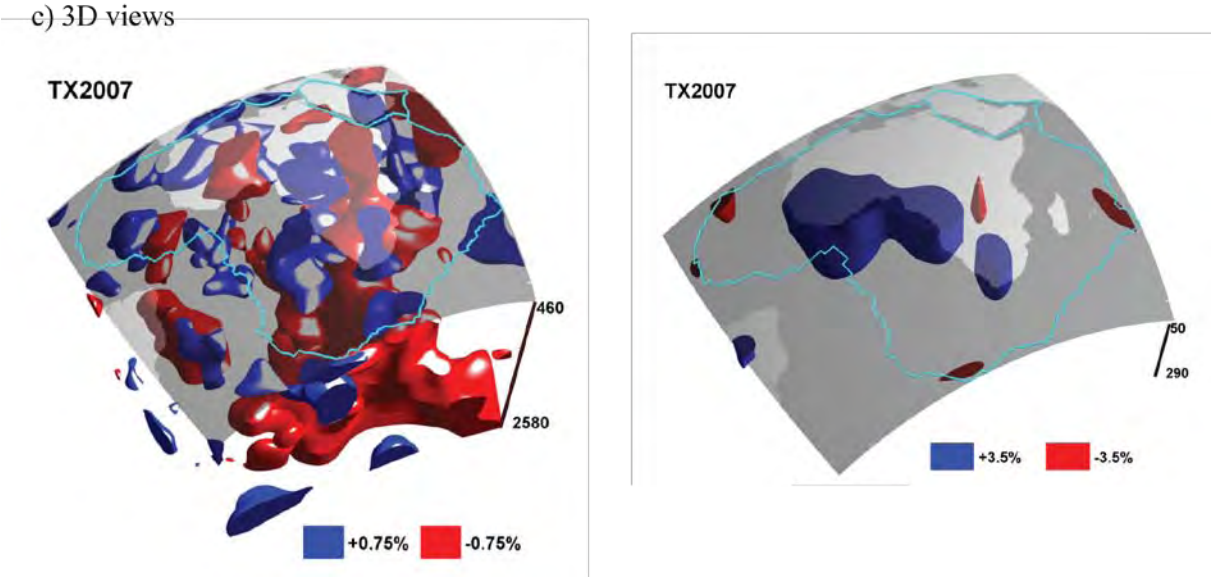

d) Location of cross-sections

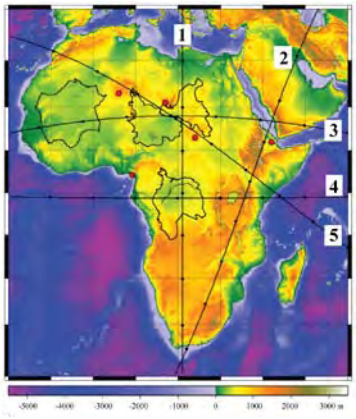

Figure 16: TX2007 (S-wave model). a) Map views, b) cross-sections c) 3D views, and d) locations of cross-sections.

2.3 Upper mantle tomography models

We visualise 5 upper mantle tomography models (*Table 1 and 2, Figs. 17-21, Appendix A*) by:

- Horizontal map views at 200 km depth (at or through the base of the lithosphere) (CU_STD1.0, CU_SRT1.0, KP08, LH08, SF09) and at 500 km depth (model LH08)
- 3D iso-surfaces at ±3.5% velocity anomaly

KP08 (Priestley et al., 2008) and SF09 (Fishwick, 2010) are models specifically derived for Africa, CU_STD1.0, CU_SRT1.0 (Shapiro and Ritzwoller, 2002) and LH08 (Lebedev and van der Hilst, 2008) are global models. Upper mantle tomography models use normal mode seismology to resolve structure in the upper 200-300km of the Earth. The various global and regional upper mantle models described here use fundamental modes (surface waves) and higher modes (S-waves), which are more sensitive to structure at these depths than other wave types. The methods used in these upper mantle models are quite different than the global tomography models, because they include group velocities (from overtones) in addition to phase velocities. Overall, these five models resolve the cratonic lithosphere under Africa (West Africa, Congo, Kalahari) fairly well. However, it is important to note that these models are not in complete agreement over the shape, size and location of cratonic structure. Similar

to the whole mantle models, the upper mantle models consistently image low velocities around Afar and the Red Sea.

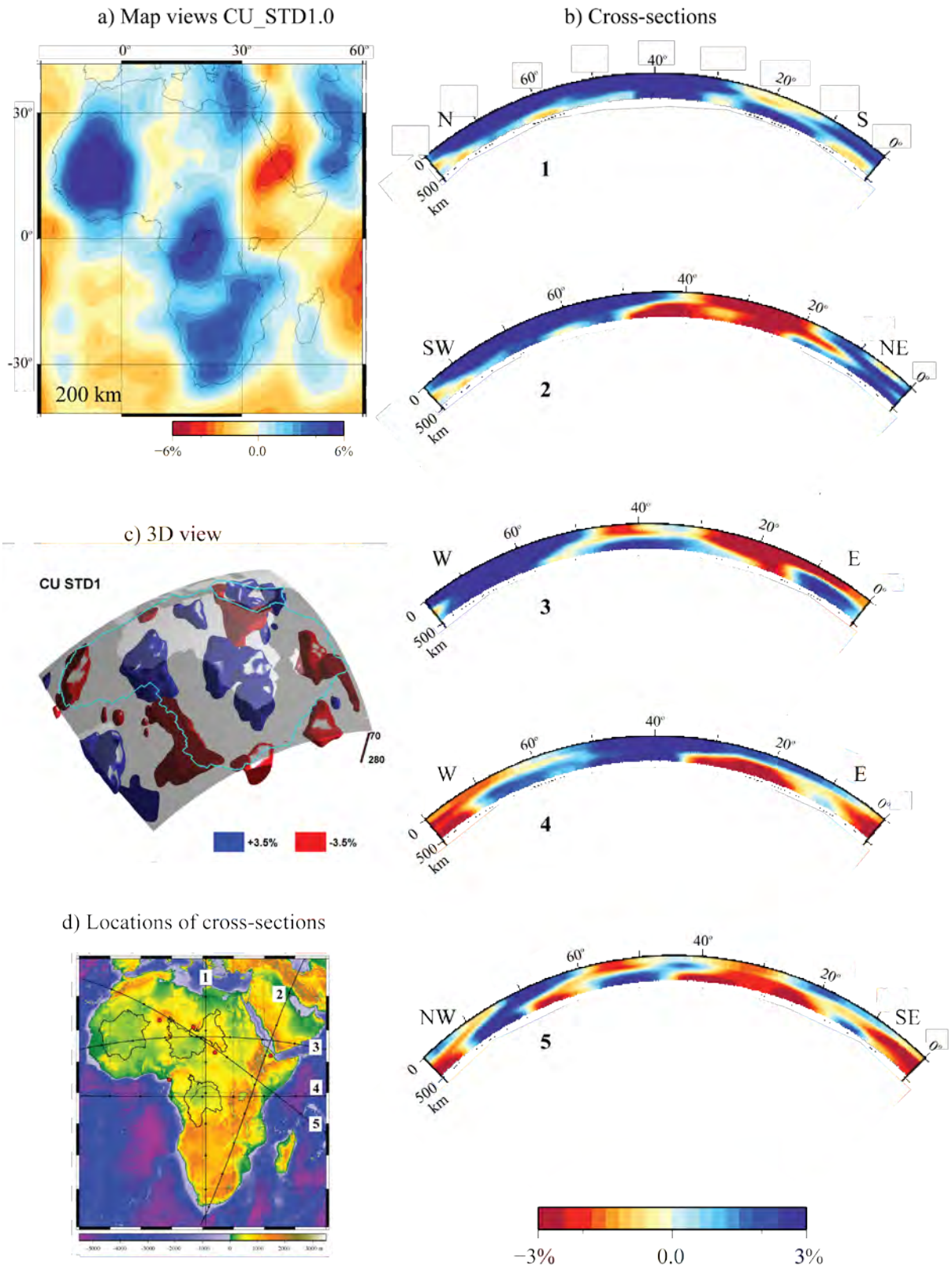

Figure 17: CU_STD1.0. a) Map views, b) cross-sections, c) 3D view and d) locations of cross-sections.

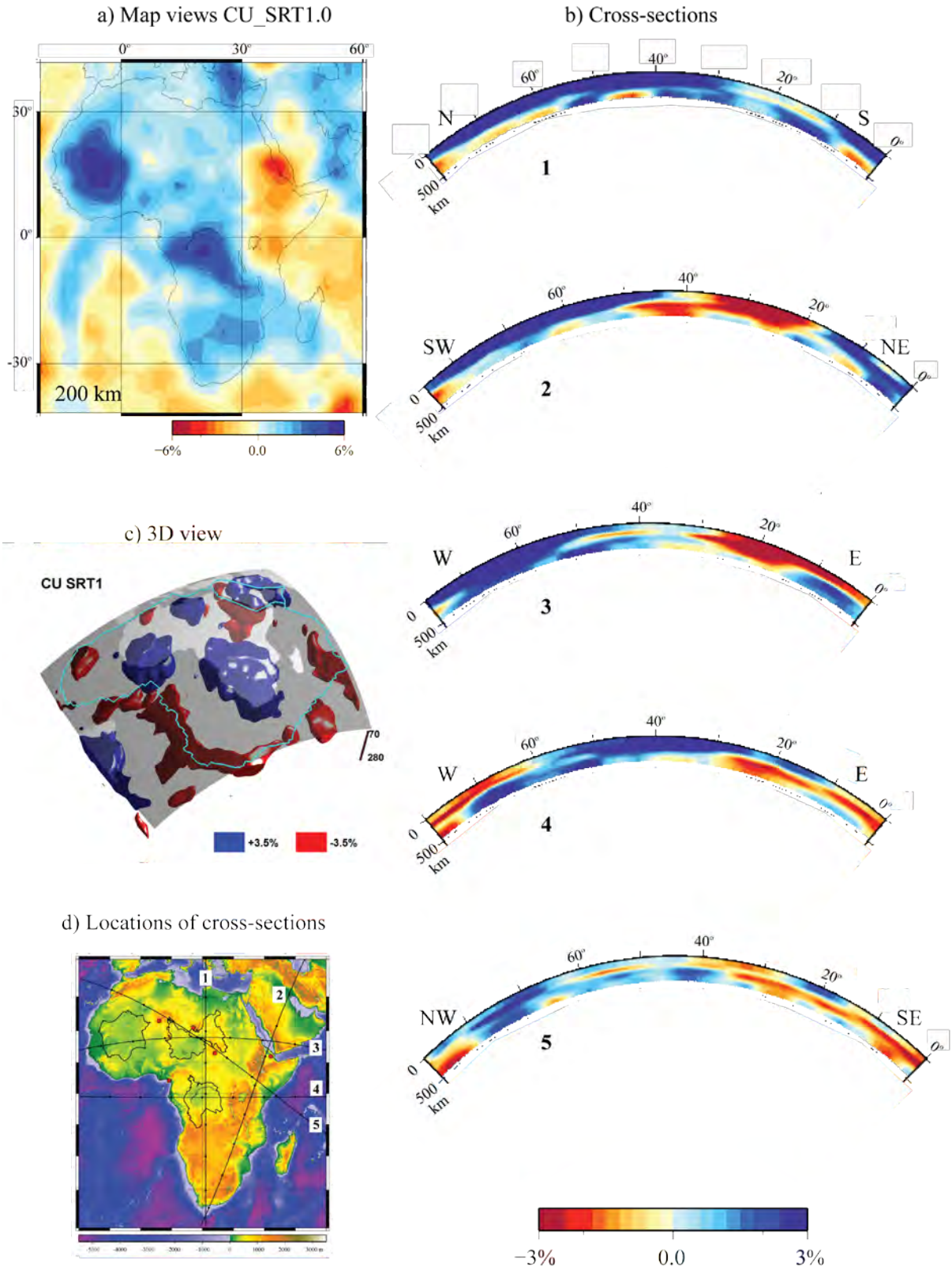

Figure 18: CU_SRT1.0. a) Map views, b) cross-sections, c) 3D view and d) locations of cross-sections.

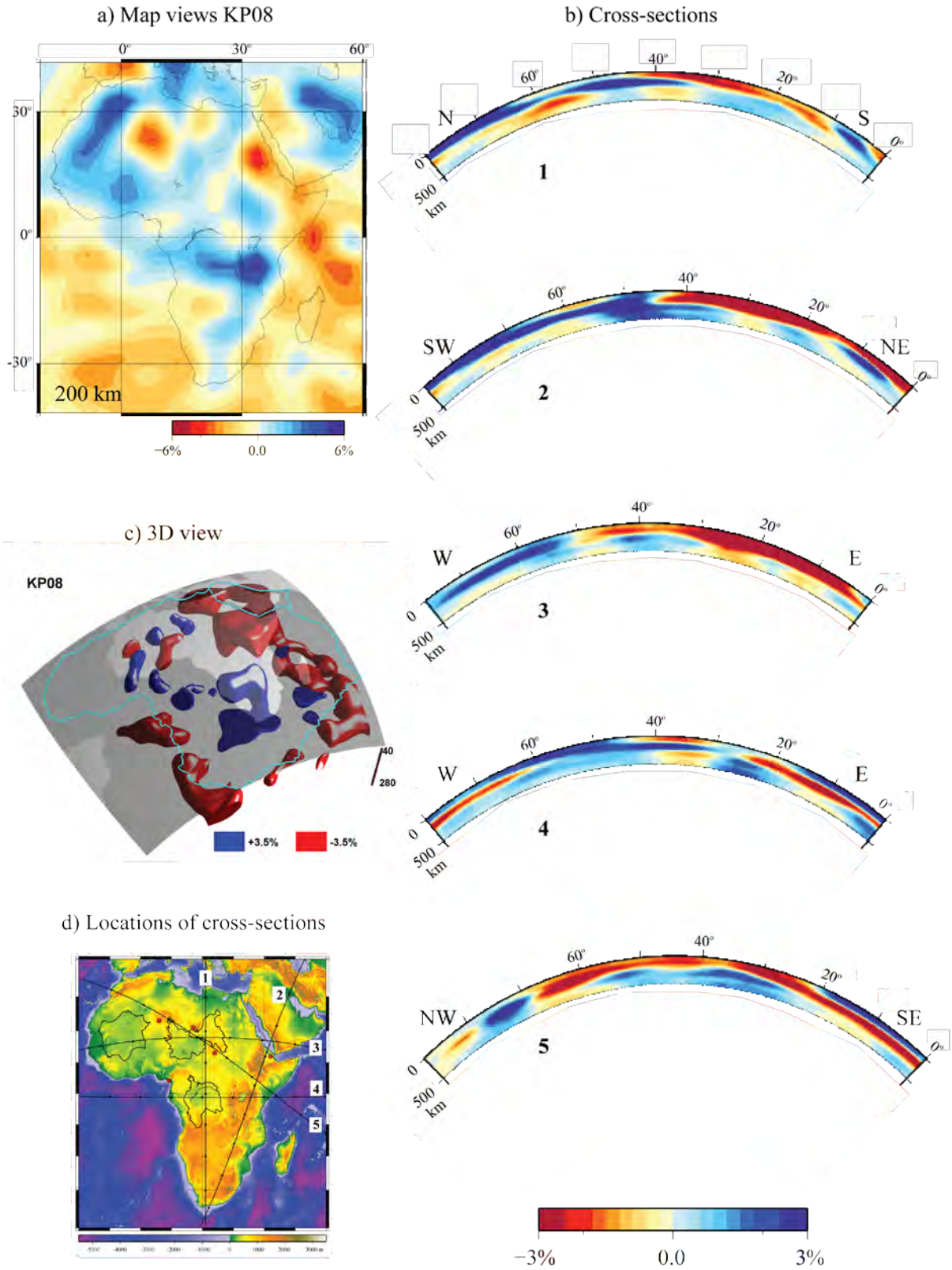

Figure 19: KP08. a) Map views, b) cross-sections, c) 3D view, and d) locations of cross-sections.

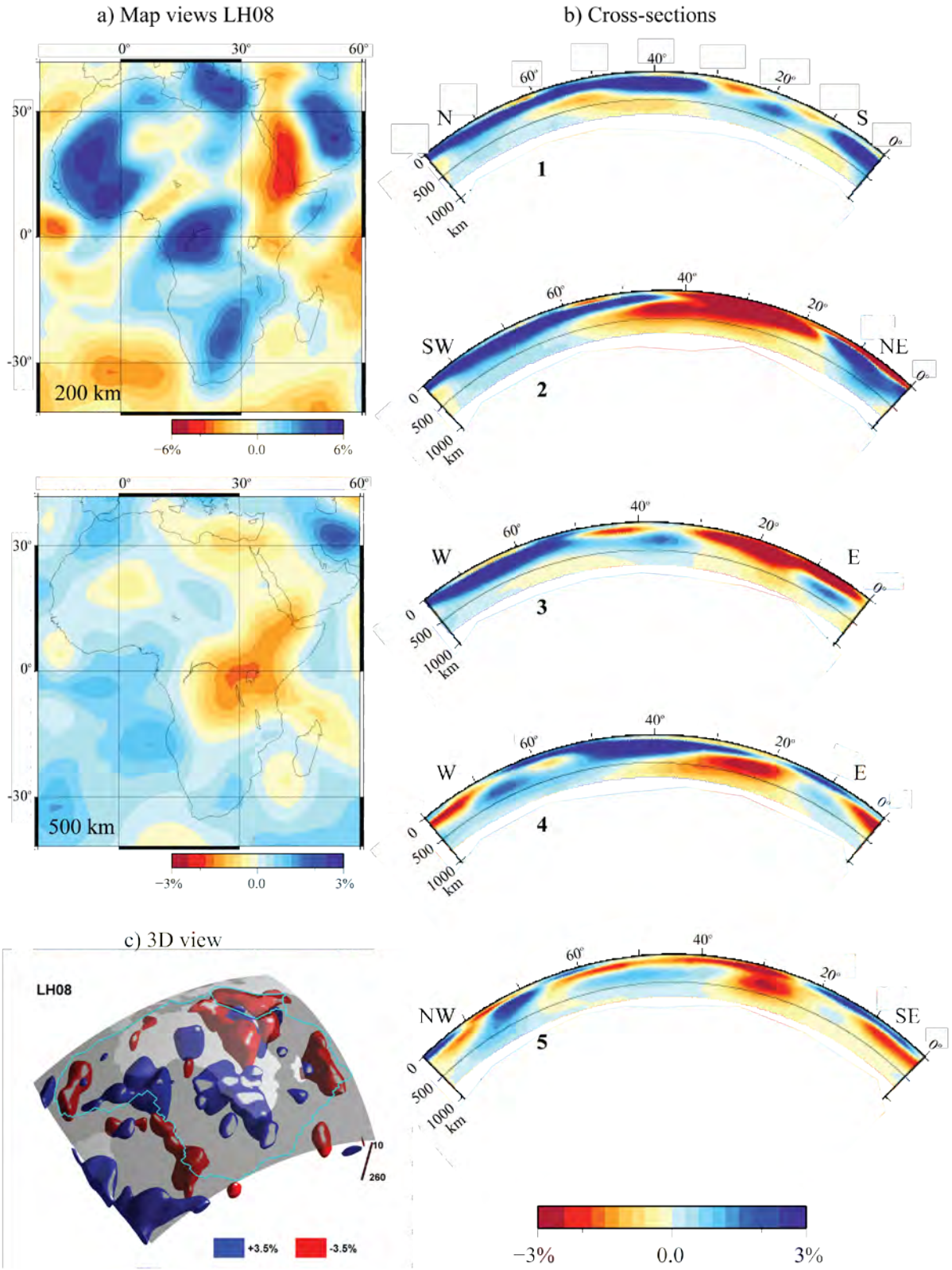

Figure 20: LH08. a) Map views, b) cross-sections, and c) 3D view.

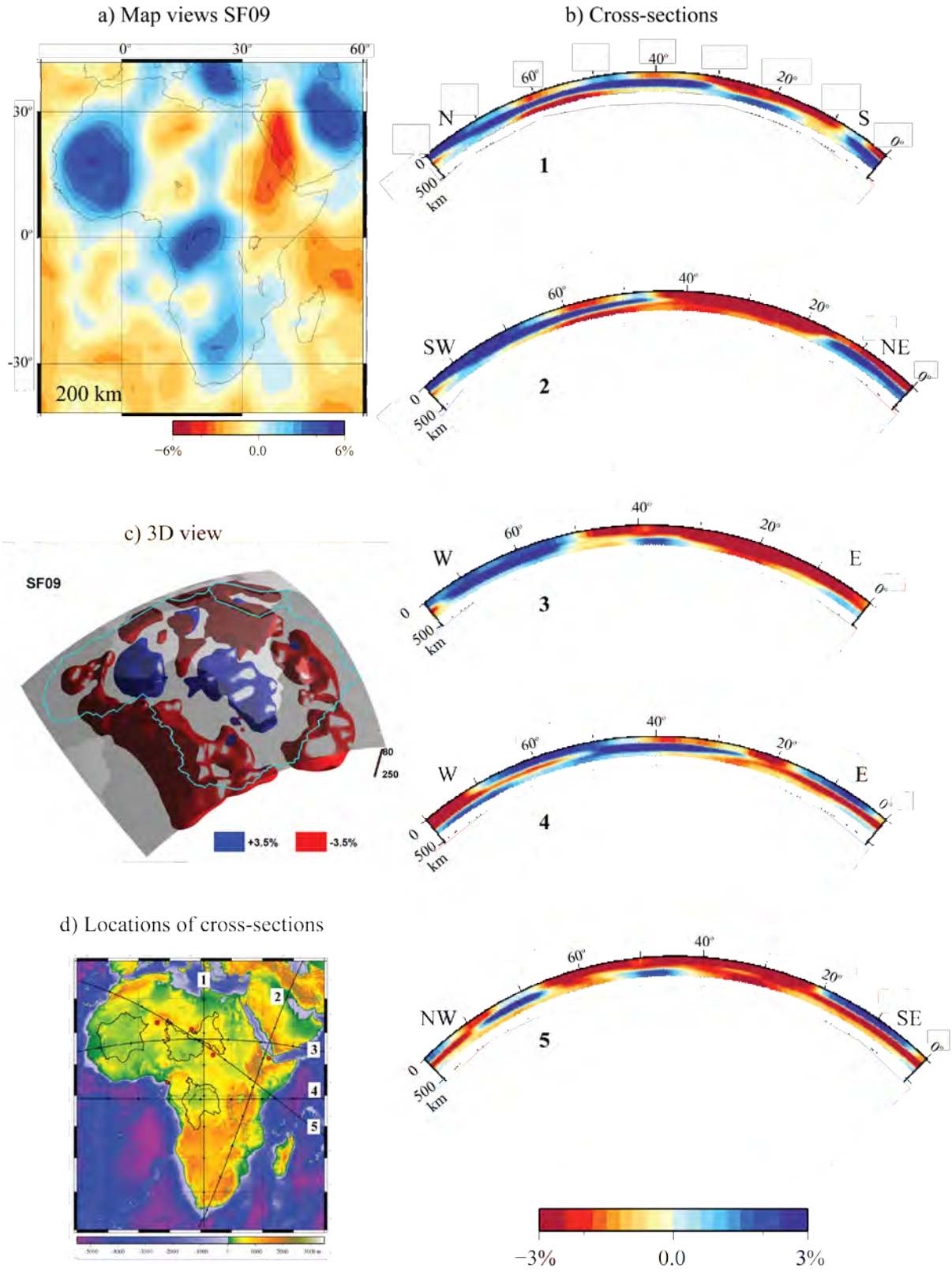

Figure 21: SF09. a) Map views, b) cross-sections, c) 3D view, and d) locations of cross-sections.

2.4 MIX-A: A new mean model of whole mantle tomography

Comparison of the 12 whole mantle tomography models (*Figs. 4-16*, Tables 1 and 2, Appendix A) indicates that there are substantial differences in detail, but that all models agree on the largest-scale features. It can hence be useful to average over several tomography models, with the expectation that unreliable features (in which the models differ) are averaged out, whereas the reliable features (in which the models agree) remain. The approach of constructing mean models was pioneered by Becker and Boschi (2002), who constructed their SMEAN model by averaging over SB4L18, S20RTS and an older version of Grand's model (University of Texas), similar to SG06. More recently, Trond Torsvik (pers. comm.) constructed the model SIXMEAN as an average of six tomography models in the lowermost mantle and Lee et al. (in press) construct the mean and empirical co-variance of six tomography models. Here this trend is continued by constructing the weighted mean of a total of eight whole-mantle tomography models. We choose the eight models that give the best fit (in terms of variance reduction) of predicted dynamic topography to observation-based residual topography (see section 5), with the exception of SG06 which is similar to TX2007, but gives a slightly worse fit. Then always two models are mixed by adding x % of one model and 100-x % of the other. x is varied from 0 to 100 in increments of 10. The mix that gives the best fit (in terms of variance reduction) is kept for the next round. In the first round, TOPOS362 and P362D28, TX2007 and S20RTSb, SAW24B16 and SAW642AN, PRI-S and PRI-P are mixed. The resulting models are called Harvard, Midwest, Berkeley and Princeton. In the second round, we mix Harvard and Princeton to a model “East”, and Midwest and Berkeley to a model ”West”. In the third round “East” and “West” are mixed. The resulting model is called MIX-A and consists of 4.8% TOPOS362D1, 7.2% P362D28, 10.8% TX2007, 1.2% S20RTSb, 11.2% SAW24B16, 16.8% SAW642AN, 28.8% PRI-S05 and 19.2% PRI-P05 (*Fig. 22*). P-wave models are additionally scaled according to different velocity-to-density scaling (*Fig. 25*, section 4.1). Typically mixing of two models averages out some features. This makes it easier to see "the big picture". However, MIX-A contains a large fraction (> 50 %) of models with low amplitude at lithosphere depth and therefore itself also has rather low amplitudes there. This enables a better fit of dynamic to residual topography (see section 5), but is not necessarily realistic.

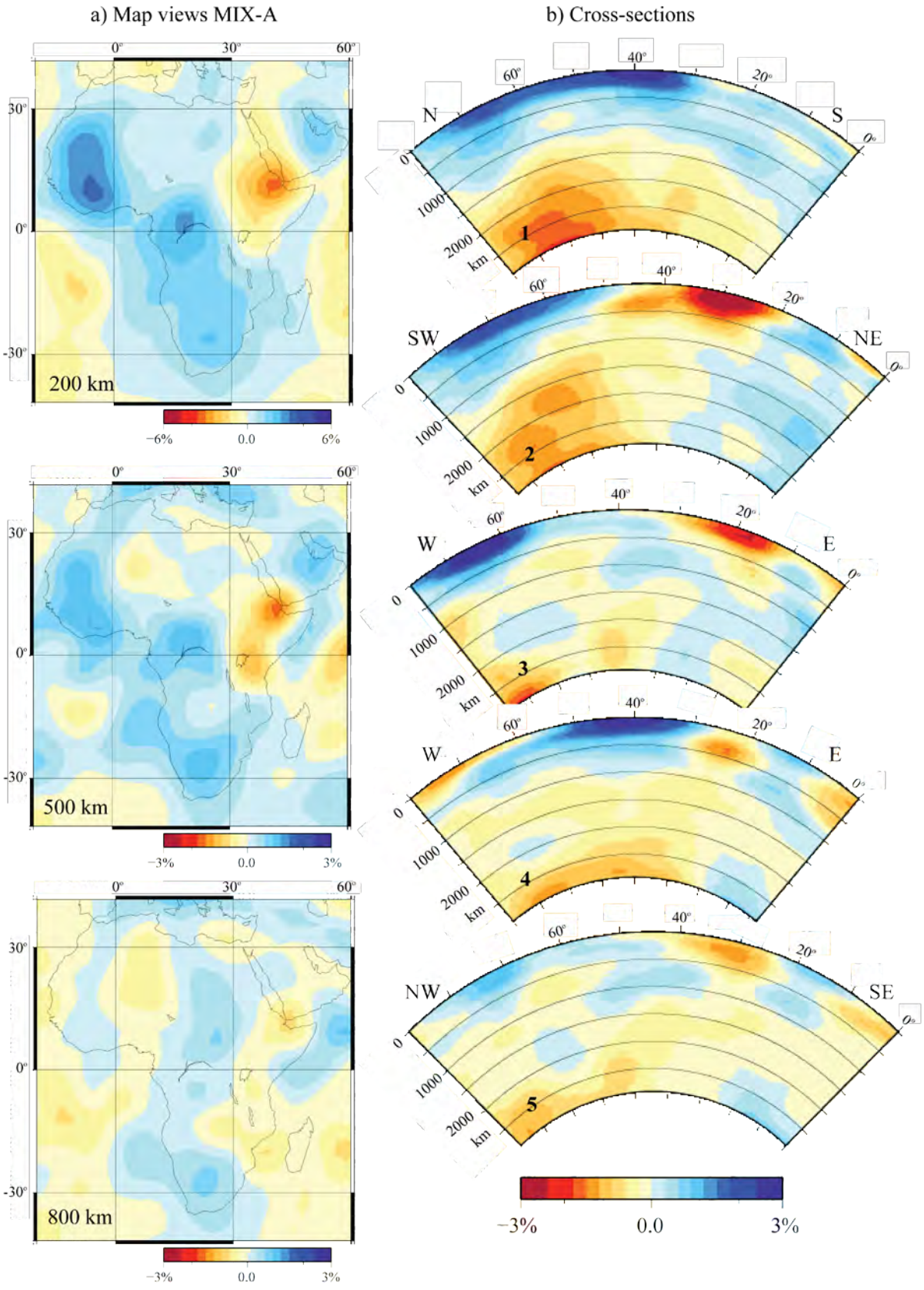
a) Map views MIX-A
b) Cross-sections
200 km
500 km
800 km
−6%
0.0
6%
−3%
0.0
3%
N
S
SW
NE
W
E
W
E
NW
SE
1
2
3
4
5
km

c) 3D views

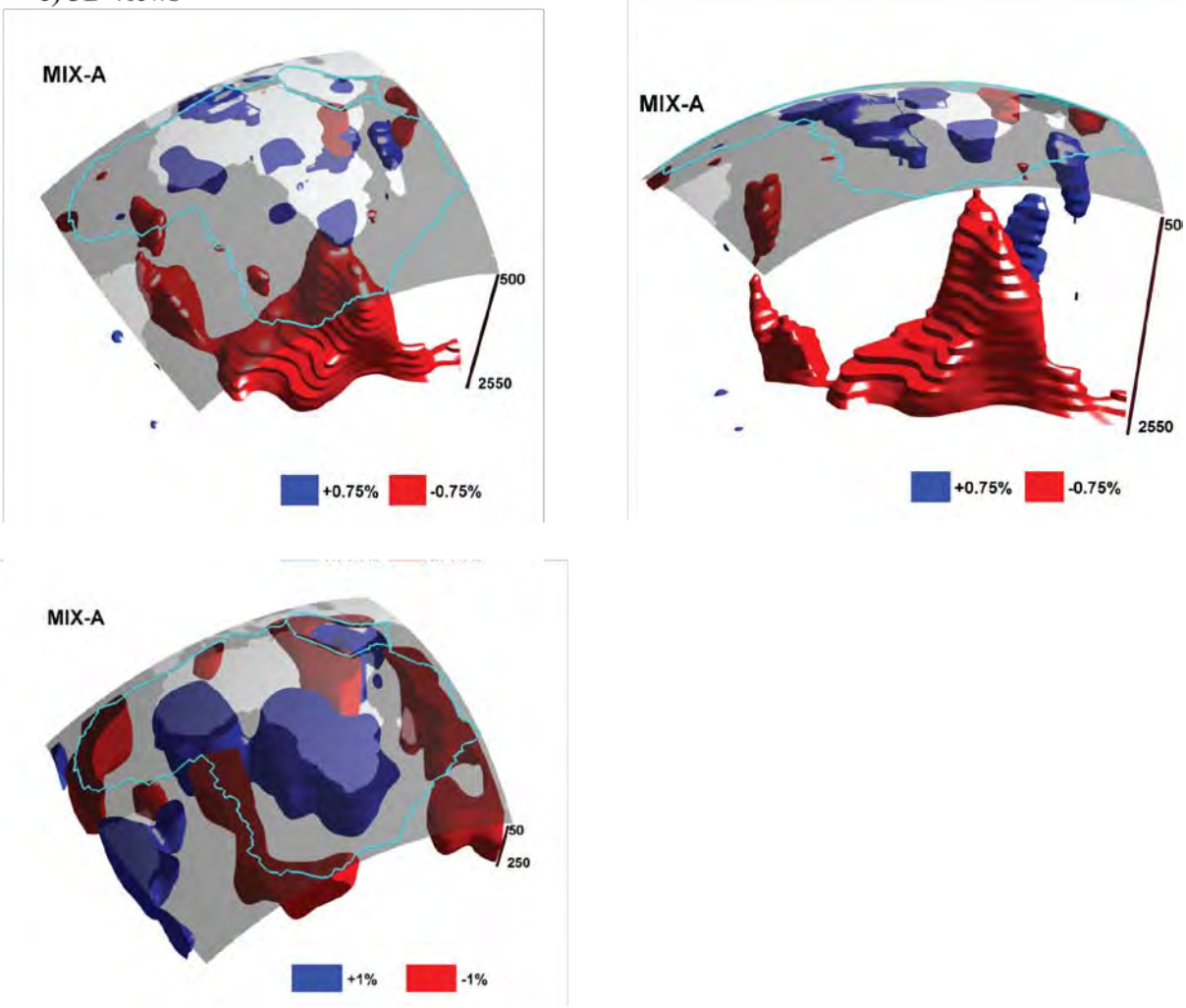

d) Location of cross-sections

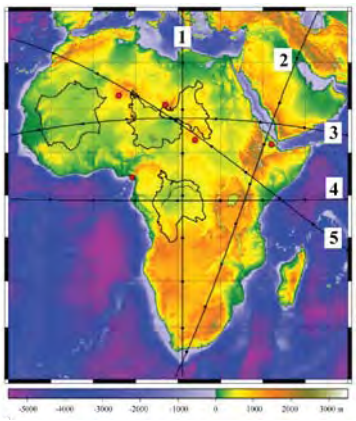

Figure 22: MIX-A (mix of 8 S- and P-wave models). a) Map views, b) cross-sections, c) 3D views, and d) location of cross-sections.

3. CRUST AND LITHOSPHERE THICKNESS

The computation of dynamic topography requires a model for the crust and lithosphere thickness. For crustal thickness we use CRUST2.0 (Bassin et al., 2000; http://igppweb.ucsd.edu/~gabi/rem.html, *Fig. 23*). The depth to the base of the lithosphere can be derived from tomography models (e.g., Conrad and Lithgow-Bertelloni, 2006) or from thermal, seismic and/or geological observations. *Fig. 24* shows a compilation of five models of lithosphere thicknesses for Africa. The global model of Conrad and Lithgow-Bertelloni (2006) (*Fig. 24a*) is obtained from S20RTSb (Ritsema et al., 2004) by equating the maximum depth for which the velocity anomaly is consistently greater than +2% with lithosphere depth. The global thermal model for continental lithosphere of Artemieva (2006) (*Fig. 24b*) shows thermal lithosphere thickness based on continental geotherms and tectonic age of the basement. The model of Rychert et al. (2010) (*Fig. 24c*), based partly on Rychert and Shearer (2009), is a global compilation of seismic observations of what is interpreted as the lithosphere-asthenosphere boundary. It has only limited data points. The Africa lithosphere model of Crosby et al. (2010; pers. comm. Fishwick) (*Fig. 24d*) was obtained by converting the tomography model of Fishwick, SF09, into temperature and using a geothermal gradient to derive lithosphere thickness. The Africa lithosphere thickness model of Pasyanos and Nyblade (2007, lithosphere thickness model pers. comm.) (*Fig. 24e*) is the result of a grid search that fits synthetic velocity profiles to average surface wave dispersion data. The lithosphere models that are based on tomography, i.e., S20RTSb/Conrad and Lithgow-Bertelloni (2006), SF09/Crosby et al. (2010) and Pasyanos and Nyblade (2007) (*Fig. 24a, c and d*), all clearly show the thick lithosphere associated with the West African, Congo and Kalahari cratons (see also Fig. 1b). The thin lithosphere of the Red Sea rift (Fig. 1a) is visible in the models of Artemieva, Crosby, Pasyanos and Rychert, but not in the model of Conrad. The East African Rift shows in the models of Artemieva and Pasyanos, while the Cameroon line is visible in Crosby and Pasyanos.

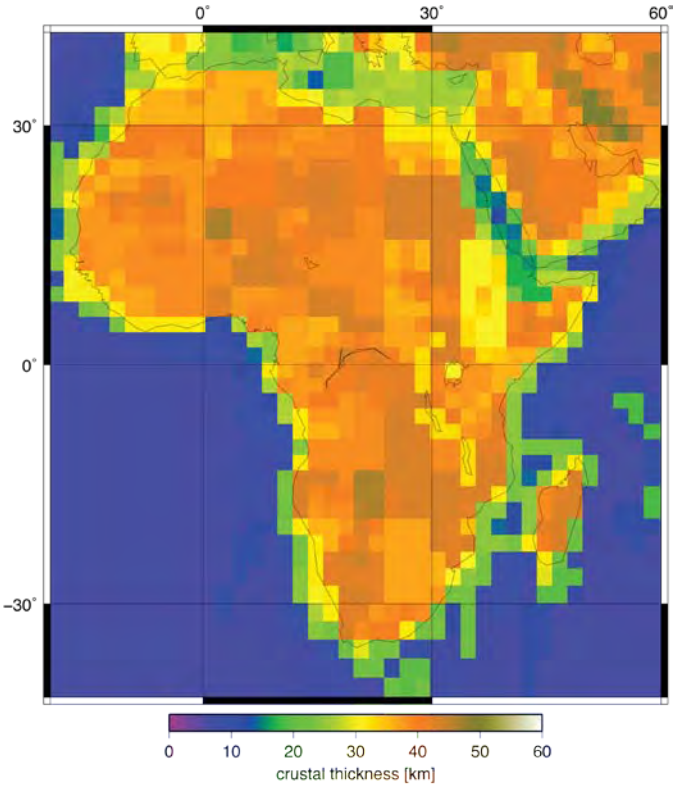

Figure 23: Crustal thickness in Africa from CRUST2 (http://igppweb.ucsd.edu/~gabi/rem.html).

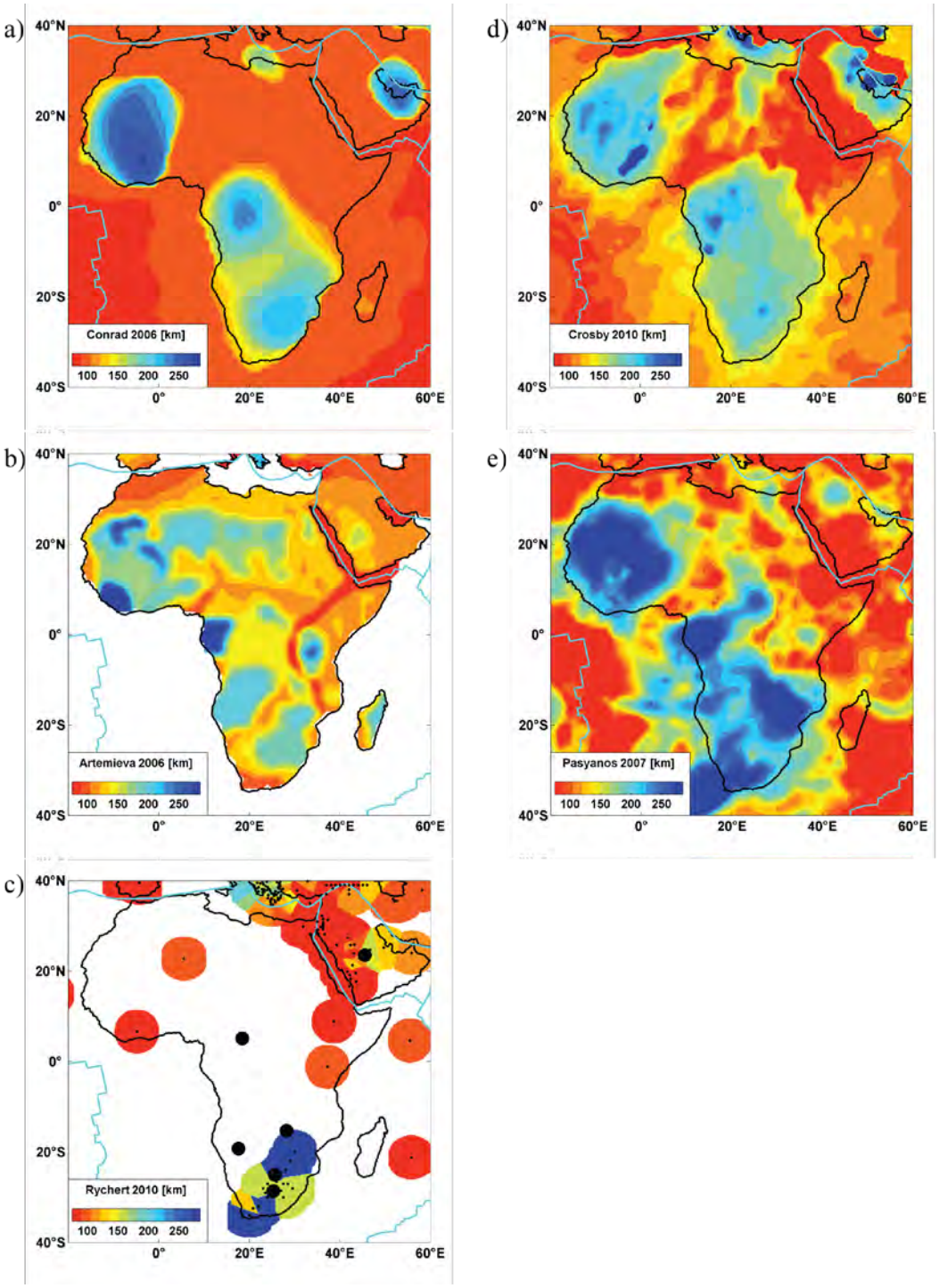

Figure 24: African lithosphere thickness models. a) Conrad and Lithgow-Bertelloni (2006), based on tomography model S20RTSb, b) Thermal lithosphere model from Artemieva (2006), c) Rychert et al. (2010). The thickness of the lithosphere was constrained by several data points (indicated by the small black dots) by assuming a constant lithosphere thickness within a 5 arc-degree from the data point. Large black circles indicate the position of points with controversial data (two or more points within 10 arc minutes and with difference in lithosphere thickness >50 km), these data points were ignored. d) Obtained from tomography model SF09, Crosby et al. (2010), and e) Obtained from the tomography model of Pasyanos and Nyblade (2007).

4. METHODS

4.1 Advection of mantle density anomalies and computation of dynamic topography

We first derive a mantle density model and the dynamic topography it causes for the present-day. The density model is derived from a weighted average of several recent tomography models. Using a thermal conversion factor, seismic velocity anomalies are converted to density anomalies everywhere, except within the lithosphere, for which we replace the velocity anomaly by a constant (and small) value. We use various lithosphere models to "cut out" the lithosphere from the tomography models in that way. The weighted average is chosen such that the fit between modelled dynamic topography and residual topography (actual topography minus topography isostatically compensated in the crust) is optimized. We mostly use the CRUST2.0 model (*Fig. 23*), but examine other crustal models as well.

We compare dynamic and residual topography by computing their correlation and ratio:

- globally
- in certain regions: continents, oceans, the African plate, the African continent
- spectrally, i.e. as a function of spherical harmonic degree
- regionally in caps of 30 degrees of arc around each point of a global 2-degree grid.

Discrepancies between dynamic and residual topography may be due to errors in either of them. We attempt here to distinguish between the two cases by considering how the observed ratio of residual topography and geoid as a function of spherical harmonic degree relates to the ratio that is "expected". This "expected" ratio is computed from a statistical model of mantle density anomalies (i.e. spectral characteristics and radial correlation) that is inferred from mantle tomography models. Discrepancies between the observed and expected ratio can be attributed to amplitude errors in the residual topography.

We then advect density anomalies backward in the computed flow field, in order to compute density models and the related dynamic topography in the geologic past. However, this procedure becomes increasingly inaccurate further back in the past, because diffusion cannot be adequately computed backward. Nevertheless, we compare here results of a pure backward advection model, and a modified model, in which we consider diffusion backward in time. We combine the backward advected model with a model of plate motions in order to compute how points that move with the plates move upward and downward over time.

The density model is inferred from tomography, but considering that the seismic velocity anomalies in the lithosphere likely do not correspond to density anomalies (see next section for details). Dynamic topography is computed with a viscous flow model that only considers radial viscosity variations (Hager and O'Connell, 1979, 1981). We use Model M2b of Steinberger and Calderwood (2006) for the radial viscosity structure. Stresses acting on the lithosphere are converted to topography using a density contrast 3300 kg/m^3, corresponding to the density of the uppermost mantle. That means, dynamic topography is computed "beneath air". To account for coverage with water (density 1020 kg/m^3, thus density contrast 2280 kg/m^3) we divide the observation-based "residual topography" by 3.3/2.28=1.4473684 rather than using different conversion factors from stress to topography on land and beneath the sea. For the actual dynamic topography computations we use a free-slip upper boundary condition, but different from that, we use prescribed plate motions to compute the advection of density anomalies in the time-dependent computations (see section 5 for details).

A negative density anomaly at any depth always causes positive dynamic topography, but the amount depends on the depth of the density anomaly and the viscosity structure. The amount of topography or geoid that a density anomaly at a given depth and given spherical harmonic degree causes can be described by topography or geoid kernels. *Fig. 25* (top) shows kernels for the viscosity structure and top boundary condition used here. It is meant to be appropriate as a "global average". For comparison, the bottom case may be more appropriate for the interior of a rigid plate. Topography kernels in this case are not too different, and we use the top case in the following. For a more detailed explanation, see Steinberger et al. (2010) and Steinberger and Holme (2002). We restrict ourselves to degrees ≤ 31, as higher degrees are likely dominated by lithosphere contribution and also less well constrained in tomography models.

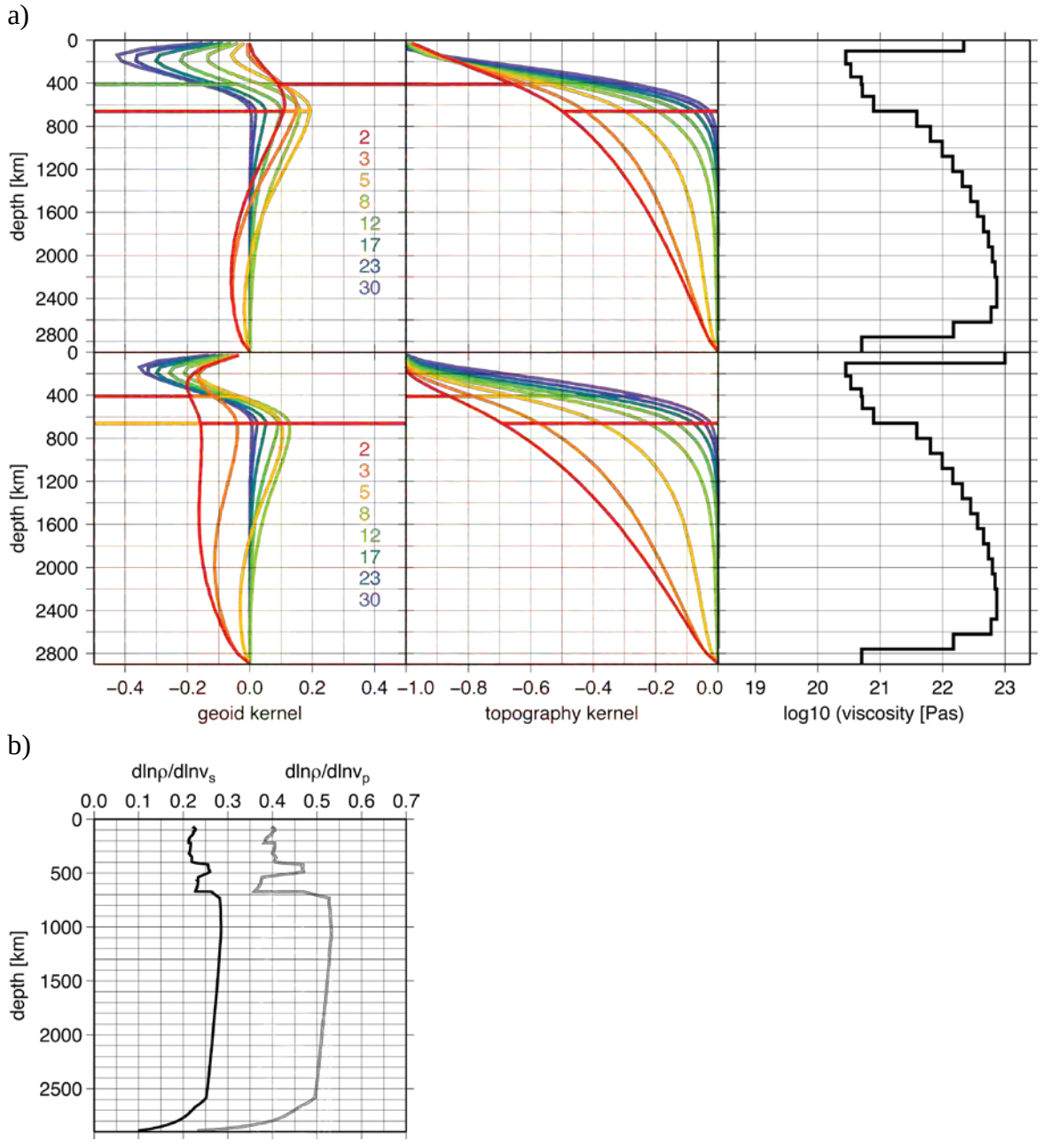

Figure 25: a) Geoid (left) and topography (center) kernels for viscosity models (right). Top: stress-free surface; viscosity model M2b. Bottom: surface is normal-stress-free but with zero horizontal motion. Same viscosity structure except for higher viscosity lithosphere. b) Scaling of relative seismic P- and S-wave velocity variations to relative density variations as a function of depth, assuming they

are due to temperature variations. Scaling for S-waves is from Steinberger and Calderwood (2006), for P-waves from Steinberger and Holme (2008) - see there for original references where applicable

4.2 Computation of lithosphere deformation

To examine the potential effects of including a deformable lithosphere with a free surface in the mantle flow models, we couple the mantle models to lithosphere models in a simple manner (section 7). For the lithosphere models we solve the incompressible momentum equation for slow creeping flows:

$$\nabla \bullet \left(\sigma' - P\right) + \rho g = 0$$

$$\nabla \bullet u = 0$$

σ' is the deviatoric stress tensor, P dynamic pressure, ρ density, g gravitational acceleration (g_x = 0 ms^{-2} and g_y = 9.81 m s^{-2}), and u velocity. The dynamic pressure (mean stress) is computed using an iterative penalty (Uzawa) formulation. The equations are discretised on a structured grid of quadrilateral elements that are continuous in velocity, but discontinuous in pressure. We have here only used linear elements (4 velocity nodes with 2 degrees-of-freedom each and constant in pressure). Our materials behave either viscous or plastic. Temperature dependent power-law flow follows:

$$\sigma_2^{'} = A^{-1/n} \dot{\varepsilon}_2^{'1/n} e^{\frac{Q+PV}{nRT}}$$

A, n, Q and V are the power-law pre-exponent, power, activation energy and activation volume, respectively, R is the gas constant, T is temperature, σ_2 and $\dot{\varepsilon}_2^{'}$ are the second invariants of the deviatoric stress tensor and strain-rate tensor, respectively. In the models in this report we do not solve for temperature, but instead advect initial temperatures, similar to what is done for the mantle flow models. Plastic failure occurs when the deviatoric stress reaches the yield stress:

$$\sigma_2^{'} = P \sin\phi + C \cos\phi$$

ϕ is angle of internal friction and C is cohesion. We solve these equations using SULEC (developed by Susanne Buiter and Susan Ellis; Buiter and Ellis, in prep; Ellis and Buiter, in prep). SULEC is an arbitrary Lagrangian Eulerian finite element code that solves the mechanical and thermal equations on a slightly deformable Eulerian grid. This approach gives a true free surface behaviour and the possibility to examine the effects of erosion and sedimentation. Material flow is tracked with tracer particles. The code has been benchmarked against numerous analytical solutions and numerical multi-code studies.

5. PRESENT-DAY DYNAMIC TOPOGRAPHY

5.1 Mantle density model inferred from whole-mantle tomography models

We use the 13 global tomography models described in section 2.1, Tables 1 and 2, and Appendix A. Except within the continental lithosphere, we convert seismic S-wave speed to density variations (Model M2b of Steinberger and Calderwood, 2006) assuming they are both caused by temperature variations. The conversion factor from relative S-wave speed to relative density variations is about 0.25 throughout the mantle (*Fig. 25)*. Conversion from P-wave speed to density is performed in a similar manner, as described in Steinberger and Holme (2008) (*Fig. 25).*

Seismic velocity variations within the continental lithosphere, however, are disregarded. Instead, a constant cut-off density value is used. We define the continental lithosphere with the following procedure, which is applied everywhere beneath the continents (defined with an elevation above 800 m below sea level): Any gridpoint between 400 and 60 km depth is assigned to the lithosphere, if the seismic velocity anomaly at the gridpoint itself and at all gridpoints above but below 60 km depth exceeds the value that corresponds to the cut-off density (using the thermal conversion factor). Gridpoints above 60 km depth are assigned to the continental lithosphere, if the shallowest gridpoint below was assigned to the continental lithosphere. This is done because seismic velocity variations above 60 km may correspond to crustal thickness variations. The constant density anomaly in the lithosphere is assigned through optimizing the fit between dynamic and residual topography (in terms of variance reduction; see section 5.2 for details) and is typically found to be around zero. The procedure is illustrated in *Fig. 26*, where we show an example cross section through both a tomography model and the inferred density model.

If seismic velocity variations within the continental lithosphere were converted to density variations in the same way as elsewhere, dynamic topography would be severely over-predicted (see section 5.2). This finding corresponds to the isopycnic hypothesis (Jordan, 1988). It should be noted that also in the Large Low Shear Velocity Provinces of the lowermost mantle the "thermal" conversion of seismic velocity variations to density variations is probably inappropriate, as they are most likely chemically distinct (see e.g., Torsvik et al., 2006 for a review of evidence). However, as dynamic topography kernels are small in the lowermost mantle, this has little effect on the predicted dynamic topography, and is hence disregarded here.

From the dynamic topographies computed in this way, we subtract topography that is assigned to lithosphere cooling of the ocean floor. We use the digital age grid of the ocean floor (Version 3.6) from Müller et al. (2008a) and compute that part of topography as $(1-(\text{age}/100\ \text{Ma})^{0.5}) \cdot 3000$ m for an age less than 100 Ma and zero elsewhere. To convert to "beneath air", this topography is also divided by 1.4473684. The same topography is also subtracted from the residual topography (see next section for more discussion on this).

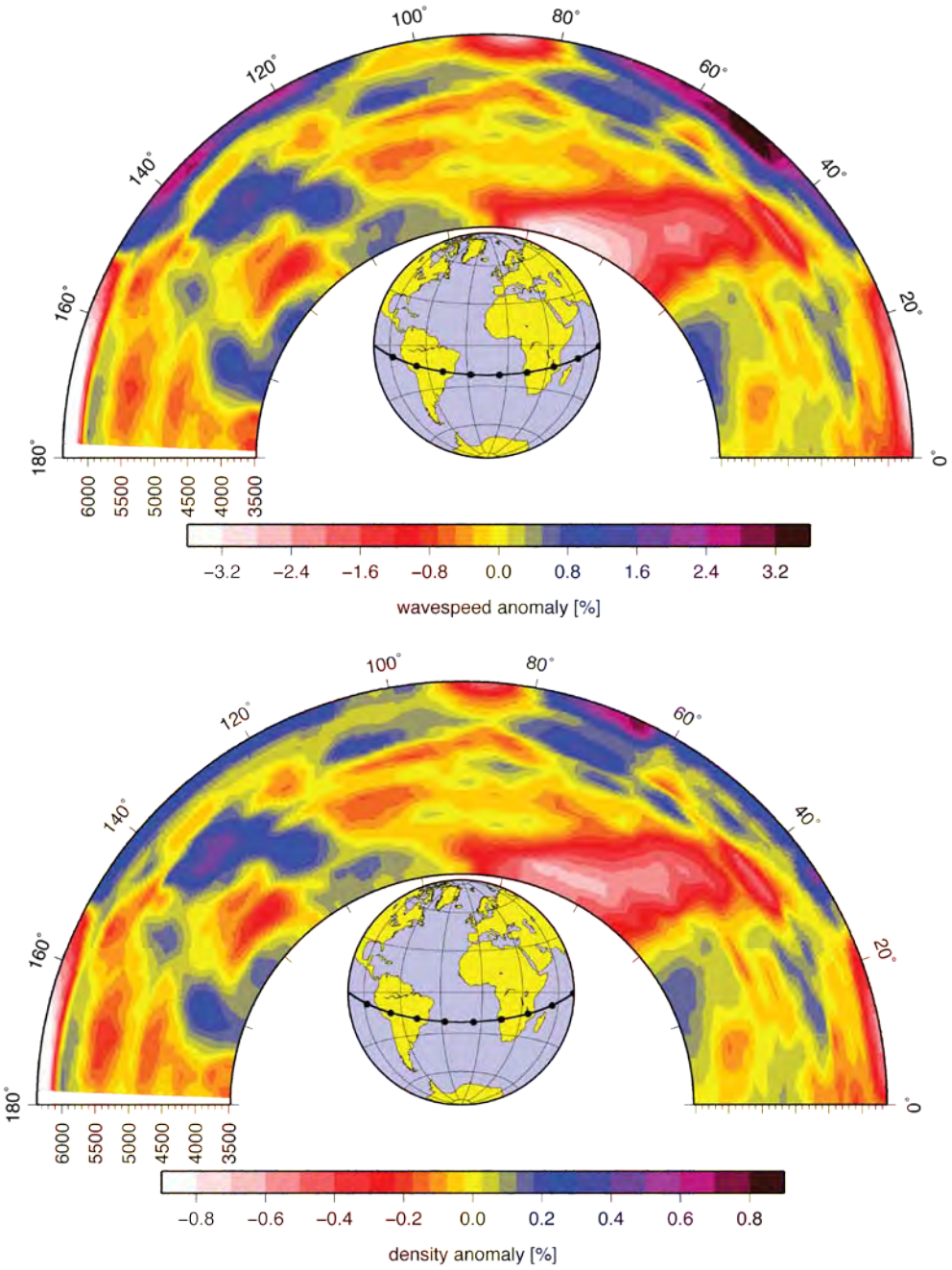

Figure 26: Example cross section through seismic velocity anomaly (model TX2007; above) and inferred density anomaly (below), with lithosphere removed as described in the text (cut-off S-wave anomaly 0.2%). At each depth level, density anomalies are re-calibrated to zero mean, which causes a variation of resulting density anomaly with depth even within the lithosphere.

5.2 Comparison of predicted dynamic topography with observation-based residual topography

For the present-day the computed dynamic topography is compared to the so-called ”residual” topography. This is computed by subtracting topography due to an isostatically compensated crust from the actual topography. We use the CRUST2.0 model (available online at http://mahi.ucsd.edu/Gabi/rem.html) (*Fig. 23*). Residual topography beneath the oceans is divided by a factor 3.3/2.28=1.4473684 to compensate for water coverage (instead of dividing dynamic topography by the same factor beneath the sea). Subsequently, for consistency we

also subtract the same topography due to ocean floor cooling (divided by factor 1.4473684) as in the last section.

We compute both correlation and amplitude ratio of dynamic and residual topography globally, in oceans only, in continents only, on the African plate only, and on the African continent only. A large positive correlation, and a ratio close to 1, corresponds to a good fit. As a measure of overall fit we also compute the variance reduction Variance(Predicted-Observed)/Variance(Observed). These correlations and ratios are computed for degrees 1-31 and 1-12. Furthermore, we compute correlation and ratio individually for each spherical harmonic degree. In this way, we can assess how the fit depends on the wavelength range considered. We also compute them regionally for each point in a cap of 30 degrees of arc radius around that point, thus assessing regional variations in fit. As an example, we show again results for TX2007 in *Fig. 27*. Results for all other models considered are shown in Appendix A.

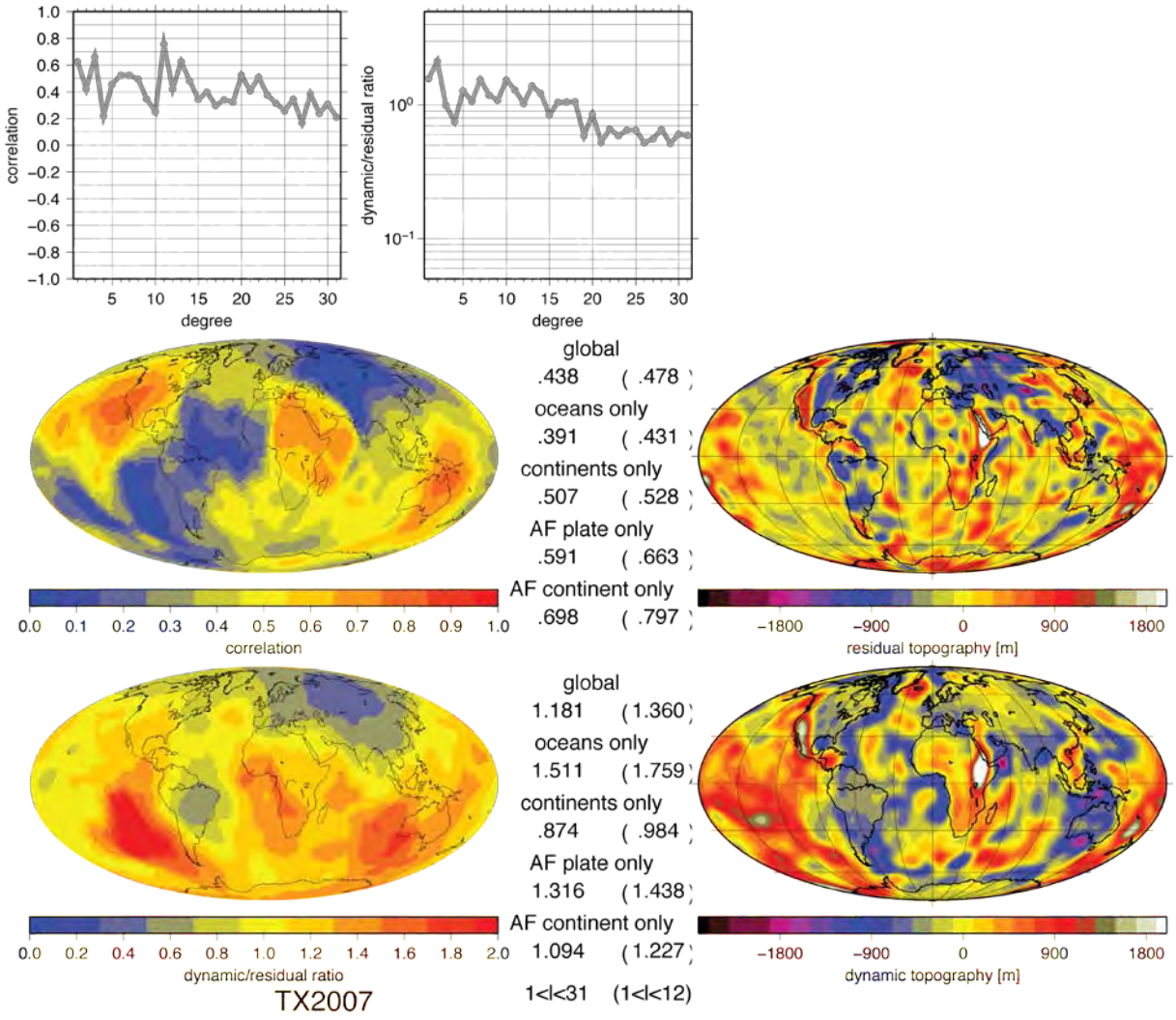

Figure 27: Results for the correlation and ratio between dynamic topography (computed based on tomography model TX2007) and residual topography. Cut-off S-wave anomaly 0.2%.

The following findings are typical for a large number of models:

- Correlations are higher for degrees 1-12 than for degrees 1-31. In the plots of correlation vs. degree, correlation tends to be high until about degree 15, and then drop

closer to zero (but typically still positive) for higher degrees. This indicates that the dynamic or residual topography models or both are probably more reliable for longer wavelengths.

- Correlation in continents tends to be higher than in oceans. Since crustal structure in the oceans is expected to be simpler than in the continents, hence the crustal correction for computing residual topography expected to be less error prone, we attribute this to generally better path coverage in the upper mantle (where density anomalies are most effective in causing dynamic topography) beneath continents
- Typically, three areas of high correlation are found: One centred on northeastern Africa, one centred on the western U.S., stretching into the northeastern Pacific, one around Australia/New Guinea. Areas where often low correlations are found are the southern Pacific, the central Atlantic and Russia.
- Correlation on the African plate tends to be higher than globally
- Correlation on the African continent tends to be even higher
- Dynamic to residual ratio tends to be somewhat (of the order of 50%) larger than 1 for "individual" tomography models for spherical harmonic degrees less than about 15, indicating that dynamic topography tends to be somewhat over-predicted (but see the finding below for the "mix" model). For larger degrees, the ratio goes gradually down with degree – typically to about 0.5-1 around degree 31. This could be either due to under-predicting dynamic topography (which would indicate a lack of resolution in tomography models) or over-predicting residual topography (most likely indicating shortcomings in the crustal correction). The considerations of geoid-topography ratio in section 5.8 rather indicate the latter (see there for details).
- Dynamic to residual ratio tends to be larger on continents than in the oceans. This difference is quite obviously due to lateral viscosity variations: Oceanic lithosphere is underlain by lower-viscosity asthenosphere, hence dynamic topography amplitude in the oceans is lower than predicted in our model without lateral viscosity variations, whereas it is higher in the continents. Hence our model tends to over-predict dynamic topography amplitude in the oceans and under-predict it in the continents.

P-wave models often don't image mid-ocean ridges well. When the effect of ocean floor cooling is subtracted, the predicted dynamic topography hence shows pronounced lows beneath ridges.

For comparison, *Fig. 28* shows the result when seismic velocity anomalies are converted to density anomalies everywhere including the lithosphere. As expected, this leads to a substantial over-prediction of dynamic topography amplitude. This is further illustrated in *Fig. 29*: A comparatively large variance reduction generally corresponds to high correlation and similar amplitudes (ratio close to 1): We hence obtain the best fit (in terms of variance reduction globally) for a cut-off at 0.2%.

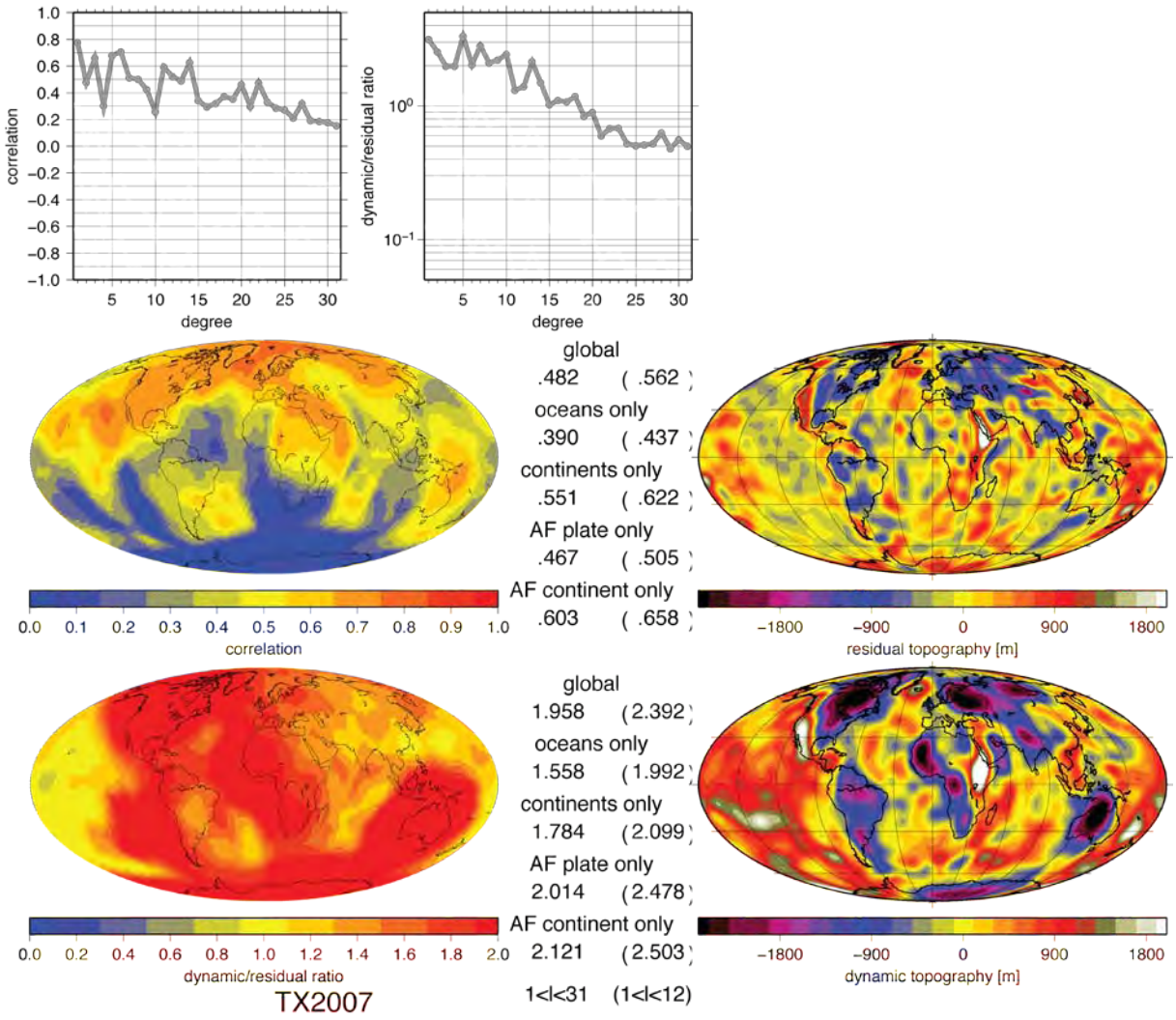

Figure 28: Results for the correlation and ratio between dynamic topography (computed based on tomography model TX2007) and residual topography. All S-wave speed anomalies (including those in the lithosphere) are converted to density anomalies.

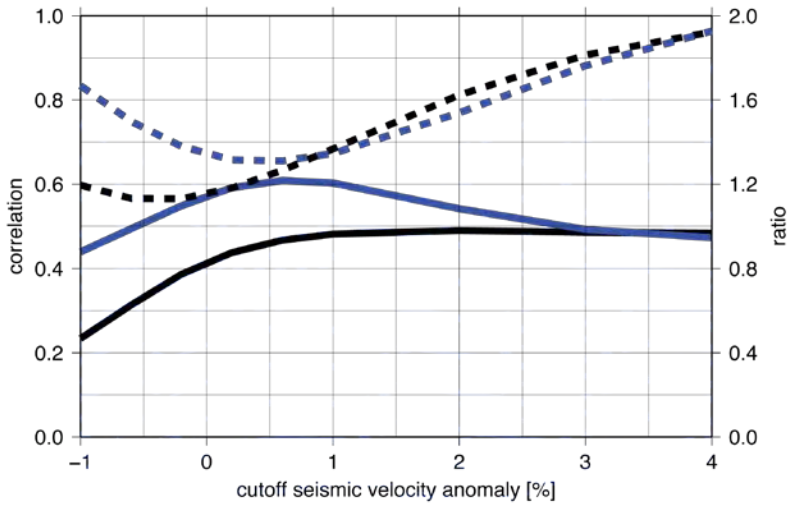

Figure 29: Correlation (continuous lines) and ratio (dashed lines) between dynamic topography (computed based on tomography model TX2007) and residual topography as a function of cut-off S-wave anomaly, both globally (black lines) and for the African plate (blue lines).

Subtraction of topography due to oceanic lithosphere cooling from both dynamic and residual topography is done, because otherwise a large part of the signal in both is due to ocean floor cooling. In this case (*Fig. 30*), correlation between dynamic and residual topography is high, and their amplitude is similar, indicating that seismic velocity anomalies in the shallow upper mantle beneath the oceans are largely due to temperature anomalies representing ocean floor cooling, and can explain age-dependent ocean floor topography quite well. However, we are here mainly interested in dynamic topography due to effects other than regular ocean floor cooling with age, and hence subtract this effect in both cases. This leaves the difference between dynamic and residual topography constant, however their correlation goes down. This indicates that dynamic topography due to effects other than ocean floor cooling with age is less well understood.

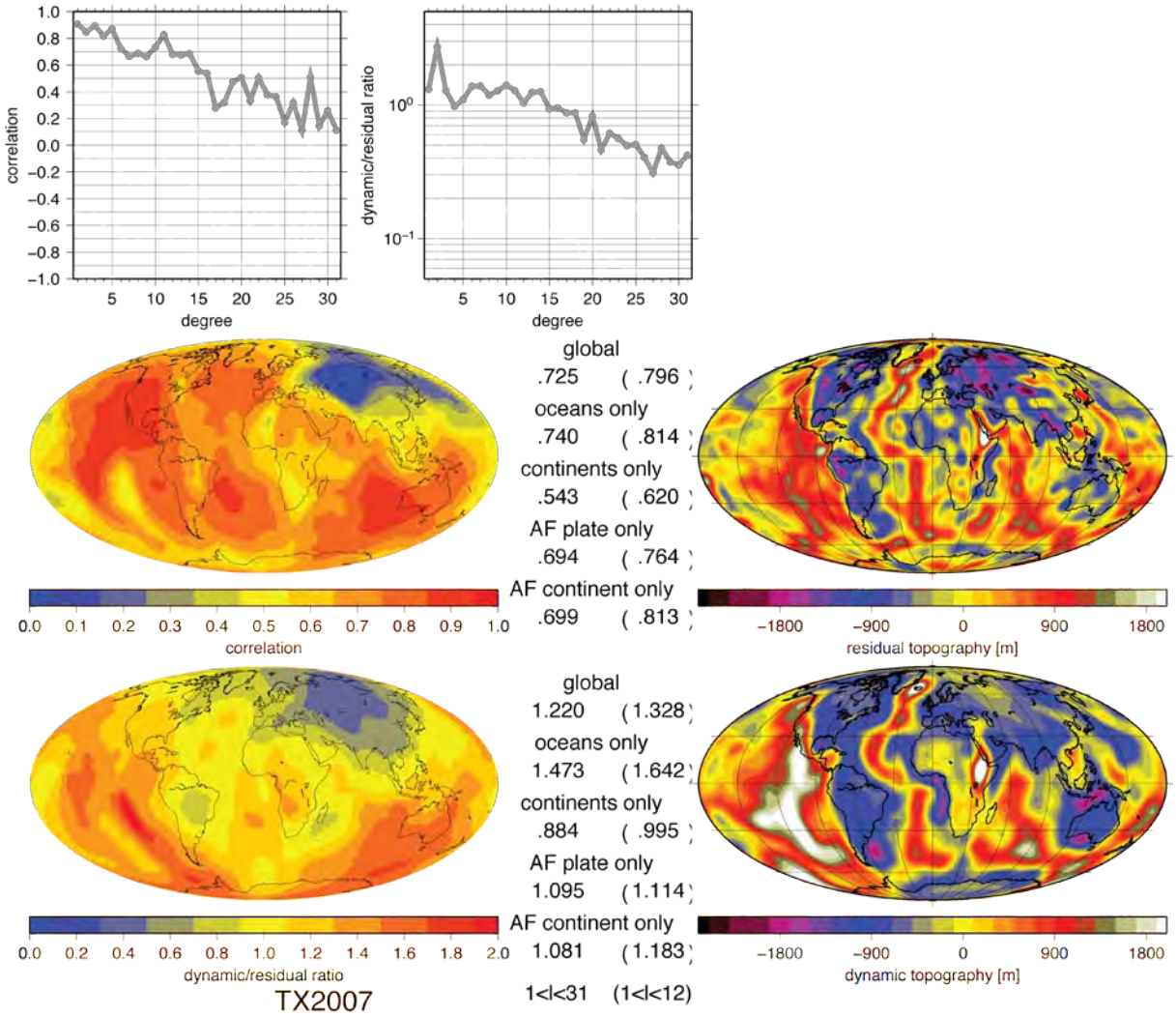

Figure 30: Results for the correlation and ratio between dynamic topography (computed based on tomography model TX2007) and residual topography, without subtraction of the effect of ocean floor cooling. Cut-off S-wave anomaly 0.2 %.

5.3 Using upper mantle tomography models

Dynamic topography is mostly caused by density anomalies close to the surface (see *Fig. 25*), it may therefore be advantageous to use tomography models constrained by surface waves to determine a density model. We use here 5 models from 4 groups, which are described in section 2.2, Appendix A and Tables 1 and 2. Results for all individual models are shown in Appendices B and C. Models KP08 (Priestley et al., 2008) and SF09 (Fishwick, 2010) are only given in a region around Africa and results are hence only shown there. Also, plotting correlation vs. degree is not meaningful if models are not given globally. This is hence not shown either. For models CU_STD1.0, CU_SRT1.0 (Shapiro and Ritzwoller, 2002) and LH08 (Lebedev and van der Hilst, 2008), correlation tends to be particularly good in the mid-degree range (about degrees 4-13). This is not surprising, because lower degrees are largely caused by density anomalies in the lower mantle (see *Fig. 25*), which is not included in these models. It hence suggests itself to combine one of these models in the uppermost mantle with a whole-mantle tomography model beneath. Various combinations were tried, and it was found that the combination of LH08 with TX2007 works well. We found the best result for the parameters (130 km, 0.5%) as in *Fig. 31*.

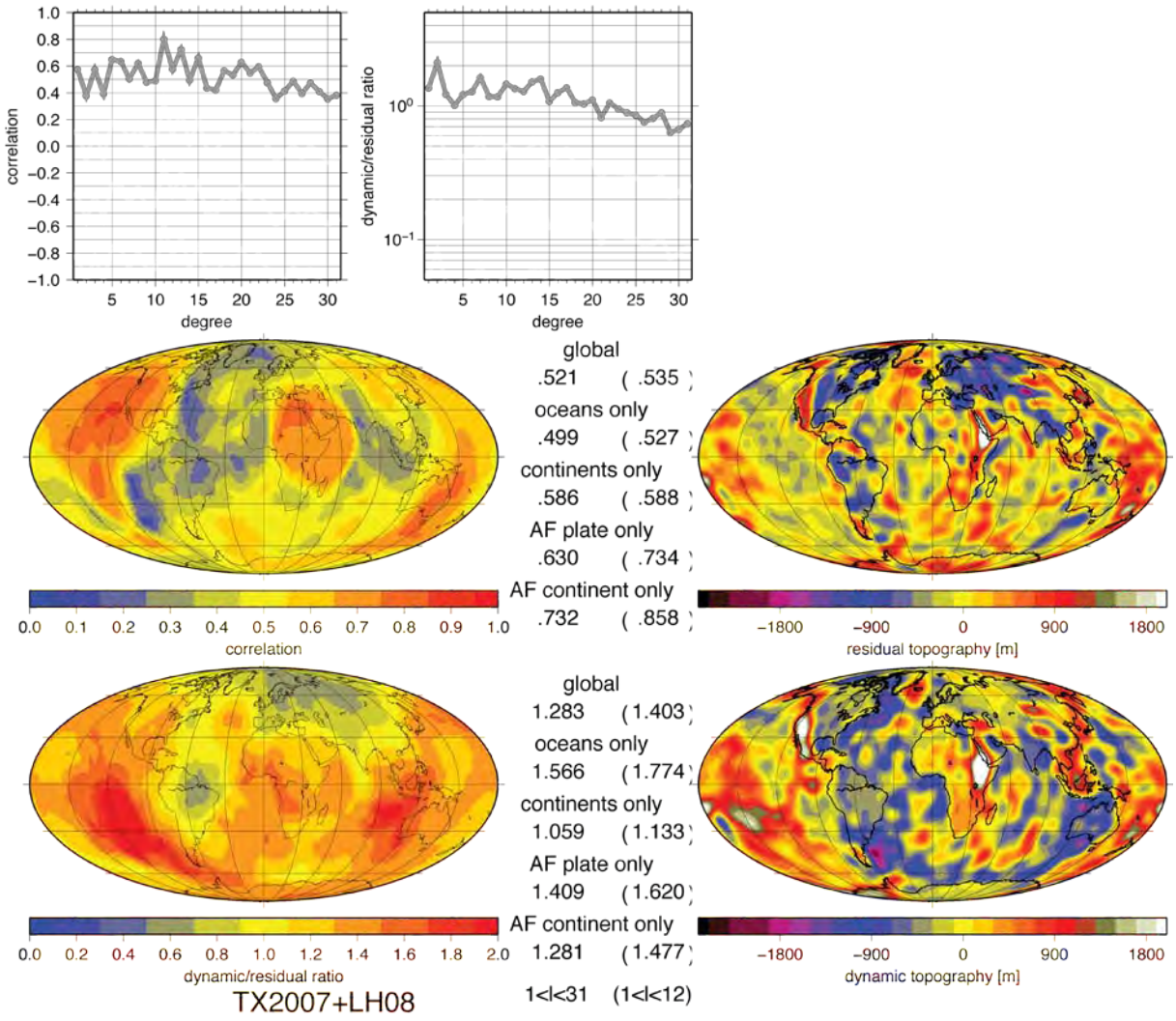

Figure 31: Results for the correlation and ratio between dynamic topography (computed based on tomography model TX2007 below depth 130 km and LH08 above) and residual topography. Cut-off S-wave anomaly 0.5%.

5.4 Using a mean model of whole mantle tomography

Typically mixing of two models averages out some features, hence the dynamic topography amplitude of the mixed model tends to be somewhat lower than for individual models. The effect of mixing is illustrated in *Fig. 32*. The mixture gives a lower amplitude and higher correlation than the individual models. In this case, the best fit (in terms of variance reduction) occurs for a fraction 0.6.

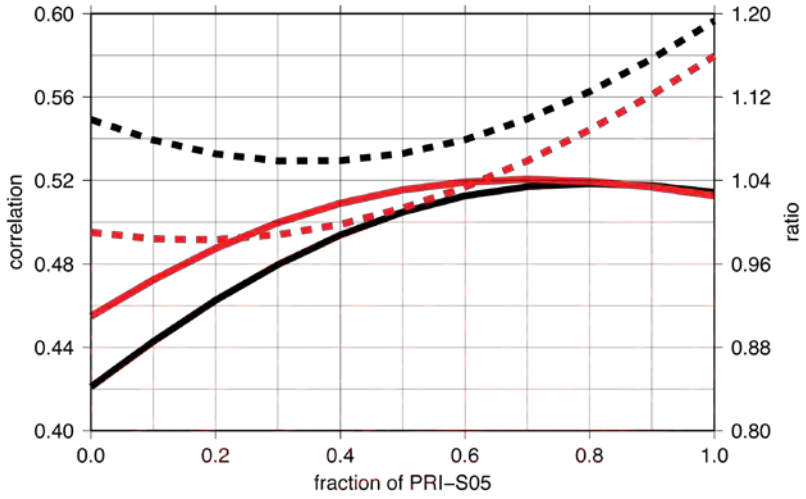

Figure 32: Correlation (continuous lines) and ratio (dashed lines) between dynamic topography computed based on a mixture of tomography models PRI-S05 and PRI-P05 and residual topography as a function of the fraction of PRI-S05 contained in the mixture, both globally (black lines) and for the African plate (red lines).

While the dynamic topography amplitude of individual models tends to be somewhat too high, the rms amplitude for model MIX-A (*Fig. 33*) is almost identical with the residual topography rms amplitude. Only for spherical harmonic degree two, dynamic topography is over-predicted by a factor of more than 2. To ascertain that this is not due to the fact that the Large Low Shear wave Velocity Provinces (LLSVPs) of the lowermost mantle have a negative chemical buoyancy, we performed additional calculations, where we have assigned a large positive density anomaly to LLSVPs but – due to the rather small topography kernels in the lowermost mantle – results change only very little.

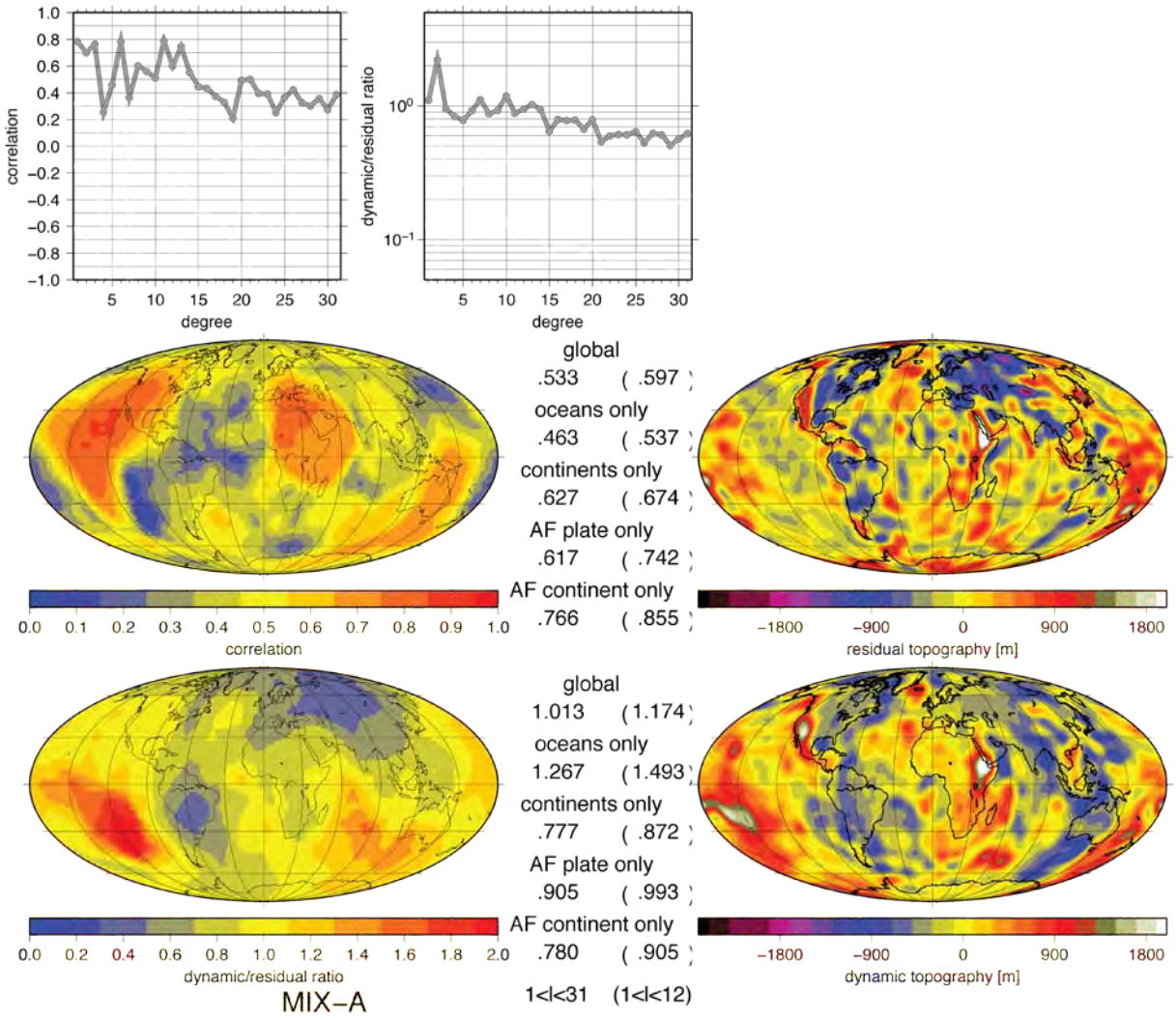

Figure 33: Results for the correlation and ratio between dynamic topography (computed based on the mean tomography model MIX-A) and residual topography. Cut-off S-wave anomaly 0.3%.

5.5 Alternative mantle lithosphere models

Besides the lithosphere models that are derived here directly from the tomography models used, as described in section 5.1, we use here also a number of other models to infer lithosphere thickness variations in continents (see section 3 and *Fig. 24*). For simplicity, we use the same averaged tomography model as before. Since the mixture for model MIX-A was determined by optimizing the fit to topography, a slightly worse fit with another lithosphere model and without changing the mixture (such as found for the Conrad lithosphere model) does not imply that this other lithosphere model is worse. Obviously, we can expect to obtain an improved fit if we re-determine the optimum mix for each lithosphere model used.

The model of Conrad and Lithgow-Bertelloni (2006) (*Figs. 24a, 34* is essentially derived in a similar way, based on a tomography model. Not surprisingly, results stay very similar. The thermal model TC1_z1300.1d of Artemieva (2006) (*Figs. 24b, 35*) gives a better fit in some regions, notably around Greenland and Denmark and in Russia. Elsewhere, results remain mostly similar, but on the African plate and African continent, the fit deteriorates. The model of Rychert et al. (2010) (*Fig. 24c*), based partly on Rychert and Shearer (2009), is a global compilation of seismic observations of what is interpreted as the lithosphere-asthenosphere boundary. Using this model in combination with the model of Artemieva gives

further improvements in many of those regions where seismic measurements exist (*Fig. S18*). The Africa model of Crosby et al. (2010; pers. comm. Fishwick) (*Figs. 24d, 36*) is based on tomography model SF09. The Africa model of Pasyanos and Nyblade (2007; lithosphere thickness model pers. comm.) (*Figs. 24e, 37*) is also based on a regional tomography model. In *Figs. 36* and *37*, the model of Conrad and Lithgow-Bertelloni (2006) is used for the rest of the Earth. For all these lithosphere models based on tomography, results remain rather similar.

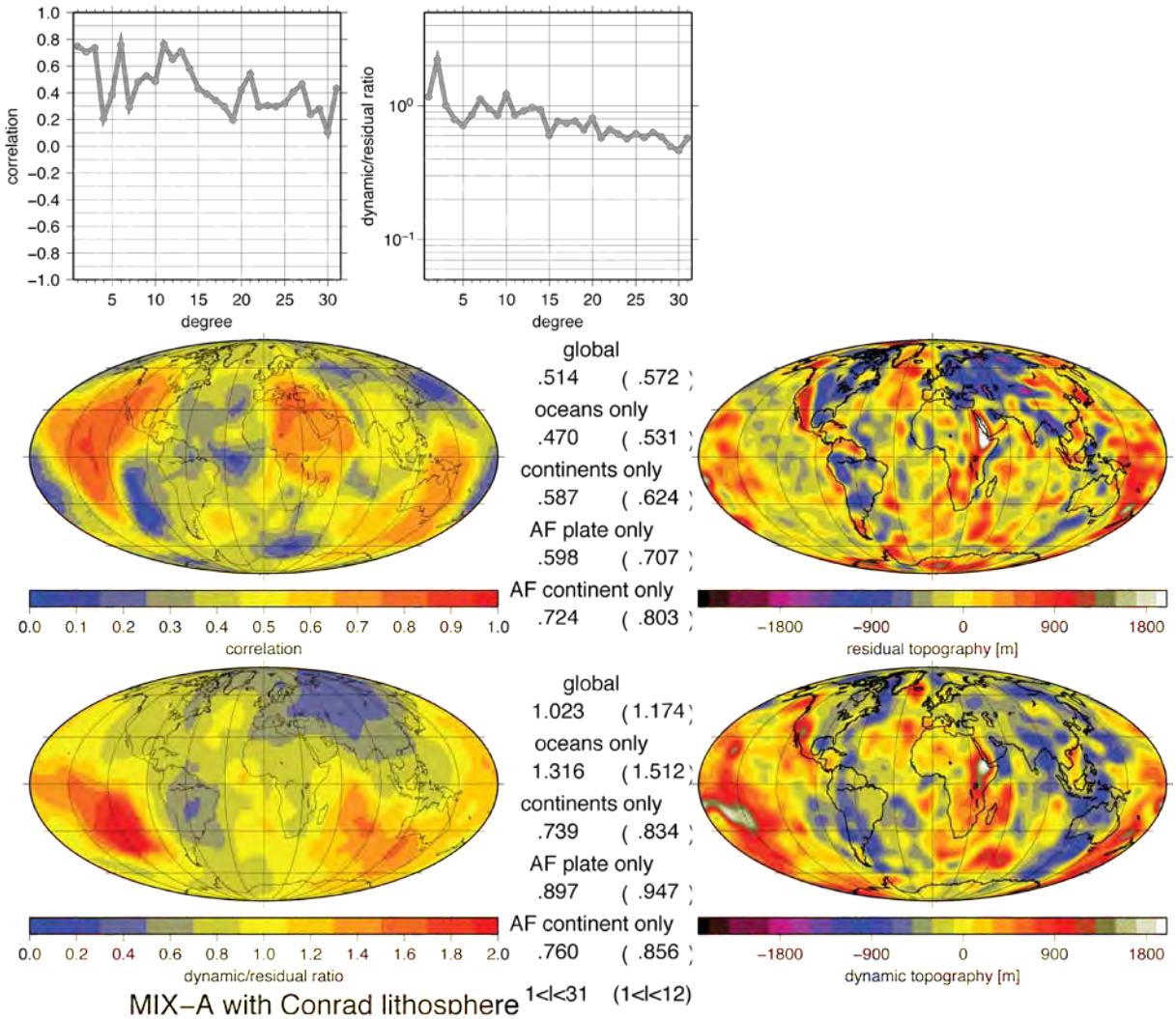

Figure 34: Results for the correlation and ratio between dynamic topography (computed based on the mean tomography model MIX-A) and residual topography. Lithosphere model of Conrad and Lithgow-Bertelloni (2006) is used; S-wave anomaly is replaced by -0.2% within lithosphere.

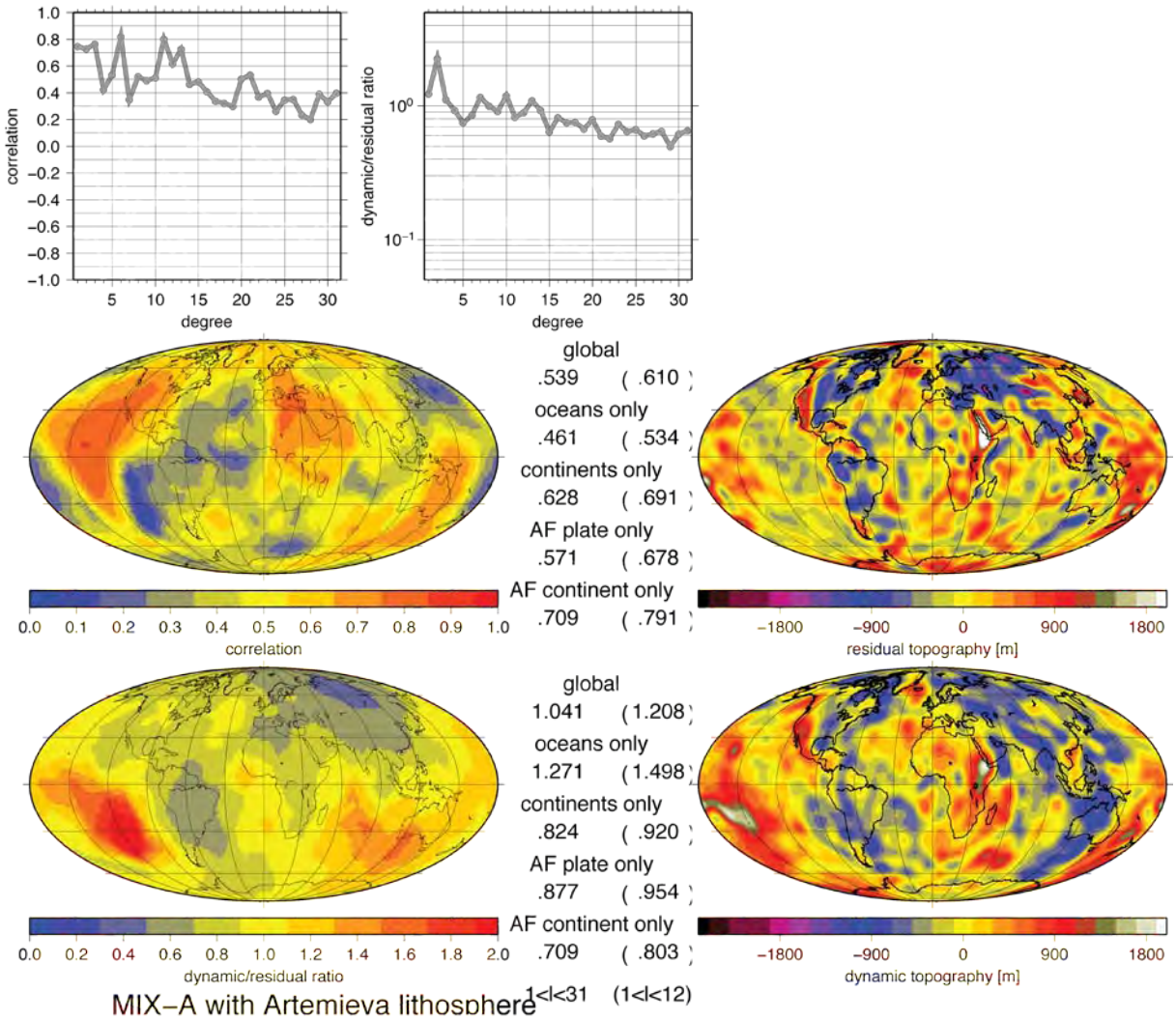

Figure 35: Results for the correlation and ratio between dynamic topography (computed based on the mean tomography model MIX-A) and residual topography. Lithosphere model of Artemieva (2006) is used; S-wave anomaly is replaced by -0.6% within lithosphere.

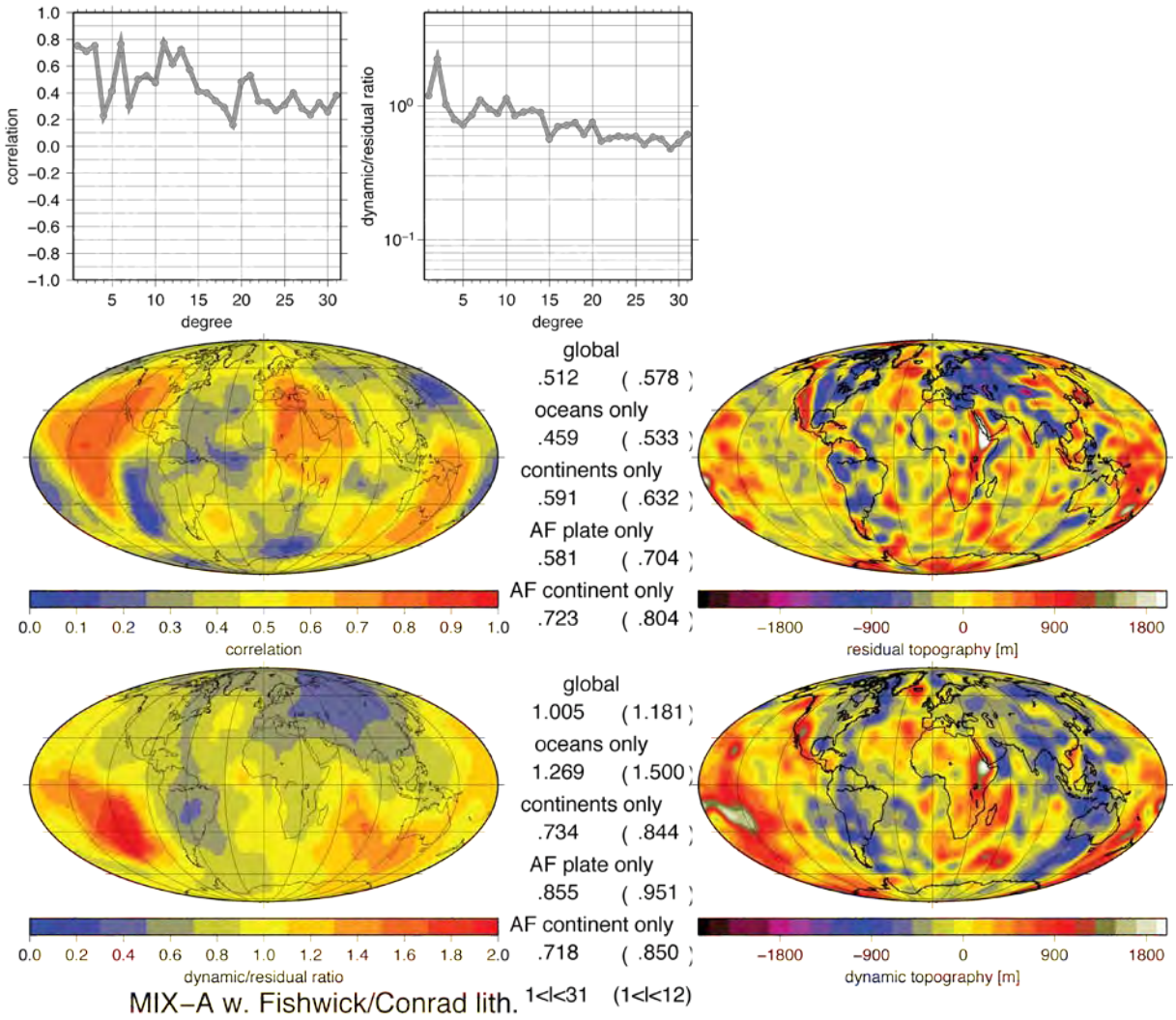

Figure 36: Results for the correlation and ratio between dynamic topography (computed based on the mean tomography model MIX-A) and residual topography. Lithosphere model of Crosby et al. (2010), based on tomography model SF09 (Fishwick, 2010) is used where it is given (40°S - 40°N and 30°W - 60°E), model of Conrad and Lithgow-Bertelloni (2006) is used elsewhere; S-wave anomaly is replaced by -0.1% within lithosphere.

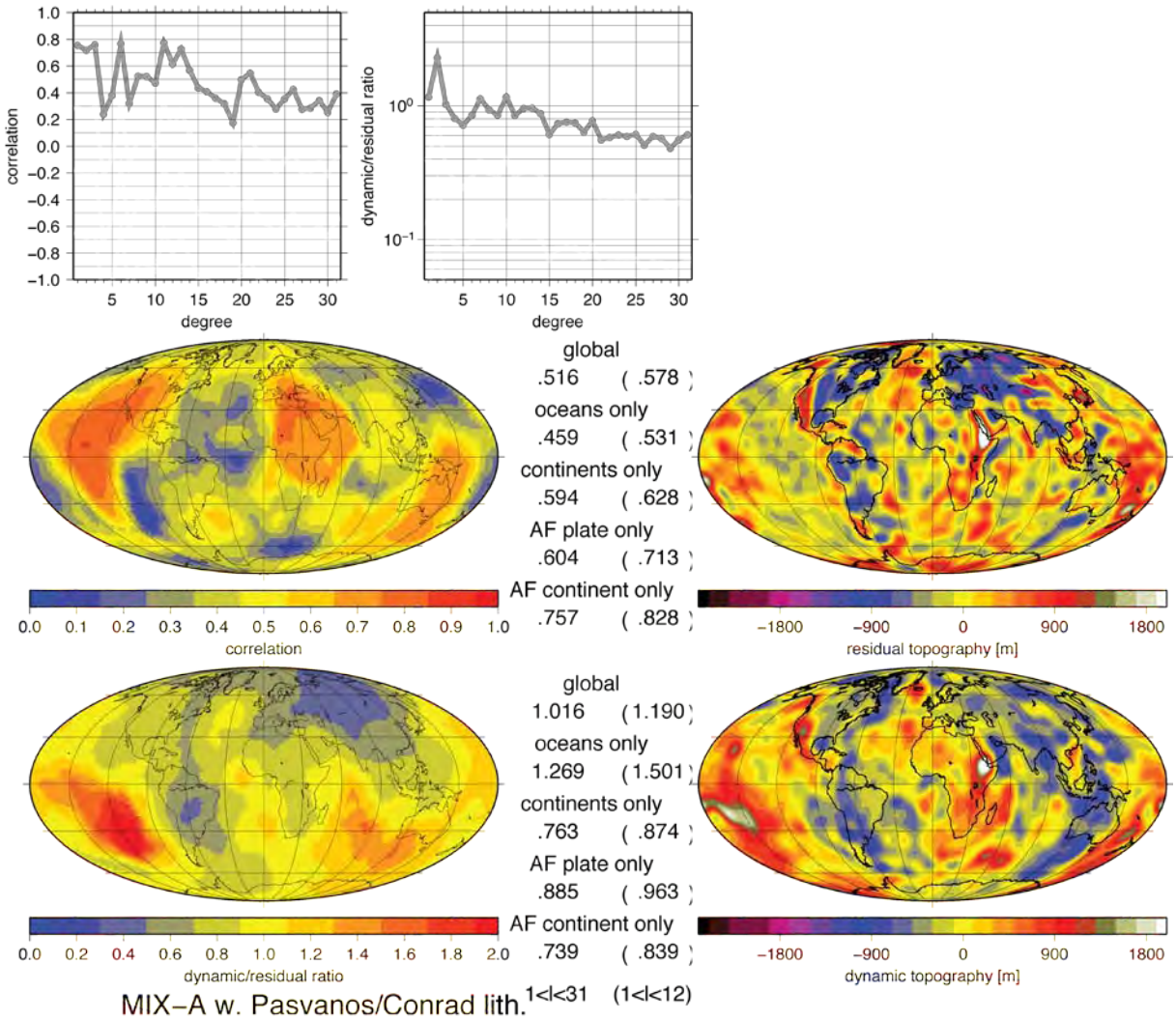

Figure 37: Results for the correlation and ratio between dynamic topography (computed based on the mean tomography model MIX-A) and residual topography. Lithosphere model of Pasyanos and Nyblade (2007) is used where it is given (40°S - 50°N and 20°W - 60°E), model of Conrad and Lithgow-Bertelloni (2006) is used elsewhere; S-wave anomaly is replaced by -0.1% within lithosphere.

5.6 Alternative crustal models

Using a crustal model that is derived from gravity inversion (S. Werner, pers. comm.) in the region of Africa gives a worse fit (*Fig. S19*). A possible reason for that is the generally high correlation (about 0.7) above degree 12 between gravity and topography. Hence, when deriving crustal thickness from gravity, we expect that – except for the lowest degrees up to 12 – most topography – regardless whether it is dynamic or isostatic – is mapped into crustal thickness variations and hence interpreted as isostatic. The resulting residual topography has therefore rather low amplitude and is comparatively poorly correlated with dynamic topography.

It would also be useful to implement new results on crustal thickness and structure that goes beyond CRUST2.0 where it is available. We are not aware of any suitable model for Africa, but as an example, implement here the European model EuCRUST-07 of Tesauro et al. (2008). Results (*Fig. S20*) remain similar with somewhat worse correlations.

5.7 Dependence of results on asthenosphere viscosity

Fig. 35 shows variations in dynamic/residual ratio between about 0.4 near the centre of the Eurasian plate and about 2.0 above the East Pacific rise. A likely explanation for these variations are lateral viscosity variations in the asthenosphere. To quantify this, we show in *Fig. 38* dynamic topography amplitude as a function of asthenosphere viscosity and the boundary condition (zero horizontal motion vs. stress free). The first boundary condition may be more appropriate for the interior of large plates, whereas the second one may be more appropriate near plate boundaries, especially ridges. To compensate for the low dynamic-residual ratio in Asia, dynamic topography would need to increase by about a factor 2. *Fig. 38* shows that such a high ratio is not reached among the models plotted. It is not even quite reached with a more extreme model (zero horizontal surface motion; 10^{24} Pas above 340 km and 10^{21} Pas in the remaining upper mantle and transition zone). On the other hand, to compensate for the high ratio beneath the East Pacific Rise not even an asthenosphere viscosity as low as 10^{17} Pas would be sufficient. Overall the results point towards substantial lateral viscosity variations in the asthenosphere. On the African plate, though, the ratio varies typically between around 1 near the surrounding ridges and 0.8 in the plate interior. This can be adequately explained as corresponding to the different boundary conditions (near ridges more close to "free slip", in the plate interior more like "rigid lid" i.e., zero horizontal motion).

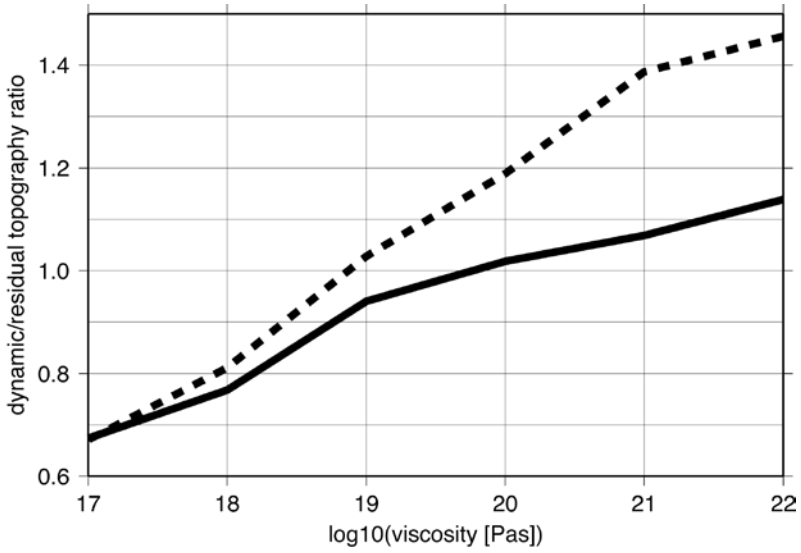

Figure 38: Dynamic topography amplitude (normalized to residual topography) as a function of viscosity in the asthenosphere (depth 100-220 km) for an upper boundary condition with zero horizontal velocity (dashed lines) and stress-free (with lithosphere viscosity $\approx 2 \cdot 10^{22}$ Pas; continuous line).

5.8 Expected versus modelled geoid-topography ratio and correlation

We now consider the observed versus modelled geoid-topography ratio as an indicator of whether the discrepancy between dynamic and residual topography is due to errors in dynamic or residual topography. The model predictions use a slightly different viscosity structure (Fig. 8 of Steinberger et al., 2010). The model is derived in detail by Steinberger et al. (2010) and Steinberger and Holme (2002). Changing the results described in this paper until here to this viscosity structure would lead to only minor changes.

Fig. 39 shows that between degrees 15 and 31 the ratio of residual geoid and topography goes down by about a factor 2 whereas the ratio expected from a model prediction goes down by a much smaller amount. On the other hand, the observed geoid power matches the model prediction quite well over the entire degree range (see top left panel of Fig. 9 by Steinberger et al., 2010). If the model prediction is correct, this would imply that residual topography is gradually more over-predicted for degrees increasing from 15 to 31. About the same amount

of residual topography over-prediction would also compensate for the discrepancy between dynamic and residual topography amplitude. We hence consider an increasing over-prediction of residual topography for degrees increasing from 15 to 31 more likely than an increasing under-prediction of dynamic topography. Such an over-prediction can be caused by errors in the crustal model used, and thus an incorrect computation of isostatic topography.

Another effect that we did not consider here is the elasticity of the lithosphere. We always assume isostatic compensation and considering elasticity would cause gradually decreased dynamic topography for higher degrees and would therefore even worsen the misfit between dynamic and residual amplitude. Such an even stronger misfit could indicate that over-damping of tomography models at higher degrees (and hence a too small dynamic topography prediction) could also play a role in causing the misfit.

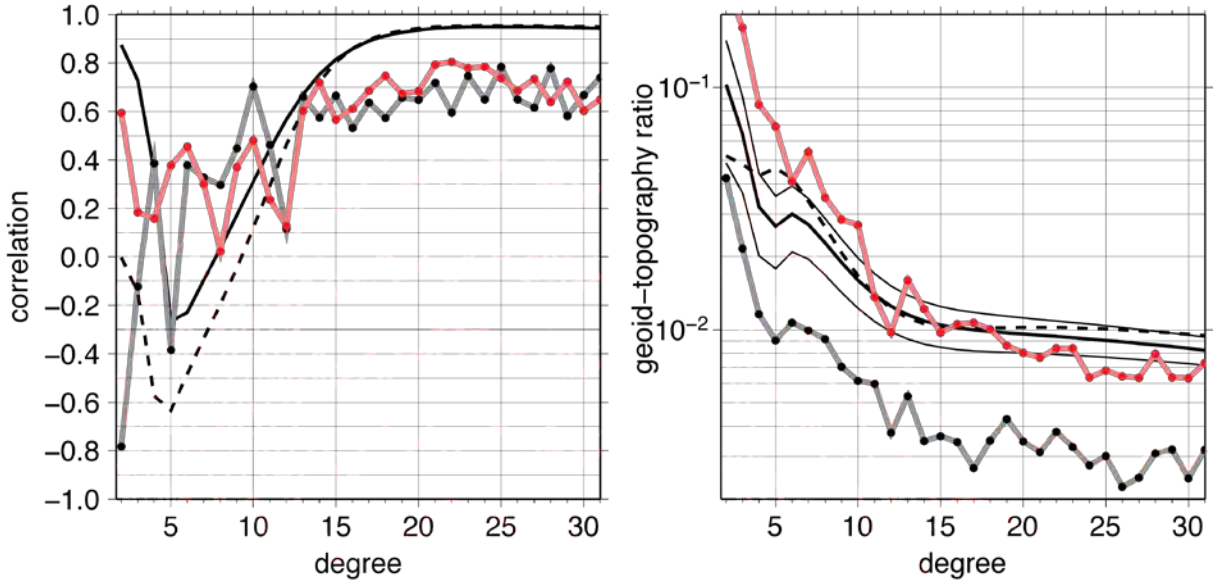

Figure 39: Geoid-topography correlation (left) and ratio (right). Continuous black lines are expected for no-slip (corresponding to bottom case in *Fig. 25*), with accompanying thin lines in the right panel indicating expected variation (1-σ standard deviation), dashed lines are for free-slip (corresponding to top case in *Fig. 25*). Grey lines with black dots are based on observed geoid and topography (which has, however, been corrected for water coverage, i.e., we use the "rock equivalent topography" of Wieczorek, 2007), pink line with red dots for residual geoid and topography.

Fig. 39 also shows that in the degree range ≈ 16 to 31 the expected geoid-topography ratio is about 1.4 % and their expected correlation is high. In *Fig. 40* we hence look regionally where these expectations are best met: We find high geoid-topography correlations in two regions where we also typically found high correlations of dynamic and residual topography. Again, this coincidence indicates that the lower correlations in other regions are more likely due to errors in residual topography rather than dynamic topography. A possible exception is Antarctica and the surrounding southern seas: Here geoid-to residual topography correlation is high, but the dynamic-to-residual topography correlation is not particularly high. Thus in these regions, the discrepancy may be to a larger degree due to errors in dynamic topography. This result is not surprising either, as these are the least well covered regions in mantle tomography models. The geoid-topography ratio most closely matches the expected value of about 1.4 % in a region centered on central Europe.

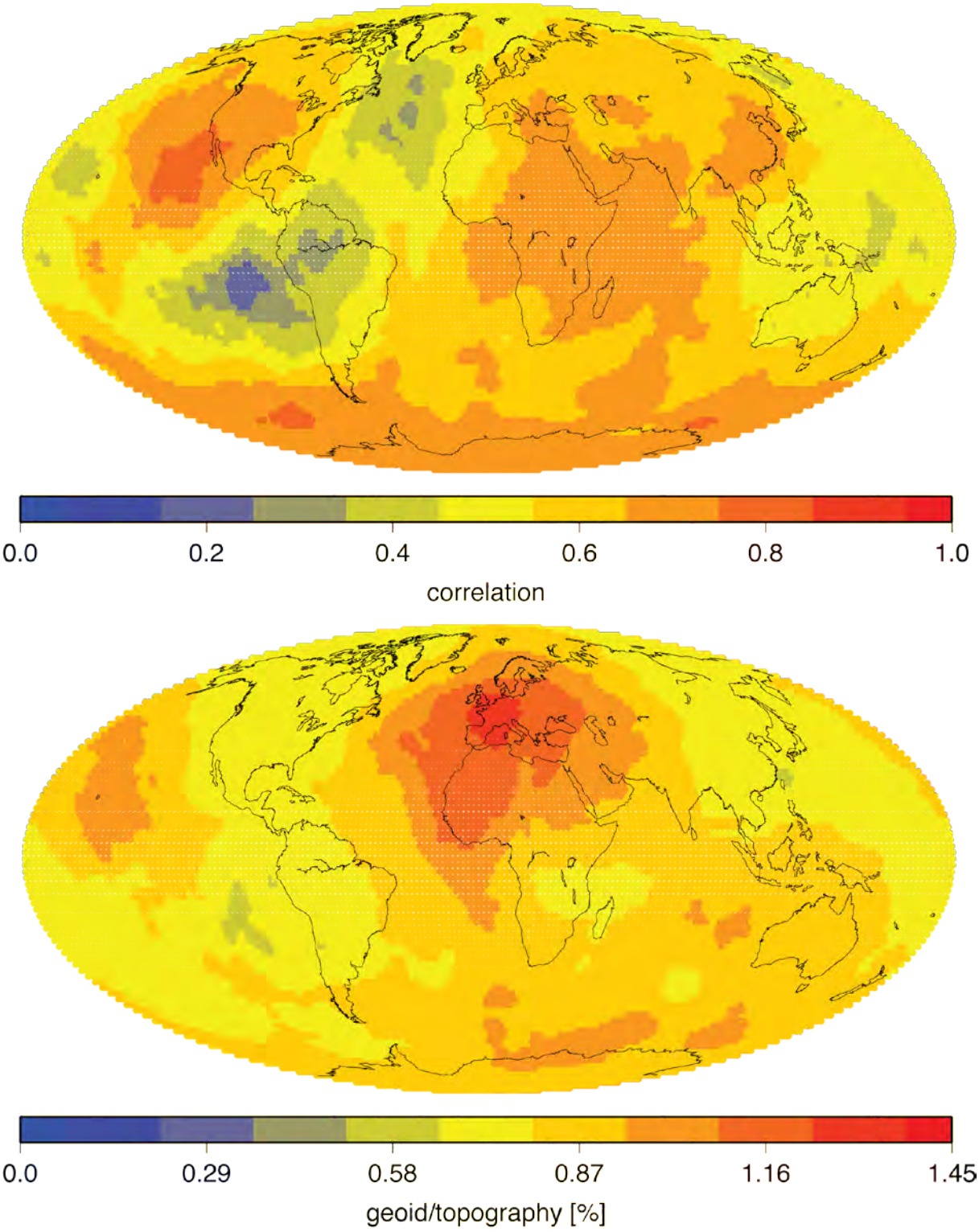

Figure 40: Correlation (above) and ratio (below) of geoid and residual topography. They are computed for each point in a spherical cap of 30 degrees around that point and in the spherical harmonic degree range 16-31.

6. PAST DYNAMIC TOPOGRAPHY

6.1 Past dynamic topography in the mantle reference frame

Density anomalies are backward-advected in the flow field. In contrast to the dynamic topography computations themselves we use here prescribed reconstructions (Torsvik et al., 2010). This boundary condition is most appropriate to compute the flow field itself, but it can lead to artifacts in the computed surface stresses (hence inferred dynamic topography) if the prescribed motion of the plates (sometimes called the "hand of god" approach) is not consistent with the forces acting on the plates. For computing dynamic topography, a free-slip boundary condition is therefore more appropriate.

A problem with the backward-advection approach is that it neglects the effect of diffusion. Hot anomalies close to the surface, which are most effective at causing positive dynamic topography, are backward-advected to the lower mantle. Cold anomalies close to the surface, which are most effective at causing positive dynamic topography, are flattened out near the surface due to backward advection. As a consequence, the computed amplitude of dynamic topography becomes smaller further back in time (*Fig. 41*). Running diffusion backward in time is unstable and therefore not a suitable remedy. Here we try as a partial remedy a "modified backward advection" approach. Different from the "pure backward advection" we introduce a diffusion term in radial direction. Backward in time, heat is added where the uppermost layer is hotter than average, and heat is removed where it is colder. When running the computation with this added diffusion term backward in time, the decay of amplitude is reduced. However, further back in time the amplitudes increase again and instabilities are developing. We hence consider in the following the "pure backward advection" shown in *Fig. 42*.

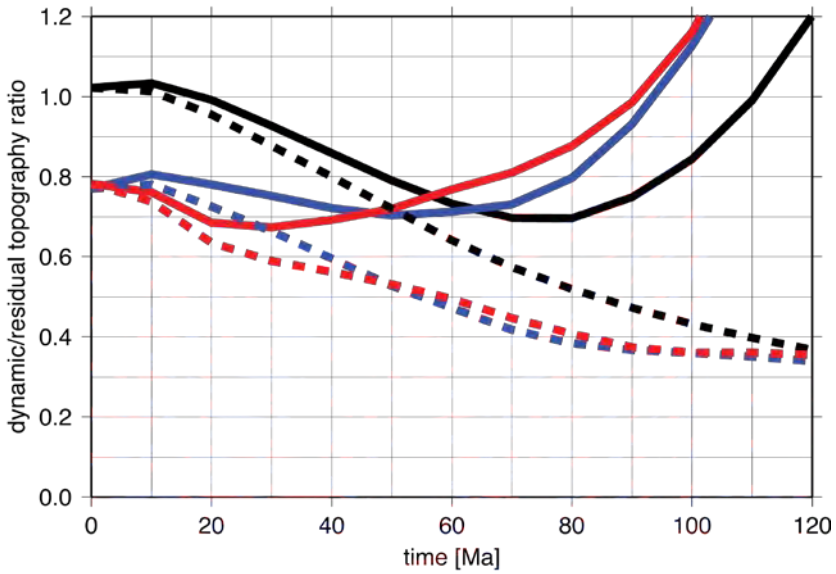

Figure 41: Root-mean-square dynamic topography (normalized to present-day residual topography) as a function of time globally (black lines), for the area of the African plate in present-day coordinates only (blue lines) and for the area of the African continent in present-day coordinates only (red lines), computed with pure backward advection (dashed lines) and modified backward advection (continuous lines).

Fig. 43 illustrates the result of backward-advection along a cross-section through South and East Africa which, according to our analysis in section 2, shows some of the most reliable features imaged by tomography beneath Africa. It shows the anomaly that is now beneath East Africa further down in the mantle further back in time. This feature is probably an artifact of the backward advection, since volcanism has begun in East Africa about 30 Myr ago (Hofmann et al., 1997). It also shows the lower mantle anomaly beneath South Africa at larger depth further back in time. This result is probably more realistic (Conrad and Gurnis,

2003) since diffusion plays less of a role in the mid-mantle -- as opposed to the thermal boundary layers.

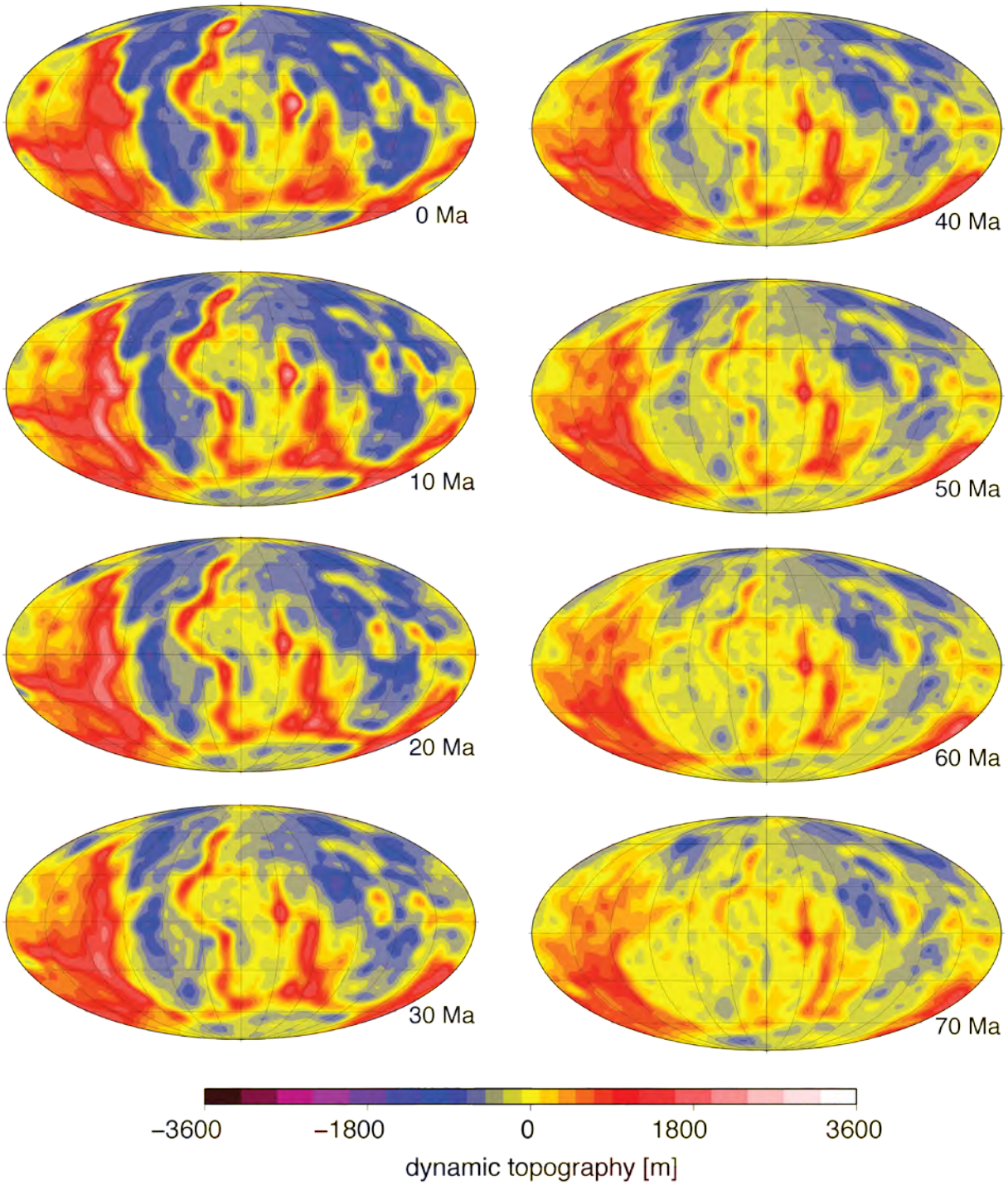

Figure 42: Past dynamic topography in mantle frame.

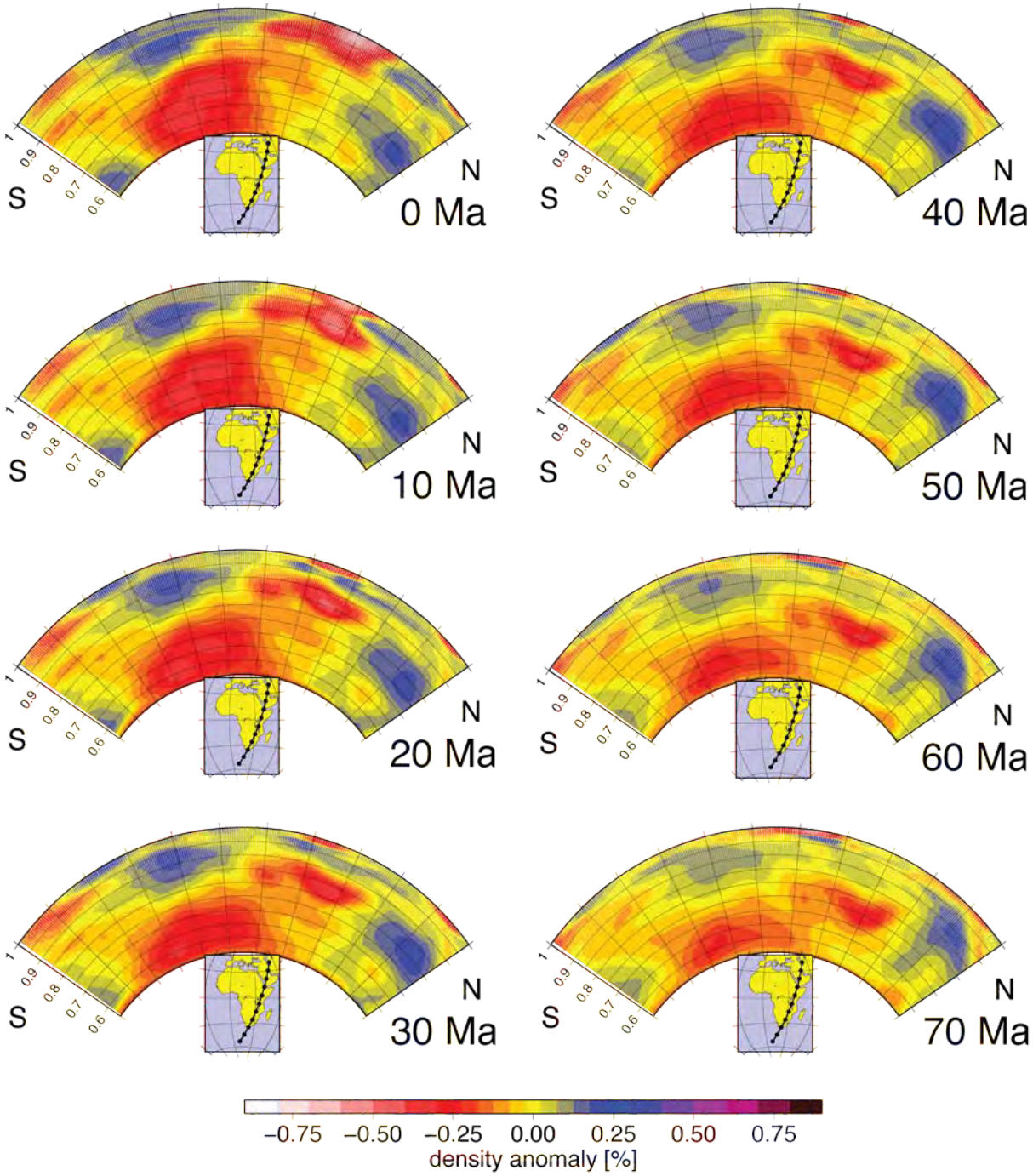

Figure 43: Cross sections along a line fixed in the mantle frame. Maps show Africa in present-day coordinates (and not at the location corresponding to the respective time.

6.2 Past dynamic topography in the reference frame of the African plate

Combining the results of backward-advection in section 6.1 with models of plate motions, we can compute dynamic topography changes in a reference frame moving with the African plate (*Fig. 44*). For comparison with observations of uplift or subsidence, topography versus time at individual points moving with the plate is shown in *Fig. 45*. An example for density anomalies along a cross-section moving with the African plate is given in *Fig. 46*. Given the problems mentioned in section 6.1, these results should be mostly seen as examples illustrating the method, and not be over-interpreted.

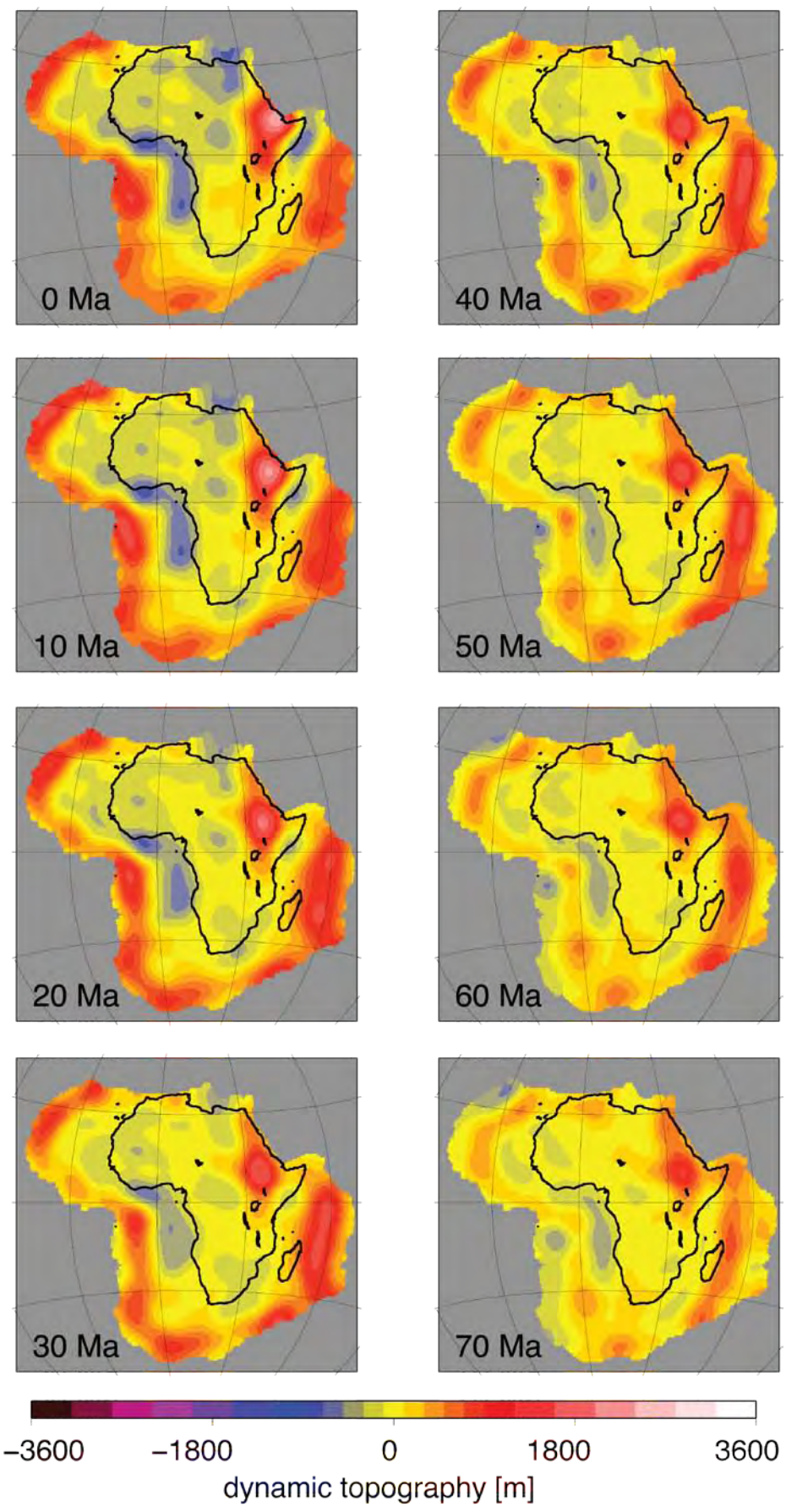

Figure 44: Past dynamic topography relative to Africa kept fixed shown for the present-day African plate. Note that the African plate was smaller in the past. The past plate boundaries approximately follow the red areas that outline the past locations of active mid-ocean ridges.

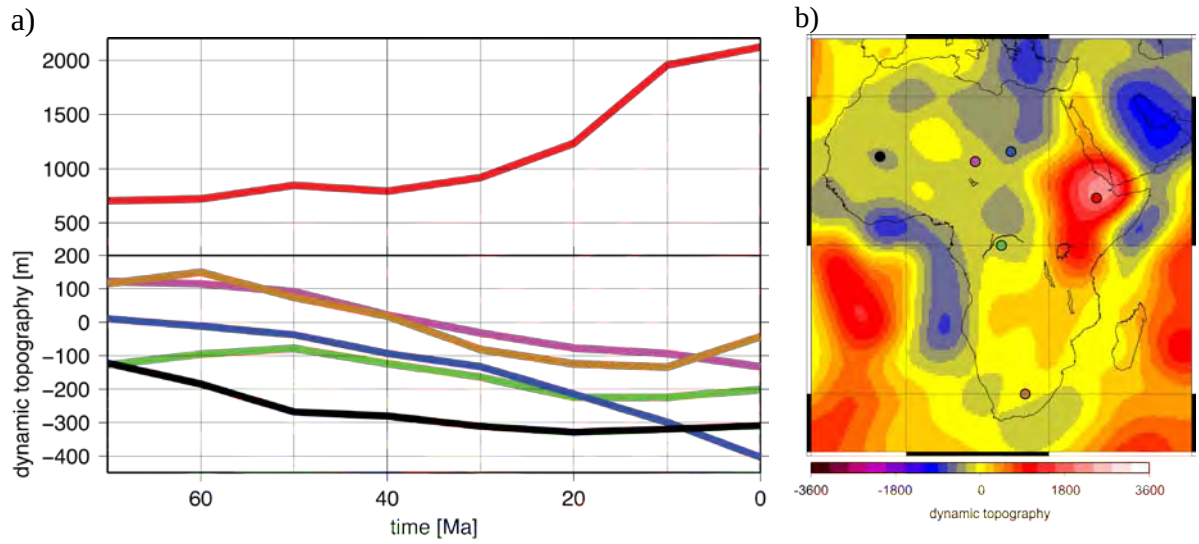

Figure 45: a) Past dynamic topography versus time at 6 points moving with the African plate. Red line: 40° E, 10° N (Afar). Green line 20° E, 0° N (Congo Basin). Brown line: 25° E, 30° S (South Africa). Blue line: 22° E, 19.5° N (Kufrah Basin). Violet line: 14.5° E, 17.5° N (Chad Basin). Black line: 5.5° W, 18.5° N (Taoudeni Basin). Note the different scale for the red line. b) Position of the points.

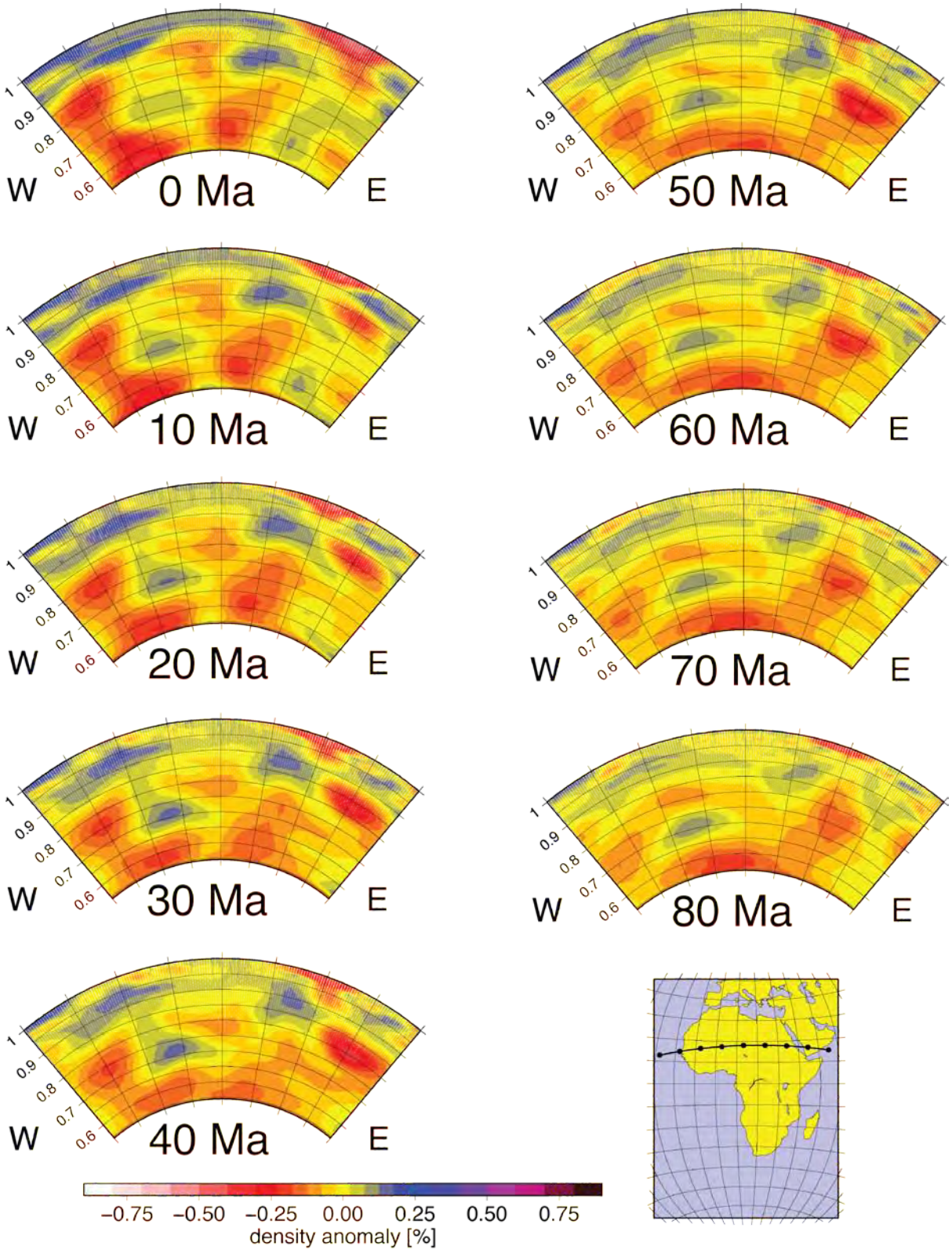

Figure 46: Cross sections along a line moving with the African plate. It passes approximately through the Kufrah basin (≈ 32 degrees clockwise along cross section), Chad basin (≈ 39 degrees) and Taoudeni basin (≈ 57 degrees).

7. MANTLE-LITHOSPHERE INTERACTION

Summarised very briefly, changes in continental surface topography can be caused by lithosphere deformation, mantle flow, and erosion and/or sedimentation. In the previous sections we have derived the contribution of mantle flow to African surface topography. One open question is what the role of the lithosphere could be in either modulating this dynamic topography through lithospheric flexure or perhaps even adding to it through active deformation processes. To examine the role of the lithosphere, we coupled mantle flow and lithosphere deformation models in a simple manner. We apply the velocities and pressure from the mantle models at 100 km depth to the lithosphere models (*Fig. 47*). We use here the SG06 tomography model for the mantle flow calculations (*Fig. 14*, sections 5.1 and 5.2). Our approach has the following limitations: 1) Back-ward advection of density anomalies in the mantle flow models is reliable until approximately 70 Ma, perhaps 100 Ma, as the approach neglects diffusion. This limits how far back in time we can compute topography changes; 2) The temperatures in our lithosphere and mantle models are advected only (i.e., no thermal conduction); 3) Dynamic feedback effects between the lithosphere and mantle models are not considered. However, the models do give us a first-order impression of the potential influence that the lithosphere could have on dynamic topography for African regions. With our coupled models, we specifically address two aspects of the mantle flow models: the surface condition and the lithosphere rheology. The mantle flow models have a so-called free-slip upper surface, meaning that vertical movements of the Earth's surface cannot occur. Topography in the mantle models is calculated from vertical stresses at the surface. The lithosphere is represented by a highly viscous layer. By coupling our models, we introduce a free surface and can evaluate the role of the surface boundary condition. We here examine the role of including a lithosphere with a temperature- and pressure-dependent viscous -plastic rheology.

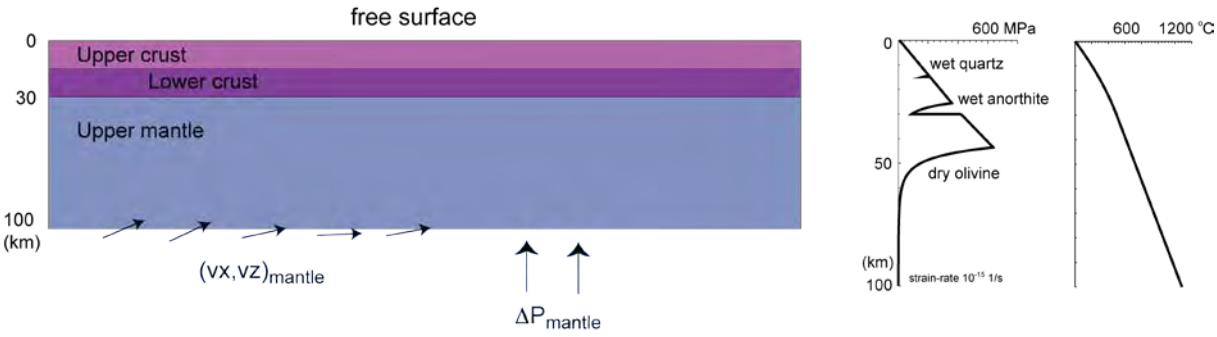

Fig. 47: Schematic model setup for models that couple the effects of mantle flow to thermomechanical lithosphere deformation models. The domain length is variable and always extends 100 km on each side beyond the profile length shown in subsequent figures. The material behaviour is viscous-plastic, whereby the deformation mechanism is selected which results in the minimum effective deviatoric stress. Frictional materials have angle of internal friction 30º softening to 15º and cohesion 10 MPa. Creep laws from Gleason and Tullis (1995), Rybacki and Dresen (2000) and Hirth and Kohlstedt (1996). The initial effective stress and temperature profiles are shown at the right side. The lithosphere models are computed with SULEC (Buiter and Ellis, in prep; Ellis and Buiter, in prep).

We focus on the Taoudeni, Kufrah and Congo sedimentary basins (*Fig. 48*). These basins are so-called intracratonic basins which record slow sedimentary processes since their formation in the (Pre)Cambrian. The absence of large-scale normal faults indicates that they are not typical rift basins and no conclusive formation mechanism has so far been identified for them. The Congo basin (see also section 1) contains up to 9 km of unconformity-bounded sedimentary layers of Precambrian to Cenozoic age. The uppermost 1-2 km (Mesozoic to Cenozoic) have been deposited during a time when the Congo craton was tectonically stable.

The large-scale Taoudeni Basin lies on the thick lithosphere of the West African Craton and contains up to around 5 km of Pre-Cambrian to Cretaceous sediments. In the time-span considered in our models (Late Cretaceous to recent), only minor sedimentation occurred. The oldest sedimentary strata in the Kufrah Basin are Cambro-Ordivican. The basin is filled with up to 3-4 km of sediments and lies on relatively thin lithosphere. Its western edge is close to the (Late Miocene - Late Quaternary) Tibesti volcanic centre.

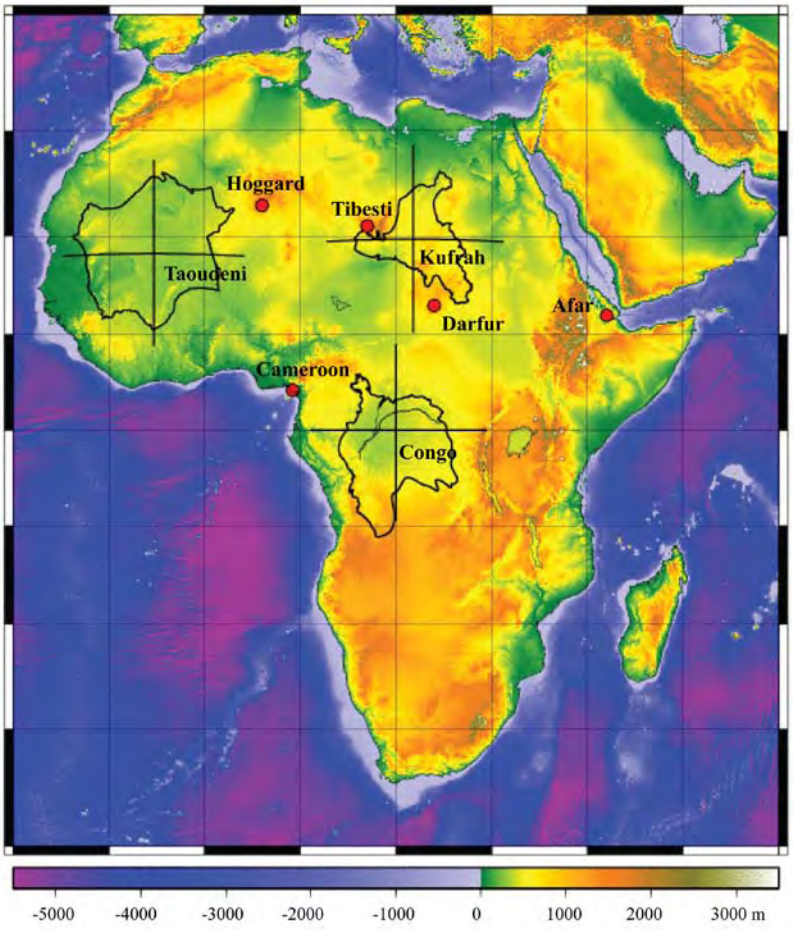

Fig. 48: Locations of the North-South and West-East sections through the Kufrah, Congo and Taoudeni sedimentary basins that are used in coupling the 2D lithosphere models to the mantle flow models.

We first use a linear viscous only lithosphere, which allows us to evaluate the effects of a free surface. *Fig. 49* shows that the Taoudeni and Kufrah sedimentary basins have only small topographic variations and that the differences through time back to 50 Ma are minor. This is actually to be expected for regions that have not experienced strong tectonic deformations during this time. For this reason, using a free surface or not will not influence dynamic topography to a large degree, in these regions. Interestingly, the Congo Basin shows an increase in basin subsidence in the Neogene, around the time at which the uppermost layer of sediments in the basin was deposited. We have previously linked this subsidence to a prominent fast anomaly that is visible at a depth of approximately 1000 km in the SG06 tomography model and speculated that this fast anomaly may represent a high-density body which sinks in the mantle underneath the Congo Basin. However, this anomaly is not found in the other tomography models (section 2.2, *Table 1*) and is therefore not a robust feature. We do therefore also not consider the recent subsidence for Congo that is obtained using SG06 a robust finding.

Fig. 50 shows that including brittle and temperature-dependent behaviour in the crust and lithosphere has only little effect on topography for the Congo Basin. Similarly, mild diffusive erosion and sedimentation (with a diffusion coefficient of 10^{-6} m^2 s^{-1}) only causes small topographic changes. These are almost negligible in comparison with the variations in topography that are obtained by using other tomographic models as input into the mantle flow calculations (section 5). We find that using other tomography models, we can easily obtain variations in topography of several 100's of meters.

The Taoudeni, Kufrah and Congo basins experienced little tectonic deformation during the past 100 Ma making them ideal for examining the contribution of the mantle to surface topography changes. We find that topography changes in these basins are of small magnitude, in line with the observation of limited Cenozoic sedimentation. The influence of a temperature- and pressure-dependent rheology and a free surface is limited for these basins, owing to the fact that lithospheric deformation is only minor and rheological feedback effects are therefore small. This implies that the dynamic topography models can be expected to give a rather complete picture of topography for intracratonic basin regions. However, our conclusion cannot be extrapolated to active regions and we would, in fact, not expect it to hold for the East African Rift or the Atlas Mountains, for example.

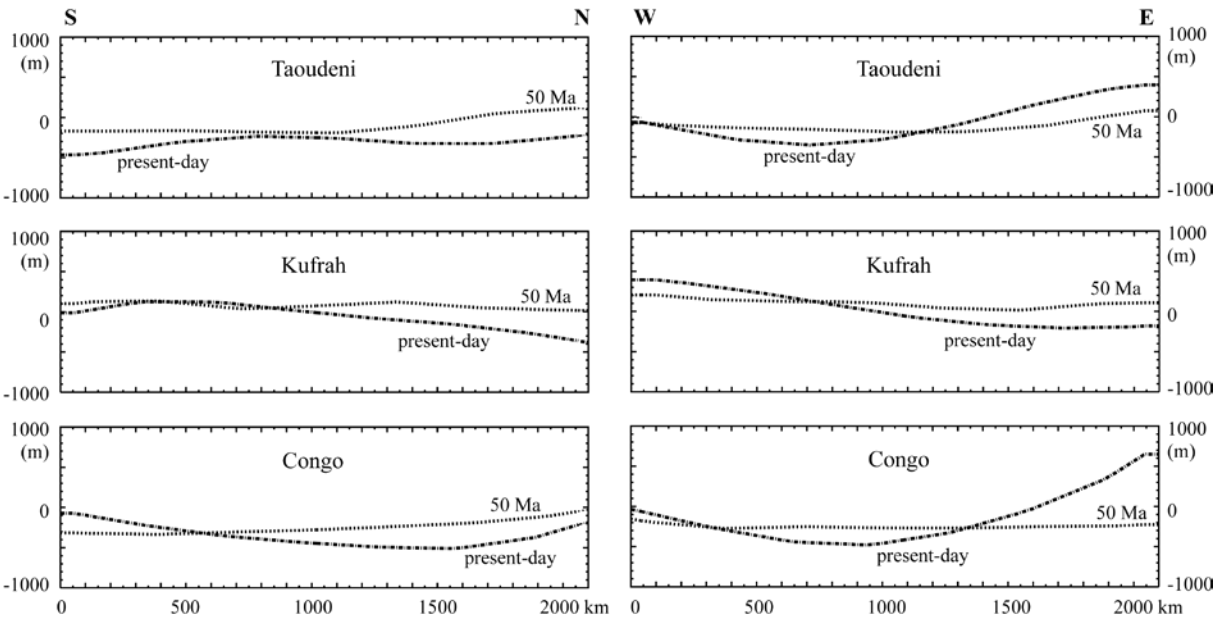

Fig. 49: 2D curves of topography at present-day and at 50 Ma obtained by coupling linear viscous lithosphere models with a free surface to mantle flow models (using SG06). Location of sections in *Fig. 46*.

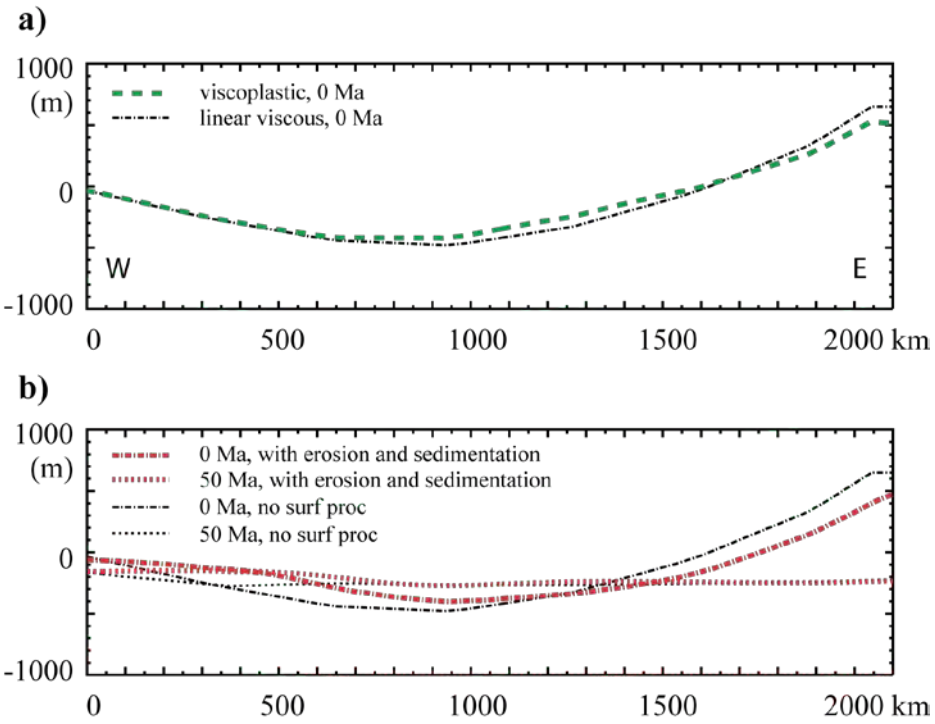

Fig. 50: Effect of a) rheology and b) surface processes on west-east topographic profiles for the Congo Basin (location of profile in *Fig. 48*).

8. CONCLUSIONS

We have compiled and analyzed a large number of tomography models, in order to assess what features are common and reliable. Our results confirm that creating mean models of mantle tomography (thereby averaging away those features that are not robust, and keeping the robust features) is a suitable approach to derive mantle density anomalies. Our mean model yields higher correlation of dynamic and residual topography than individual models, and their amplitude is about identical, whereas individual models tend to give too large amplitudes (by about 50%). In order to match amplitudes, seismic velocity variations within the lithosphere cannot be interpreted as density variations, and it is therefore important to use an appropriate lithosphere model. We find that using a thermal lithosphere model improves results in some regions compared to using a model that is based on the tomography models themselves, but in Africa, results become worse. By combining the mantle flow code with a lithosphere code, we found that in the African basins, lithosphere deformation seems to be very small and the treatment with a mantle flow code appears to be valid to a good approximation, for these regions.

Results of backward advection (regardless of pure or modified) always need to be considered with care. Essentially, only those features that are and remain in the mid-mantle are realistically backward advected. Hence backward advection is better suited at predicting the geoid (and true polar wander) back in time (e.g., Steinberger and O'Connell, 1997), as the geoid kernels go to zero close to the surface, whereas topography kernels go to their maximum value.

A somewhat realistic model of dynamic topography through geologic time at a given locations moving with a plate can therefore be expected, if the density anomalies causing it are in the mid-mantle, and/or if the plate is moving relatively fast such that a large part of dynamic topography change is due to this sideward motion (e.g., Müller et al., 2008b; Heine et al., 2010). Unfortunately, features in the uppermost mantle have the largest effect on dynamic topography, and there is a large anomaly in the uppermost mantle beneath East Africa. Also, the African plate is moving very slowly. Hence the conditions for predicting past dynamic topography are comparatively disadvantageous in the case of the African plate.

A better approach is the adjoint or inverse approach (e.g., Liu et al., 2008; Spasojevic et al., 2009). It essentially means iteratively determining the best initial condition such that a forward model (including the diffusion term) optimally matches the present-day condition.

The backward advection can be improved by choosing appropriate “zero density anomalies” at different depth levels. Since the density structure beneath “normal” ridges (away from hotspots) probably most closely corresponds to adiabatic, hence backward (downward) advected material beneath ridges should give approximately zero density anomaly, we plan to average seismic anomalies beneath “normal” ridges to re-define the zero level in future work.

Further future directions are

- joint inversion of the viscosity structure for fitting geoid and topography (instead of just adopting the structure that best fits the geoid)
- considering lateral viscosity variations (in particular continent versus ocean)
- possibly use a joint model of mantle and lithosphere (Sobolev et al., 2009) also in those regions where substantial deformation can be expected

Acknowledgements

The research described in this report was funded by Statoil through “The African Plate” project. We thank Hans Morten Bjørnseth, Jakob Skogseid and Allison Kennedy for their continued interest in this project. The authors also benefitted from an IS-DAAD collaborative research grant (“Could the mantle cause subsidence of the Congo Basin?” from the Norwegian Research Council and the Deutscher Akademischer Austausch Dienst) and B.S. and S.B. from their stay at the Centre for Advanced Study (2010/2011) in Oslo. We thank all authors who kindly made data available to us: Michael Antolik, Thorsten Becker, Stewart Fishwick, Yu “Jeff” Gu, Miaki Ishii, Sergei Lebedev, Michael Pasyanos, Keith Priestley, Catherine A. Rychert, and Nathan Simmons. We thank Stephanie Werner for providing her crustal model from gravity inversion and Walter Mooney, Carmen Gaina and Trond Torsvik for outlines of cratonic areas. Most of our figures were made using GMT (Wessel and Smith, 1991).

9. REFERENCES

Amante, C. and B. W. Eakins, 2009. ETOPO1 1 Arc-Minute Global Relief Model: Procedures, Data Sources and Analysis. NOAA Technical Memorandum NESDIS NGDC-24, 19 pp.

Armitage, J.J. and Allen, Ph.A., 2010. Cratonic basins and the long-term subsidence history of continental interiors, *J. Geol. Soc. Lond.*, **167**, 61-70

Antolik, M., Gu, Y.J., Ekström, G., and Dziewonski, A.M., 2003. J362D28: a new joint model of compressional and shear velocity in the Earth's mantle, *Geophys. J. Int.*, **153**, 443–466

Artemieva I.M., 2006. Global 1°x1° thermal model TC1 for the continental lithosphere: implications for lithosphere secular evolution. *Tectonophysics*, **416**, 245–277

Ayarza, P., Alvarez-Lobato, F., Teixell, A., Arboleya, M.L., Tesón, Julivert, M. and Charroud, M., 2005. Crustal structure under the central High Atlas Mountains (Morocco) from geological and gravity data, *Tectonophy*., **400**, 67-84

Bassin, C., G. Laske, and G. Masters, 2000. The current limits of resolution for surface wave tomography in North America, *Eos Trans. AGU*, 81(48), Fall Meet. Suppl., Abstract S12A-03

Becker, T.W. and Boschi, L., 2002. A comparison of tomographic and geodynamic mantle models, *Geochem. Geophys. Geosyst.*, **3**, 2001GC000168

Buiter, S.J.H. and Ellis, S., in prep. The role of the initiation phase in numerical subduction models

Burke, K., Gunnell, Y., 2008. The African Erosion Surface: A Continental-Scale Synthesis of Geomorphology, Tectonics, and Environmental Change over the Past 180 Million Years. *Geol. Soc. Am. Mem.* **201**, 66 p., doi: 10.1130/2008.1201

Conrad, C.P., and Gurnis, M., 2003. Seismic tomography, surface uplift, and the breakup of Gondwanaland: Integrating mantle convection backwards in time, *Geochem. Geophys. Geosyst.* **4**(3), 1031, doi:10.1029/2001GC000299

Conrad, C.P.,and Lithgow-Bertelloni, C., 2006. Influence of continental roots and asthenosphere on plate-mantle coupling, *Geophys. Res. Lett.*, **33**, L05312, doi:10.1029/2005GL025621

Crosby, A.G., Fishwick, S., White, N., 2010. Structure and evolution of the intracratonic Congo Basin. *Geochem. Geophys. Geosys.* **11(6)**, Q06010, doi:10.1029/2009GC003014

Daly, M.C., Lawrence, S.R., Diemu-Tshiband, K., Matouana, B., 1992. Tectonic evolution of the Cuvette Centrale, Zaire. *J. Geol. Soc. Lond*. **149**, 539-546, doi:10.1144/gsjgs.149.4.0539

Downey, N.J., Gurnis, M., 2009. Instantaneous dynamics of the cratonic Congo basin. *J. Geophys. Res.* **114**, B06401, doi:10.1029/2008JB006066

Durek, J.J. and G. Ekstrom, 1996. A radial model of anelasticity consistent with long-period surface wave attenuation, *Bull. seism. Soc. Am.*, **86,** 144–158

Dziewonski, A.M. and D.L. Anderson, 1981. Preliminary reference Earth model, *Phys. Earth planet. Inter.*, **25,** 297–356

Ebinger, C.J. and N.H. Sleep, 1998. Cenozoic magmatism throughout east Africa resulting from impact of a single plume. *Nature* **395**, 788-791

Ekström, G., J. Tromp, and E.W.F. Larson, 1997. Measurements and global models of surface wave propagation, *J. Geophys. Res.*, **102,** 8137–8157

Ellis, S. and Buiter, S.J.H., in prep. Three-dimensional thrust wedges.

Fishwick, S., 2010. Surface wave tomography: Imaging of the lithosphere–asthenosphere boundary beneath central and southern Africa? *Lithos* **120** (1-2), 63-73

Forte, A.M., Quere, S., Moucha, R., Simmons, N.A., Grand, S.P., Mitrovica, J.X., Rowley, D.B., 2010. Joint seismic–geodynamic-mineral physical modelling of African geodynamics: A reconciliation of deep-mantle convection with surface geophysical constraints, *Earth Planet. Sci. Lett.*, **295**, 329–341

Giresse, P., 2005. Mesozoic-Cenozoic history of the Congo Basin. *J. Afr. Earth Sci*. **43**, 301-315

Gleason, G.C. and Tullis, J., 1995. A flow law for dislocation creep of quartz aggregates determined with the molten salt cell. *Tectonophysics* **247**, 1–23

Grand, S.P., 2002. Mantle shear-wave tomography and the fate of subducted slabs. *Phil. Trans. R. Soc. Lond. A.*, **360**, 2475–2491

Gu, Y.J. and A.M. Dziewonski, 2002. Global variability of transition zone thickness, *J. Geophys. Res.*, **107,** 10.1029/2001JB000489.

Gu, Y.J., Dziewonski, A.M., and Ekström, G., 2003. Simultaneous inversion for mantle shear velocity and topography of transition zone discontinuities, *Geophys. J. Int.*, **154**, 559–58

Gubanov, A.P. and W.D. Mooney, 2009. New global geological maps of crustal basement age, Eos Trans. AGU 90(52), Fall Meet. Suppl, Abstract T53B-1583

Gurnis, M., Mitrovica, J.X., Ritsema, J., and van Heijst, H.-J., 2000. Constraining mantle density structure using geological evidence of surface uplift rates: The case of the African superplume, *Geochem., Geophys., Geosyst.*, **1**, 1999GC000035

Hager, B.H., and O'Connell, R.J., 1979. Kinematic models of large-scale mantle flow, *J. geophys. Res.*, **84**, 1031–1048

Hager, B.H., and O'Connell, R.J., 1981. A simple global model of plate dynamics and mantle convection, *J. geophys. Res.*, **86**, 4843–4867

Hartley, R.W., Allen, P.A., 1994. Interior cratonic basins of Africa: relation to continental break-up and role of mantle convection. *Basin Research* **6**, 95-113

Heine, C., Müller, R.D., Steinberger, B., and DiCaprio, L., 2010. Integrating deep Earth dynamics in paleogeographic reconstructions of Australia, *Tectonophysics*, **483**, 135–150

Hirth, G. and Kohlstedt, D., 1996. Water in the oceanic upper mantle; implications for rheology, melt extraction and the evolution of the lithosphere. *Earth Planet. Sci. Lett.* **144**, 93–108

Hofmann, C., Courtillot, V., Feraud, G., Rochette, P., Yirgu, G., Ketefo, E. Pik, R., 1997. Timing of the Ethiopian flood basalt event and implications for plume birth and global change, *Nature*, **389**, 838-841

Jordan, T.H., 1988. Structure and formation of the continental tectosphere. *J. Petrology*, Special Lithosphere Issue, 11–37

Kaus, B.J.P., Connolly, J.A.D., Podladchikov, Yu.Yu. and Schmalholz, S.M., 2005. Effect of mineral phase transitions on sedimentary basin subsidence and uplift, *Earth Planet. Sci. Lett.*, **233**, 213-228

Kennett, B. L. N., and E. R. Engdahl, 1991. Traveltimes for global earthquake location and phase identification, *Geophys. J. Int.*, **105**, 429–465

Kennett, B. L. N., E. R. Engdahl, and R. Buland, 1995. Constraints on seismic velocities in the Earth from travel times, *Geophys. J. Int.*, **122**, 108–124, doi:10.1111/j.1365- 246X.1995.tb03540.x

Kustowski B., Ekström G., and Dziewonski, A.M., 2008a. Anisotropic shear-wave velocity structure of the Earth's mantle: A global model, *J. Geophys. Res.*, **113**, B06306. doi:10.1029/-2007JB005169

Kustowski, B., G. Ekström, and A. M. Dziewonski, 2008b. The shear-wave velocity structure in the upper mantle beneath eurasia. *Geophys. J. Int.*, **174**, 978–992

Lebedev, S., and van der Hilst, R.D. 2008. Global upper-mantle tomography with the automated multimode inversion of surface and S-wave forms, *Geophys. J. Int.*, **173**, 505–518

Lee, C.-K., Han, S.-C., and Steinberger, B., in press. Influence of variable uncertainties in seismic tomography models on constraining mantle viscosity from geoid observations, *Phys. Earth Planet. Inter.*

Li, C., van der Hilst, R.D., Engdahl, E.R., and Burdick S., 2008. A new global model for P wave speed variations in Earth's mantle, *Geochem. Geophys. Geosyst.*, **9**, Q05018, doi:10.1029/-2007GC001806

Liu, L., Spasojevic, S., Gurnis, M., 2008. Reconstructing Farallon Plate Subduction Beneath North America Back to the Late Cretaceous, *Science*, **322**, 934

Masters, G., Laske, G., Bolton, H., and Dziewonski, A., 2000. The Relative Behavior of Shear Velocity, Bulk Sound Speed, and Compressional Velocity in the Mantle: Implications for Chemical and Thermal Structure, in: S. Karato, A.M. Forte, R.C. Liebermann, G. Masters and L. Stixrude (eds.) Earth's Deep Interior, *AGU Monograph* **117**, AGU, Washington D.C.

Mégnin C., and Romanowicz, B., 2000. The shear velocity structure of the mantle from the inversion of of body, surface and higher modes waveforms, *Geophys. J. Int.*, **143**, 709–728, 2000

Middleton, M.F., 1989. A model for the formation of intracratonic sag basins, *Geophys. J. Int.*, **99**,665-676

Missenard, Y., Zeyen, H., Frizon de Lamotte, D. and Leturmy, P., 2006. Crustal versus asthenospheric origin of relief of the Atlas Mountains of Morocco, *J. Geophys. Res.*, **111**, B03401, doi:10.1029/2005JB003708

Mooney, W.D., G. Laske, and G. Masters, 1998. CRUST-5.1: a global crustal model at 5º x 5º. *J. Geophys. Res.*, **103**, 727–747

Montagner, J.-P., B. Marty, E. Stutzmann, D. Sicilia, M. Cara, R. Pik, J.-J. Lévèque, G. Roult, E. Beucler and E. Debayle, 2007. Mantle upwellings and convective instabilities revealed by seismic tomography and helium isotope geochemistry beneath eastern Africa, *Geophys. Res. Lett.* **34**, L21303, doi:10.1029/2007GL031098

Montelli, R., Nolet, G., Dahlen, F.A., and Masters G., 2006. A catalogue of deep mantle plumes: new results from finite-frequency tomography, *Geochem. Geophys. Geosyst.*, **7**, Q11007, doi:10.1029/2006GC001248

Müller, R.D., Sdrolias, M., Gaina, C., and Roest, W.R., 2008a. Age, spreading rates, and spreading asymmetry of the world's ocean crust, *Geochem. Geophys. Geosyst.*, **9**, Q04006, doi:10.1029/2007GC001743

Müller, R.D., Sdrolias, M., Gaina, C., Steinberger, B., and Heine, C., 2008b. Long-term sea-level fluctuations driven by ocean basin dynamics, *Science*, **319**, 1357–1362

Nataf, H.C. and Y. Ricard, 1996. 3SMAC: an a priori tomographic model of the upper mantle based on geophysical modeling. *Phys. Earth. Planet. Int.*, **95**, 101–22

Pasyanos, M.E., Nyblade, A.A., 2007. A top to bottom lithospheric study of Africa and Arabia. *Tectonophysics* **444**, 27-44, doi:10.1016/j.tecto.2007.07.008

Panning, M.P., and Romanowicz, B.A., 2006. A three dimensional radially anisotropic model of shear velocity in the whole mantle, *Geophys. J. Int.*, **167**, 361–379

Priestley, K., McKenzie, D., Debayle, E., and Pilidou, S., 2008. The African upper mantle and its relationship to tectonics and surface geology, *Geophys. J. Int.*, **175**, 1108–1126

Quinlan, G.M., 1987. Models of subsidence mechanisms in intracratonic basins, and their applicability to North American examples, in: Sedimentary Basins and Basin-Forming Mechanisms, Beaumont, C. and Tankard, A.J. (eds), *Can. Soc. Petr. Geol.*, Calgary, Alberta, p. 463-481

Reusch, A.M., Nyblade, A.A., Wiens, D.A., Shore, P.J., Ateba, B., Tabod, C.T., and Nnange , J.M., 2010. Upper mantle structure beneath Cameroon from body wave tomography and the origin of the Cameroon Volcanic Line, *Geochem. Geophys. Geosyst.*, **11**, Q10W07, doi:10.1029/-2010GC003200.

Ritsema, J., van Heijst, H.J., and Woodhouse, J.H., 1999. Complex shear wave velocity structure imaged beneath Africa and Iceland, *Science*, **286**, 1925--1928

Ritsema, J., van Heijst, H.J., and Woodhouse J.H., 2004. Global transition zone tomography, *J. Geophys. Res.*, **109**, B02302, doi:10.1029/2003JB002610

Ritzwoller, M. H., N. M. Shapiro, M. P. Barmin, and A. L. Levshin, 2002. Global surface wave diffraction tomography, *J. Geophys. Res.*, **107**(B12), 2335, doi:10.1029/2002JB001777, 2002

Romanowicz, B. 2003, Global Mantle Tomography: Progress Status in the Past 10 Years, *Annu. Rev. Earth Planet. Sci.* **31**:303–28

Rychert, C.A., and Shearer, P.M., 2009. A global view of the lithosphere-asthenosphere boundary, *Science*, **324**, 495–498

Rybacki, E. and Dresen, G., 2000. Dislocation and diffusion creep of synthetic anorthite aggregates. *J. Geophys. Res*. **105**, 26,017–26,036

Rychert, C.A., Shearer, P.M., Fischer, K.M., 2010. Scattered wave imaging of the lithosphere–asthenosphere boundary, *Lithos* 120 (1-2), 173-185, doi:10.1016/j.lithos.2009.12.006

Sebai, A., E. Stutzmann, J.-P. Montagner, D. Sicilia and E. Beucler, 2006. Anisotropic structure of the African upper mantle from Rayleigh and Love wave tomography. *Phys. Earth Planet. Int.*, **155**, 48-62

Seber, D., Sandvol, E., Sandvol, C., Brindisi, C. and Barazangi, M., 2001. Crustal model for the Middle East and North Africa region: implications for the isostatic compensation mechanism, *Geophys. J. Int.*, **147**, 630-638

Simmons, N.A., Forte, A.M., and Grand S.P., 2007. Thermochemical structure and dynamics of the African super-plume, *Geophys.Res. Lett.*, **34**, L02301, doi:10.1029/2006GL028009

Simmons, N.A., Forte, A.M., and Grand S.P., 2009. Joint seismic, geodynamic and mineral physical constraints on three-dimensional mantle heterogeneity: Implications for the relative importance of thermal versus compositional heterogeneity, *Geophys. J. Int.*, **177**, 1284–1304

Shapiro, N.M., and Ritzwoller, M.H., 2002. Monte-Carlo inversion for a global shear velocity model of the crust and upper mantle, *Geophys. J. Int.*, **151**, 88–105

Spasojevic, S., Liu, L., and Gurnis, M., 2009. Adjoint models of mantle convection with seismic, plate motion and stratigraphic constraints: North America since the Late Cretaceous, *Geochem., Geophys., Geosyst.*, **10**, Q05W02, doi:10.1029/2008GC002345

Steinberger, B., and O'Connell, R.J., 1997. Changes of the Earth's rotation axis owing to advection of mantle density heterogeneities, *Nature*, **387**, 169–173

Steinberger, B., and Calderwood, A., 2006. Models of large-scale viscous flow in the Earth's mantle with constraints from mineral physics and surface observations, *Geophys. J. Int.*, **167**, 1461–1481

Steinberger, B., and Holme, R., 2002. An explanation for the shape of Earth's gravity spectrum based on viscous mantle flow models, *Geophys. Res. Lett.*, **29**(21), 2019, doi:10.1029/2002GL015476

Steinberger, B., and Holme, R., 2008. Mantle flow models with core-mantle boundary constraints and chemical heterogeneities in the lowermost mantle, *J. Geophys. Res.*, **113**, B05403, doi:10.1029/2007JB005080

Steinberger, B., Werner S.C., and Torsvik, T.H., 2010. Deep versus shallow origin of gravity anomalies, topography and volcanism on Earth, Venus and Mars, *Icarus*, **207**, 564–577

Sobolev, S.V., Popov, A., and Steinberger, B., 2009. Constraining rheology and water content in the upper mantle by modeling plate tectonics, *Geochim. Cosmochim. Ac.* **73** (13), Supp. 1, A1244

Teixell, A., Arboleya, M.-L. and Julivert, M., 2003. Tectonic shortening and topography in the central High Atlas (Morocco), *Tectonics*, **22(5)**, doi:10.1029/2002TC001460

Teixell, A., Ayarza, P., Zeyen, H., Fernàndez, M. and Arboleya, M.-L., 2005. Effects of mantle upwelling in a compressional setting: the Atlas Mountains of Morocco, *Terra Nova*, **17**, 456-461, doi: 10.1111/j.1365-3121.2005.00633.x

Tesauro, M., Kaban, M.K., Cloetingh, S.A.P.L., 2008. EuCRUST-07: A new reference model for the European crust, *Geophys. Res. Lett.*, **35**, 5, L05313

Torsvik, T.H., Smethurst, M.A., Burke, K., and Steinberger, B., 2006. Large igneous provinces generated from the margins of the large low-velocity provinces in the deep mantle, *Geophys. J. Int.*, **167**, 1447–1460

Torsvik, T. H., Steinberger, B., Gurnis, M., and Gaina, C., 2010. Plate tectonics and net lithosphere rotation over the past 150 My, *Earth Planet. Sci. Lett.*, **291**, 106–112

Wessel, P. and W. H. F. Smith, 1991. Free software helps map and display data, *EOS Trans.* AGU, **72**, 441

Wieczorek, M. A., 2007. The gravity and topography of the terrestrial planets, *Treatise on Geophysics*, **10**, 165–206

Wigger , P., Asch, G., Giese, P., Heinsohn, W.-D., El Alami, S.O. and Ramdani, F., 1992. Crustal structure along a traverse across the Middle and High Atlas mountains derived from seismic refraction studies, *Geol. Rundschau*, **81(1)**, 237-248

Wilson, M. and R. Guiraud, 1992. Magmatism and rifting in Western and Central Africa, from Late Jurassic to Recent times. *Tectonophysics*, **213**, 203-225

APPENDIX A: SHORT DESCRIPTION OF TOMOGRAPHY MODELS

P-wave tomography models

MITP08: The compressional wave tomography model by Li et al. (2008) utilizes many different P-wave phases from earthquakes occurring during the period of 1964-2007. Data sources include processed traveltimes from global databases, waveform modelling of core phases (PKP and Pdiff), and temporary regional arrays. Velocity perturbations are calculated with respect to values computed from the P-wave global reference model *ak135* (Kennett et al, 1995). Crustal contributions are removed by regularization to a 3-D crustal model, composed of CRUST2.0 (Bassin et al., 2000) and regional crustal models. The MIT-P08 model is parameterized with a rectangular adaptive grid mesh, defined with 0.7º x0.7º laterally and variable thicknesses radially. Like most P-wave models, the MIT-P08 model is not useful in imaging cratonic lithosphere but successful in imaging subducting slabs. Under Africa, the MITP08 model has poor coverage over most of the continent except for South Africa and the Afar Region, primarily because of data from recent temporary arrays.

P362D28: The P-wave tomography model by Antolik et al. (2003) is part of a joint compressional and shear wave inversion. Travel time and source locations of P and PP-P waves were taken from the ISC global database. The model inversion is carried out over a triangular grid created by a horizontal tessellation of 362 spherical splines and 14 radial cubic B-splines (~spherical harmonic of degree 18). Corrections to velocities are made with respect to CRUST5.1 (Mooney et al., 1998) for the crust and PREM Q to account for attenuation affects commonly observed in long-period waves. P362D28 has very poor resolution above 670 km depth. This compressional wave tomography model is useful for long-wavelength features in the upper mantle. A checkerboard test reveals that resolution under Africa is best between approximately 600 km and 2000 km depth.

PRI-P05: The PRI-P05 model by Montelli et al. (2006) consists of P, PP-P, and pP-P waves from the ISC global database. Velocity perturbations are calculated with respect to the *iasp91* global model (Kennett and Engdahl, 1991). Crustal corrections are made with respect to CRUST2.0 (Bassin et al., 2000). The PRI-P05 model is parameterized by a tetrahedral delauney mesh. The authors utilize this model in conjuction with their shear wave models to image plumes. However, the cratonic lithosphere under Africa is poorly imaged and large structures are mainly observed in the upper mantle under Africa.

S-wave Tomography Models

PRI-S05: The PRI-S05 model by Montelli et al. (2006) uses traveltimes of many different shear-wave phases. As with the compressional wave model PRI-P05, the model is parameterized with a tetrahedral delauney mesh. Data for PRI-S05 comes from long period S-wave arrivals and ScS and SS-S wave differential arrival times from the ISC global database. Residual traveltimes were calculated with respect to the *iasp91* global velocity model (Kennett and Engdahl, 1991). Under Africa, PRI-S05 can adequately image the Afar plume and cratonic lithosphere, but the cratons appear thicker than in other S-wave models. Like PRI-P05, this model is best at imaging plume structures.

S20RTSb: The S20RTSb shear wave tomography model by Ritsema et al. (2004) uses normal mode splitting, Rayleigh wave phase velocity, and body waves for the data. Data sources include events from 1996-2000 in shear wave velocity residuals are calculated with respect to

CRUST5.1 (Mooney et al., 1998) and global velocity model PREM (Dziewonski and Anderson, 1981). S20RTSb is parameterized with 21 radial spline function and horizontally by spherical harmonics up to degree 20. S20RTSb is good at imagining African cratonic lithosphere structure.

S362ANI: The Harvard model S362ANI by Kustowski et al. (2008a,b) uses surface waves in addition to body wave travel times to produce an anisotropic tomography model. S362ANI uses body waves from 219 events between 1994 and 2003 from the GSN and FDSN networks and ~55,000 phase arrivals from surface waves. S362ANI contains 3.5 times more rays than previous Harvard model TOPO362D1 (Gu et al., 2003). Crustal effects are corrected using model CRUST2.0 (Bassin et al., 2000). Velocity perturbations are calculated with respect to a modified PREM global velocity model (Dziewonski and Anderson, 1981), called STW105 (Kustowski et al., 2008a). It should be noted that the publicly available S362ANI model can calculate velocity residuals with respect to other 1D global models such as PREM and *ak135*. S362ANI compares arrivals of radial and transverse components of shear waves, therefore calculating the anisotropic component. This model only presents results for anisotropy in the upper 300 km, which consequently allows for a better fit with the surface waves than if anisotropy was not included. The model is parameterized horizontally with 362 spherical splines and vertically with 16 radial cubic B-splines. This shear wave model has very good ray path coverage over Eurasia and the Pacific, but poor coverage for Africa. However, the anisotropy model is able to resolve a good image of the upper mantle structure under Africa.

S362D28: S362D28 is part of a joint compressional and shear wave tomographic inversion (Antolik et al., 2003). Data includes travel times from surface waves and numerous phases of shear waves from the ISC global catalogue. The model is parameterized horizontally with 362 spherical splines and vertically with 14 radial splines. Perturbations in shear wave velocities were calculated with respect to PREM (Dziewonski and Anderson, 1981) and corrections for crustal effects with respect to CRUST5.1 (Mooney et al., 1998). Upper mantle structure under Africa is adequately resolved, but only long-wavelength structures are resolved in the lower mantle.

SAW24B16: The shear wave tomography model SAW24B16 by Megnin and Romanowicz (2000) uses SH waveforms from body waves, surface waves, and long period waves. Data is from modelled waveforms from events in the period of 1977 to 1997 in the IRIS and GEOSCOPE catalogs. The model is spatially derived with horizontal spherical splines up to degree 24 and 16 radial cubic B-splines, but is organized differently in the upper and lower mantles. SAW24B16 consists of velocity perturbations from the PREM global model (Dziewonski and Anderson, 1981). This Berkeley model resolves upper mantle structure under Africa quite well.

SAW642AN: Model SAW642AN by Panning and Romanowicz (2006) is another anisotropic tomography model, produced from surface and shear body waves. Data comes from modelled waveforms from events between 1995 and 1999 in the IRIS and GEOSCOPE catalogues. The model is spatially parameterized with spherical B-splines to degree 4 (~degree 24 spherical harmonics) laterally and vertically with 16 radial cubic B-splines. SAW642AN consists of shear wave and anisotropic component perturbations relative to the global model PREM (Dziewonski and Anderson, 1981) and a radial Q (anelastic) structure from model QL6 (Durek and Ekström, 1996). Ray coverage is poorest under Africa, as usual, and upper mantle structure is poorly resolved under Africa. Also the Afar superplume is poorly imaged.

SB4L18: Model SB4L18 by Masters et al., (2000) uses body waves of S, SS, and ScS phases and long-period surface waves. Body waves are collected from the ISC catalogue and long-period surface waves are from the GDSN catalogue. SB4L18 is parameterized up to degree 20 spherical harmonics in the mantle and vertically with 18 layers varying in thickness from 100 km to 200 km. Perturbations are calculated with respect to the PREM global model (Dziewonski and Anderson, 1981), with crustal corrections from CRUST5.1 (Mooney et al., 1998).

SG06: Model SG06, an update of Grand (2002) is an older shear wave tomography model from the UT-Austin group. Data for this model comes from numerous networks (IRIS, GSN, GEOSCOPE, MedNet, CNSN, WWSN, and temporary PASSCAL arrays). Many different phases of shear waves were used in this inversion, and velocity perturbations are given relative to TNA/SNA for the upper mantle and PREM (Dziewonski and Anderson, 1981) for the lower mantle. The model is parameterized with an irregular grid of 2° x 2° laterally and varying from 75 km to 230 km in depth.

TOPOS362D1: The Harvard model TOPOS362D1 from Gu et al. (2003) uses numerous shear wave phases and surface waveforms. Data is from shear waves from events recorded between 1977 and 1998 from the ISC catalogue, long-period waveforms, surface wave dispersions from Ekström et al., (1997), and differential travel times of SS-SdS and S400S-S670S (Gu and Dziewonski, 2002). The model is parameterized spatially with 362 spherical B-splines and radially with 14 cubic B-splines with a 670km discontinuity. Crustal effects are corrected using CRUST5.1 (Mooney et al., 1998) and velocity perturbations are calculated relative to PREM (Dziewonski and Anderson, 1981). This tomography model is particularly useful in imaging the topography of the 400 km and 670 km discontinuities. However, under Africa, resolution is quite poor.

TX2007: Model TX2007 is a tomography model by Simmons et al. (2007, 2009) consisting of shear wave velocity perturbations from a joint inversion of seismic data and geodynamic constraints. Data comes from various shear wave phases, same as SGO6 (Grand, 2002). The velocity perturbations are corrected for crustal effects with CRUST5.1 (Mooney et al., 1998) and calculated relative to the reference model TNA/SNA for the upper mantle and PREM (Dziewonski and Anderson, 1981) for the lower mantle. The geodynamic constraints come from global free-air gravity, tectonic plate divergences, excess ellipticity of the crust-mantle boundary, and dynamic surface topography. The model is parameterized with an irregular grid of 250 km x 250 km laterally and varying thickness from 75 to 240 km.

Upper Mantle Tomography Models

CU_SDT1.0: Global upper mantle tomography model CU_SDT1.0 (Ritzwoller et al., 2002; Shapiro and Ritzwoller, 2002) uses diffraction tomography on surface waves, rather than the commonly used ray theory. Data sources include events from the period of 1977-1999 in GSN, GDSN, GEOSCOPE, and temporary regional arrays. Phase and group velocities were calculated from Rayleigh and Love waves using diffraction tomography methods on a 2º x 2º grid for certain periods. The surface wave diffraction maps are then inverted using a Monte-Carlo inversion to geographical points. Velocity perturbations are made with respect to global model *ak135* (Kennett et al, 1995), however PREM (Dziewonski and Anderson, 1981) and CRUST5.1 (Mooney et al., 1998) are included in the initial model for the inversion.

CU_SRT1.0: Global upper mantle tomography model CU_SRT1.0 (Ritzwoller et al., 2002; Shapiro and Ritzwoller, 2002) is the ray theory companion to model CU_SDT1.0. CU_SRT1.0 uses the same data, Monte-Carlo inversions, and reference models as

CU_SDT1.0. Only the method in computing the surface wave dispersion maps is different – CU_SRT1.0 uses ray theory to calculate phase and group velocities, while CU_SDT1.0 uses diffraction tomography.

KP08: Model KP08 (Priestley et al., 2008) is an upper mantle tomography model for Africa made with fundamental (Rayleigh) and higher mode SV waves. Data comes from events in the period of 1977 and 2002, with seismograms from global and temporary arrays in IRIS, GEOSCOPE, GEOFON, and PASSCAL catalogues. Crustal corrections are made with 3SMAC (Nataf and Ricard, 1996) and velocity perturbations are calculated relative to a modified PREM global model.

LH08: Global upper mantle tomography model LH08 (Lebedev and Van der Hilst, 2008) uses fundamental and higher mode waves. LH08 uses phase velocities from fundamental mode (Rayleigh) and higher mode (S and multiple S) waves from events during the period of 1994 and 2002 in GSN, GEOSCOPE, GEOFON, IRIS, PASSCAL, CDSN, CNSN, KAZNET, MEDNET, and POSEIDON seismic bulletins. Velocity perturbations are calculated with respect to CRUST2.0 (Bassin et al., 2000) and global model *ak135* (Kennett et al., 1995) and parameterized with a dense grid of knots.

SF09: Regional model SF09 by Fishwick (2010) is an upper mantle tomography model of Africa computed from the most recent temporary seismic arrays. Data comes from permanent arrays and numerous temporary arrays across Africa, including the recent Africa Array (Nyblade et al., 2008). Velocity perturbations are made with respect to global velocity model *ak135* (Kennett et al., 1995) but the initial model for the inversion uses crustal model 3SMAC (Nataf and Ricard, 1996) and PREM (Dziewonski and Anderson, 1981) for the mantle. Model SF09 is parameterized with a grid of knots spaced 3º apart.

APPENDIX B: PRESENT-DAY DYNAMIC TOPOGRAPHY FOR INDIVIDUAL WHOLE-MANTLE TOMOGRAPHY MODELS

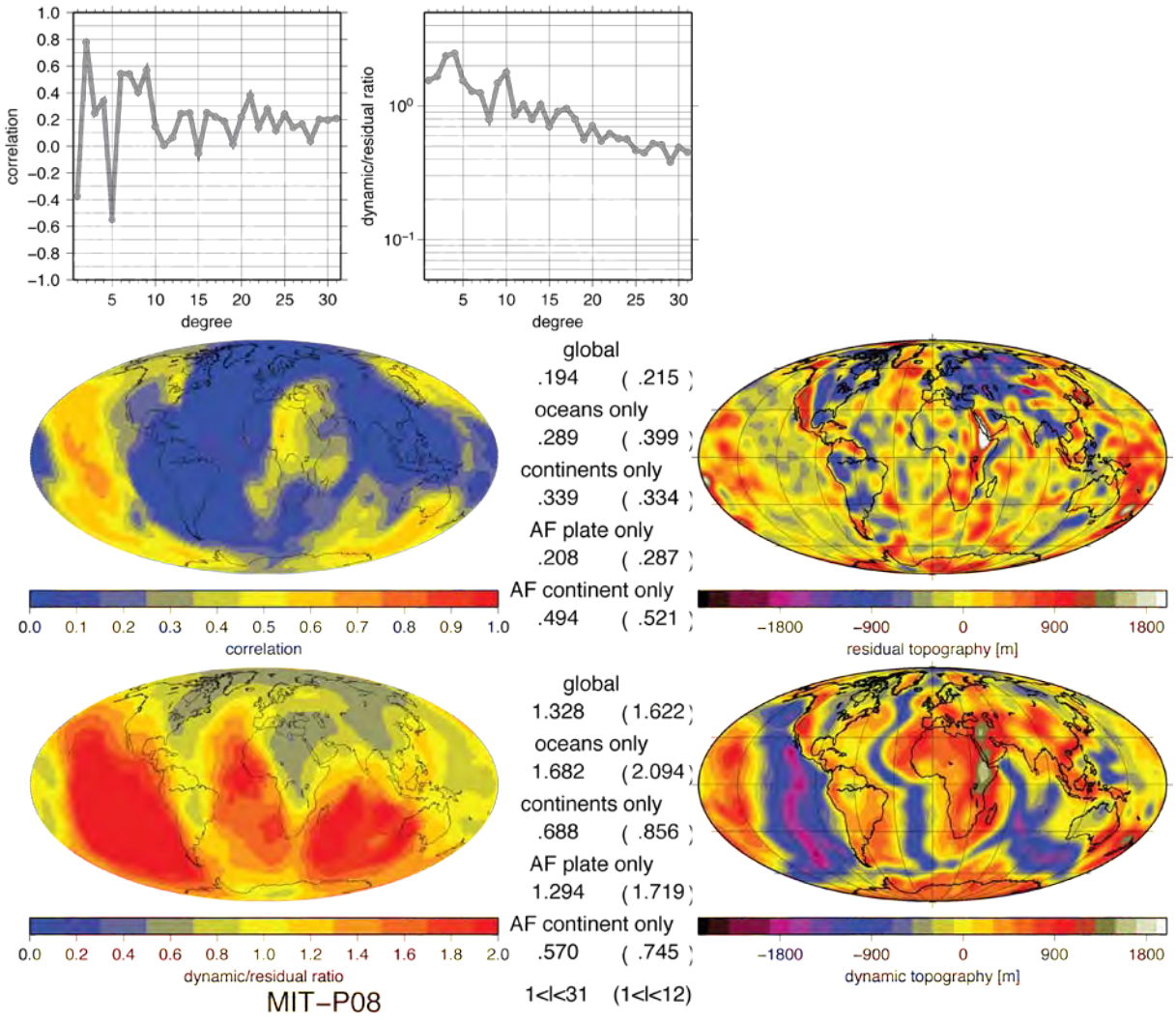

Figure S1: Results for the correlation and ratio between dynamic topography (computed based on tomography model MIT-P08) and residual topography. Cut-off S-wave anomaly 0.6%.

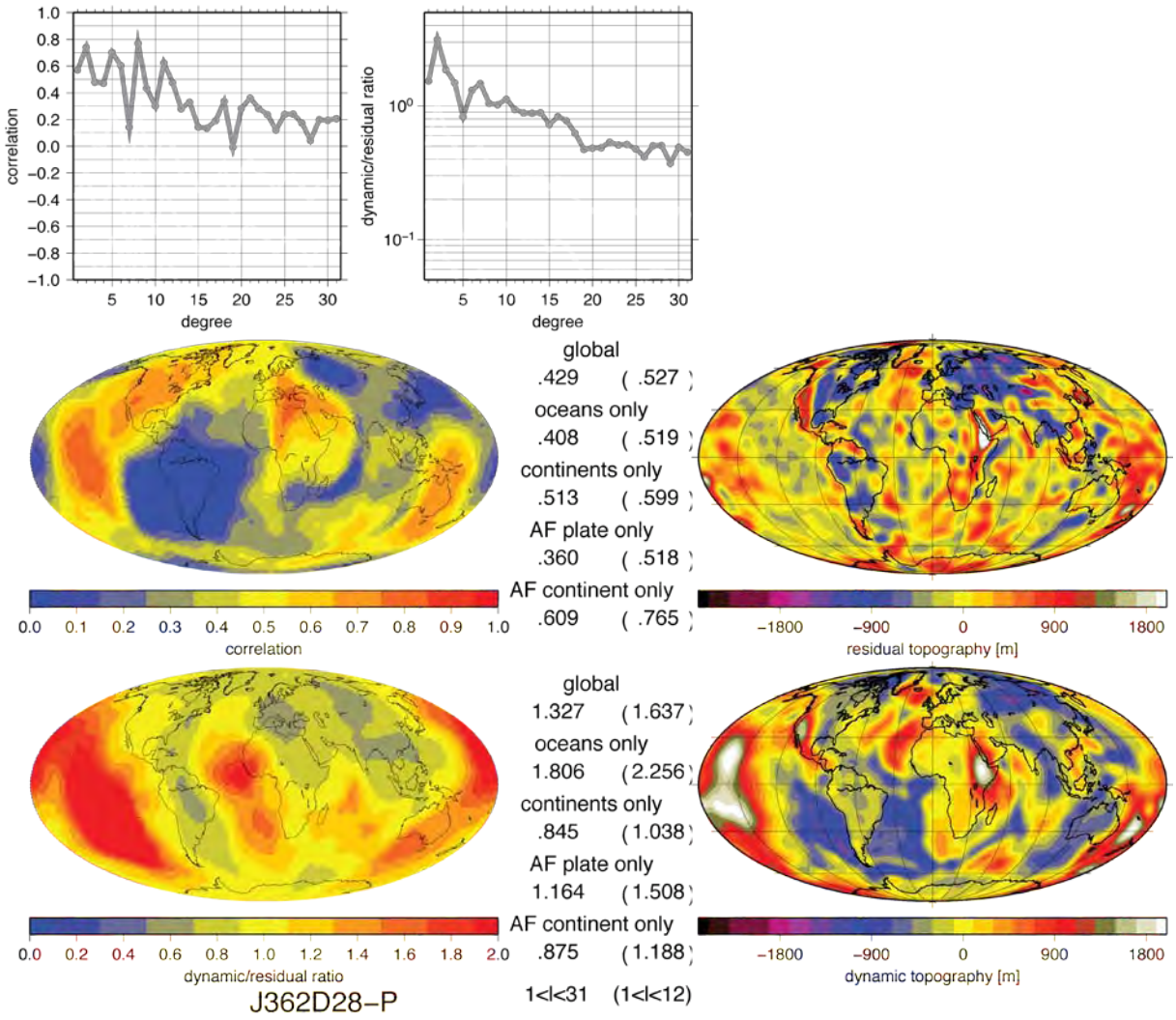

Figure S2: Results for the correlation and ratio between dynamic topography (computed based on tomography model P362D28) and residual topography. Cut-off S-wave anomaly 0.4%.

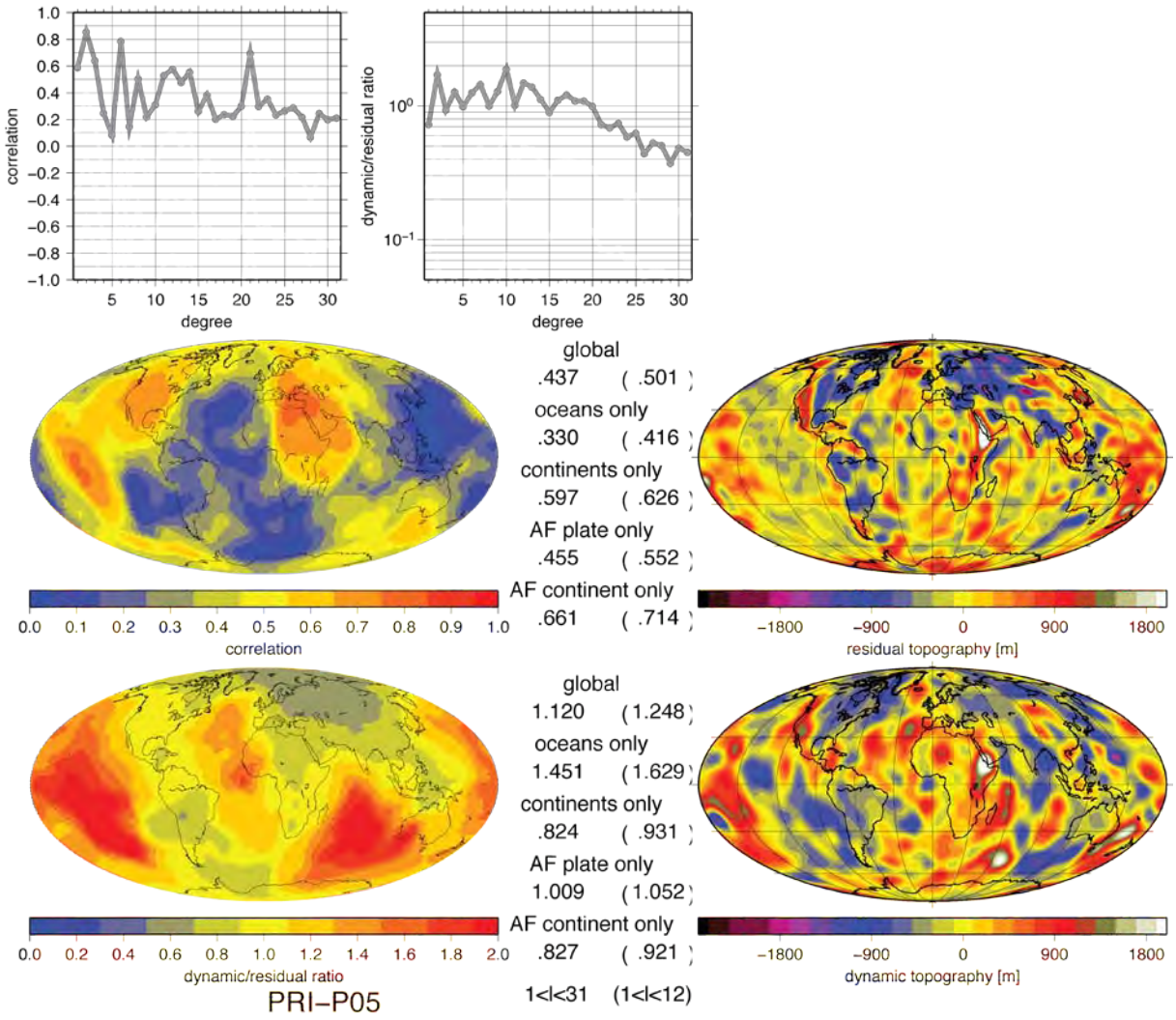

Figure S3: Results for the correlation and ratio between dynamic topography (computed based on tomography model PRI-P05) and residual topography. Cut-off S-wave anomaly 0.1%.

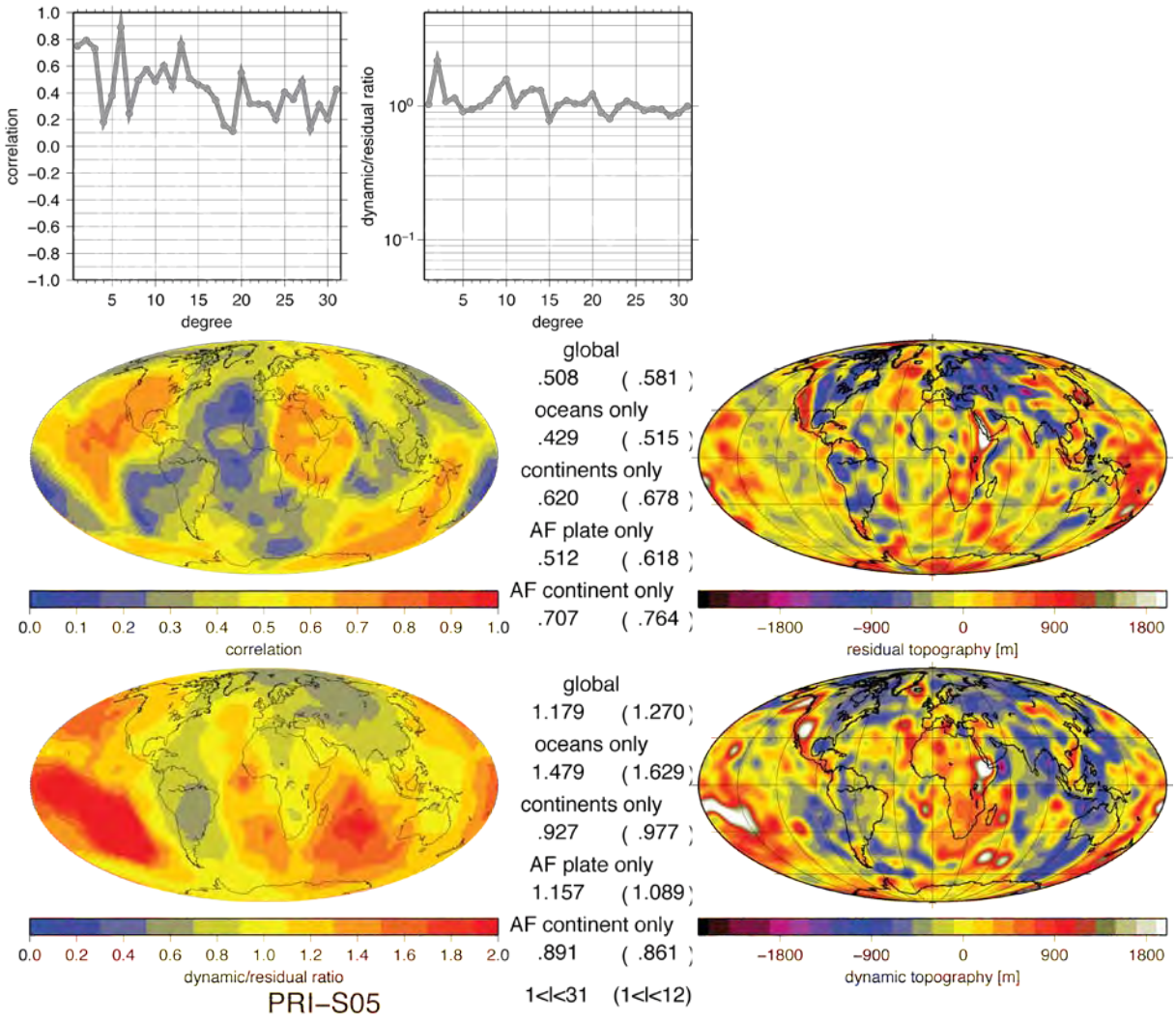

Figure S4: Results for the correlation and ratio between dynamic topography (computed based on tomography model PRI-S05) and residual topography. Cut-off S-wave anomaly -0.1%.

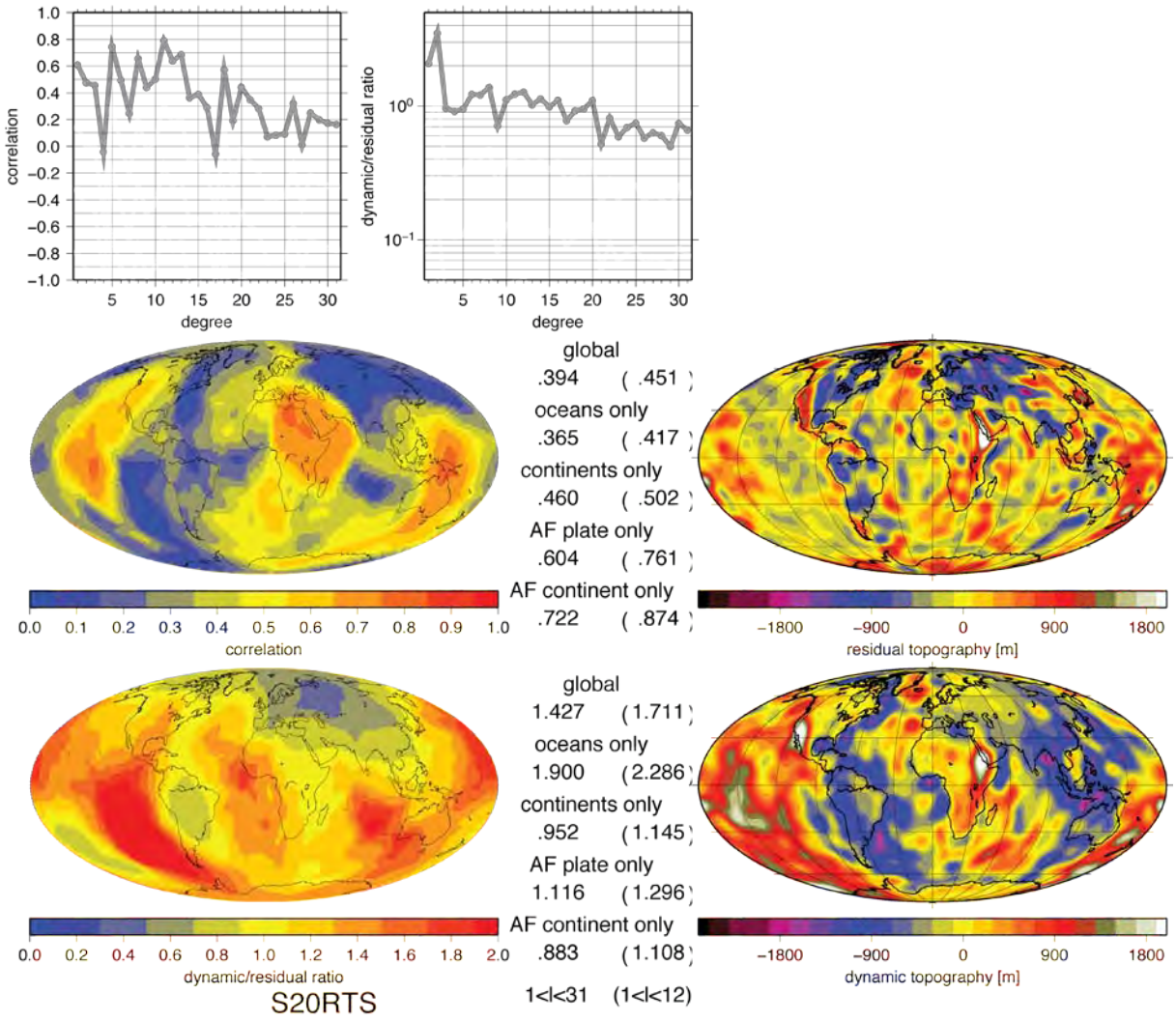

Figure S5: Results for the correlation and ratio between dynamic topography (computed based on tomography model S20RTSb) and residual topography. Cut-off S-wave anomaly 0%.

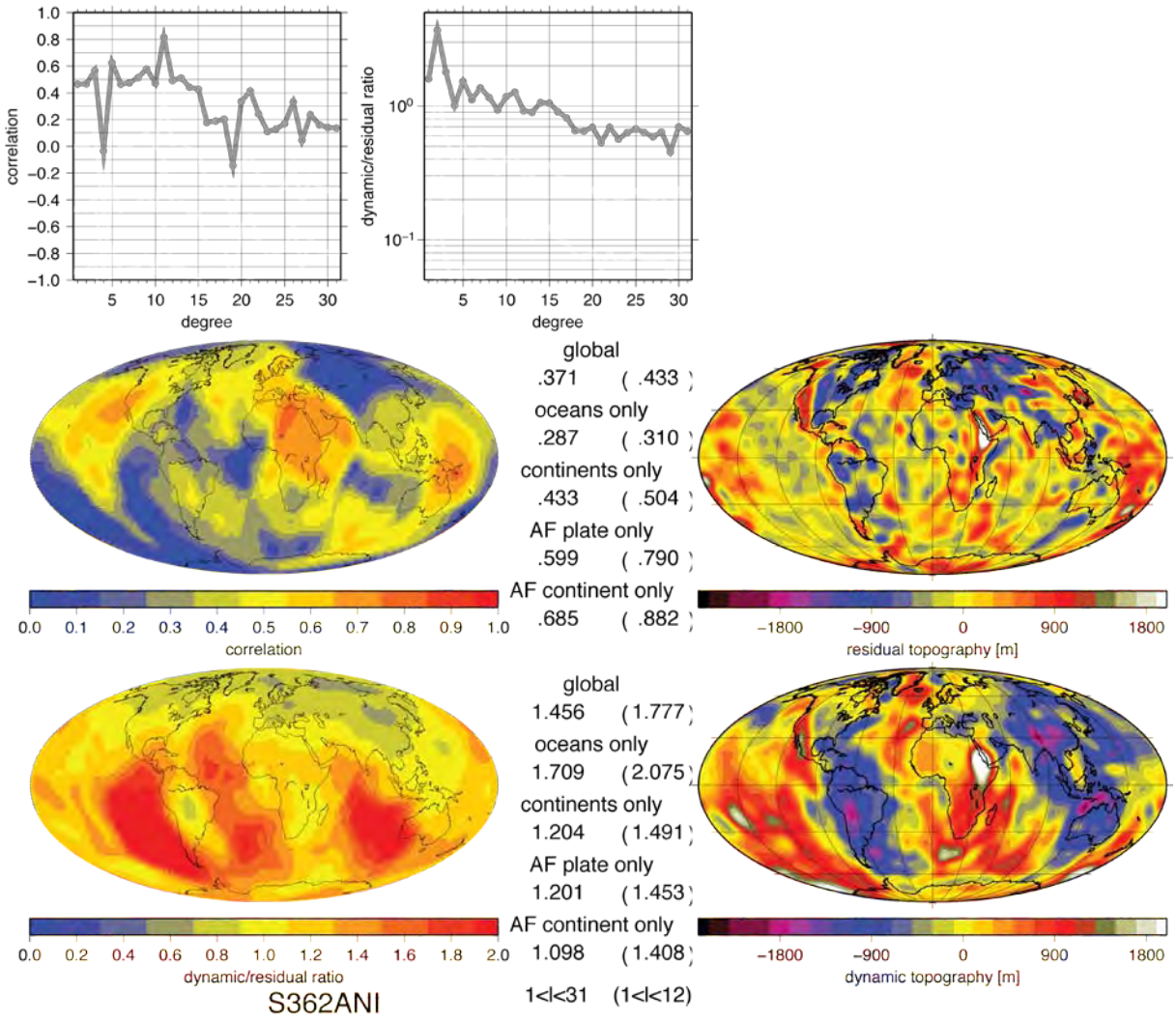

Figure S6: Results for the correlation and ratio between dynamic topography (computed based on tomography model S362ANI) and residual topography. Cut-off S-wave anomaly 0.4%.

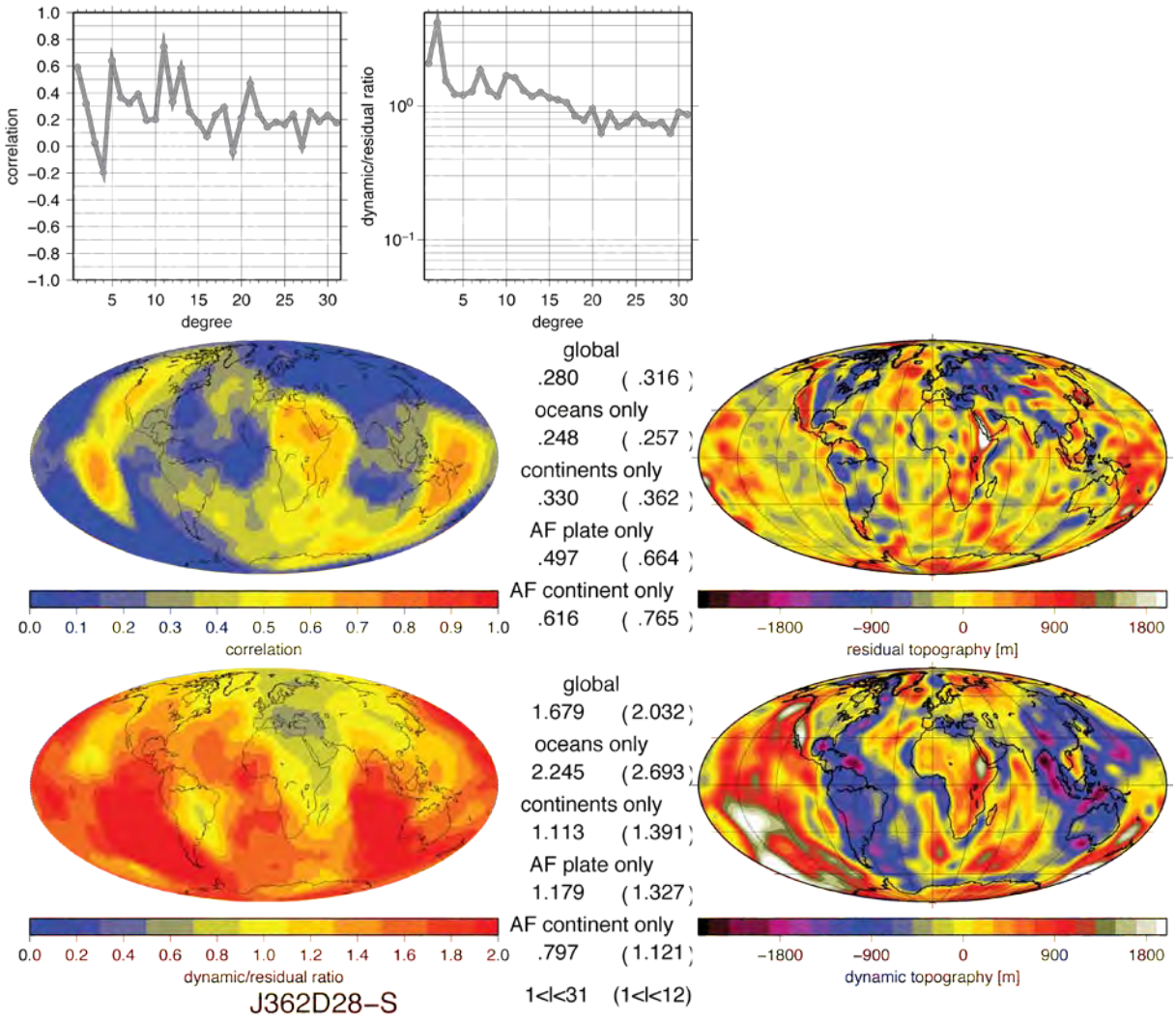

Figure S7: Results for the correlation and ratio between dynamic topography (computed based on tomography model S362D28) and residual topography. Cut-off S-wave anomaly -0.2%.

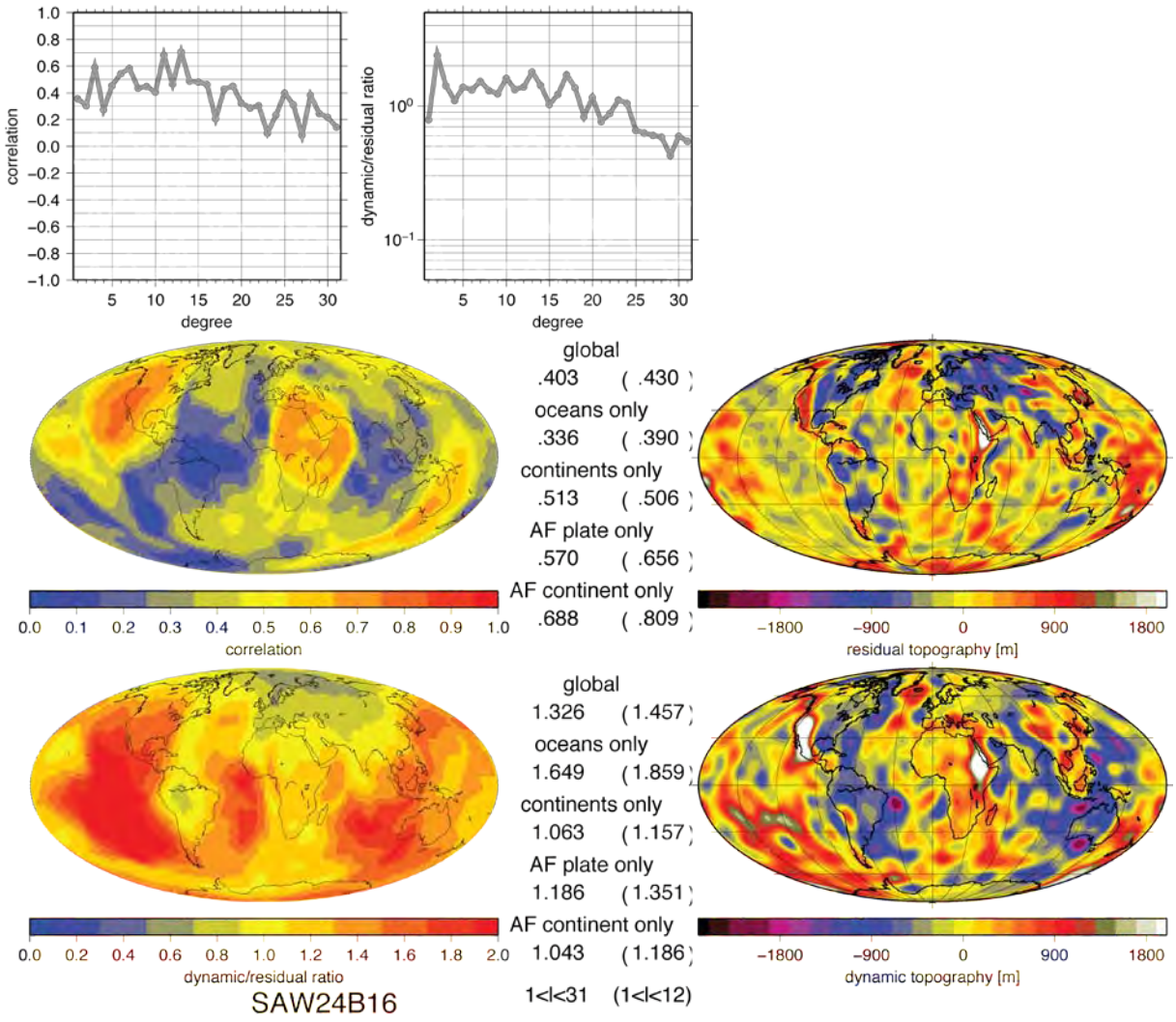

Figure S8: Results for the correlation and ratio between dynamic topography (computed based on tomography model SAW24B16) and residual topography. Cut-off S-wave anomaly 0.6%.

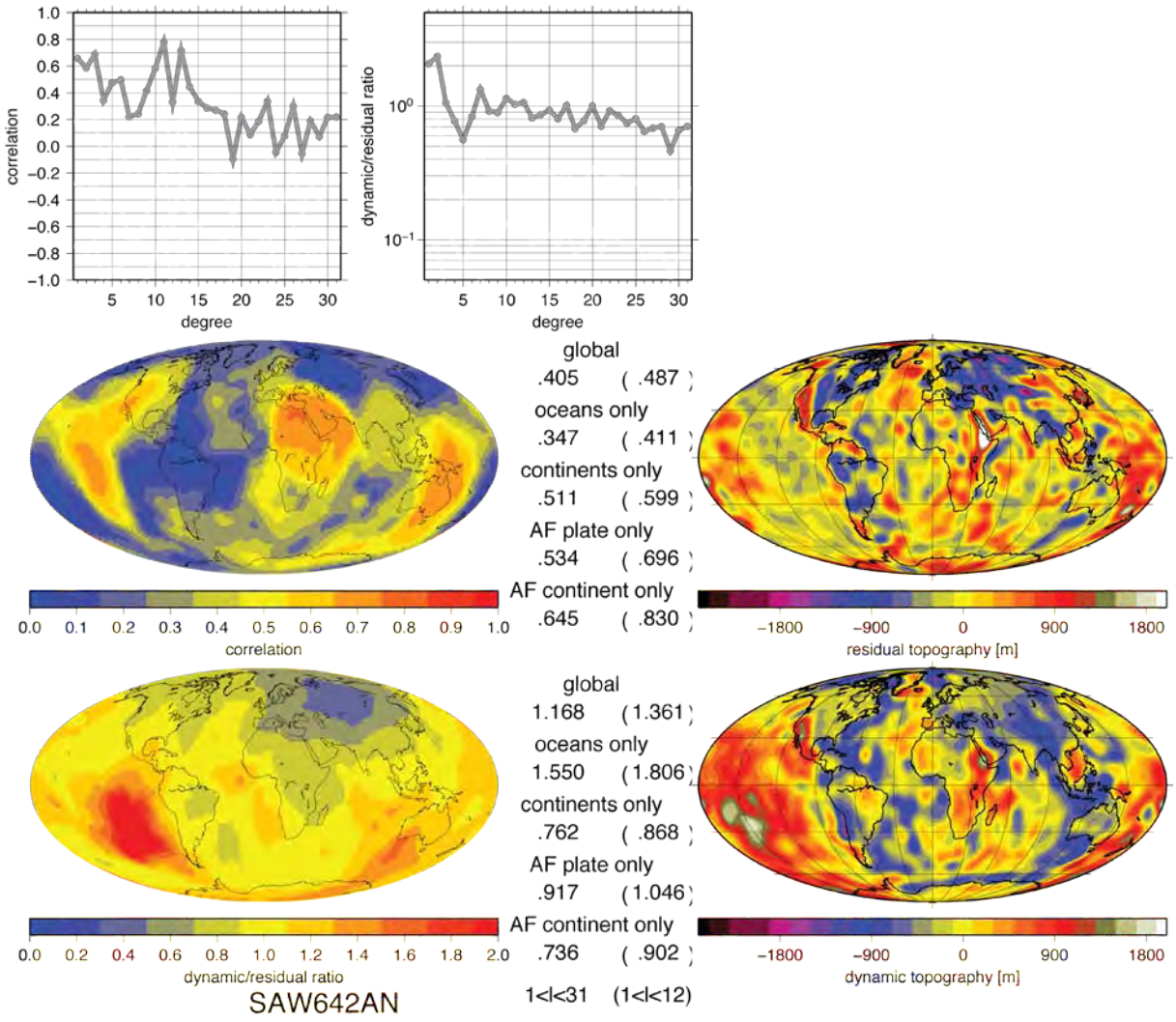

Figure S9: Results for the correlation and ratio between dynamic topography (computed based on tomography model SAW642AN) and residual topography. Cut-off S-wave anomaly 0.5%.

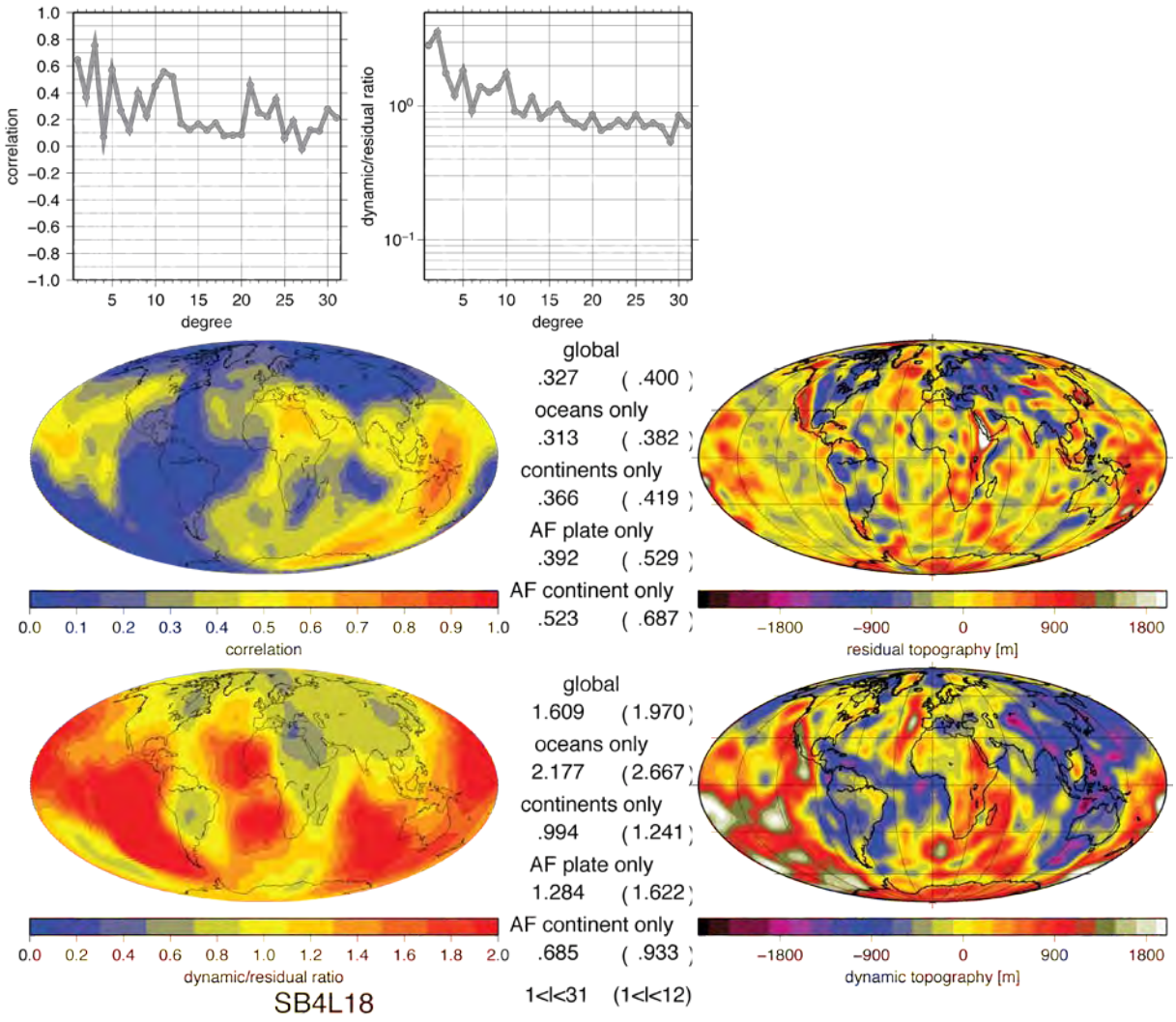

Figure S10: Results for the correlation and ratio between dynamic topography (computed based on tomography model SB4L18) and residual topography. Cut-off S-wave anomaly -0.3%.

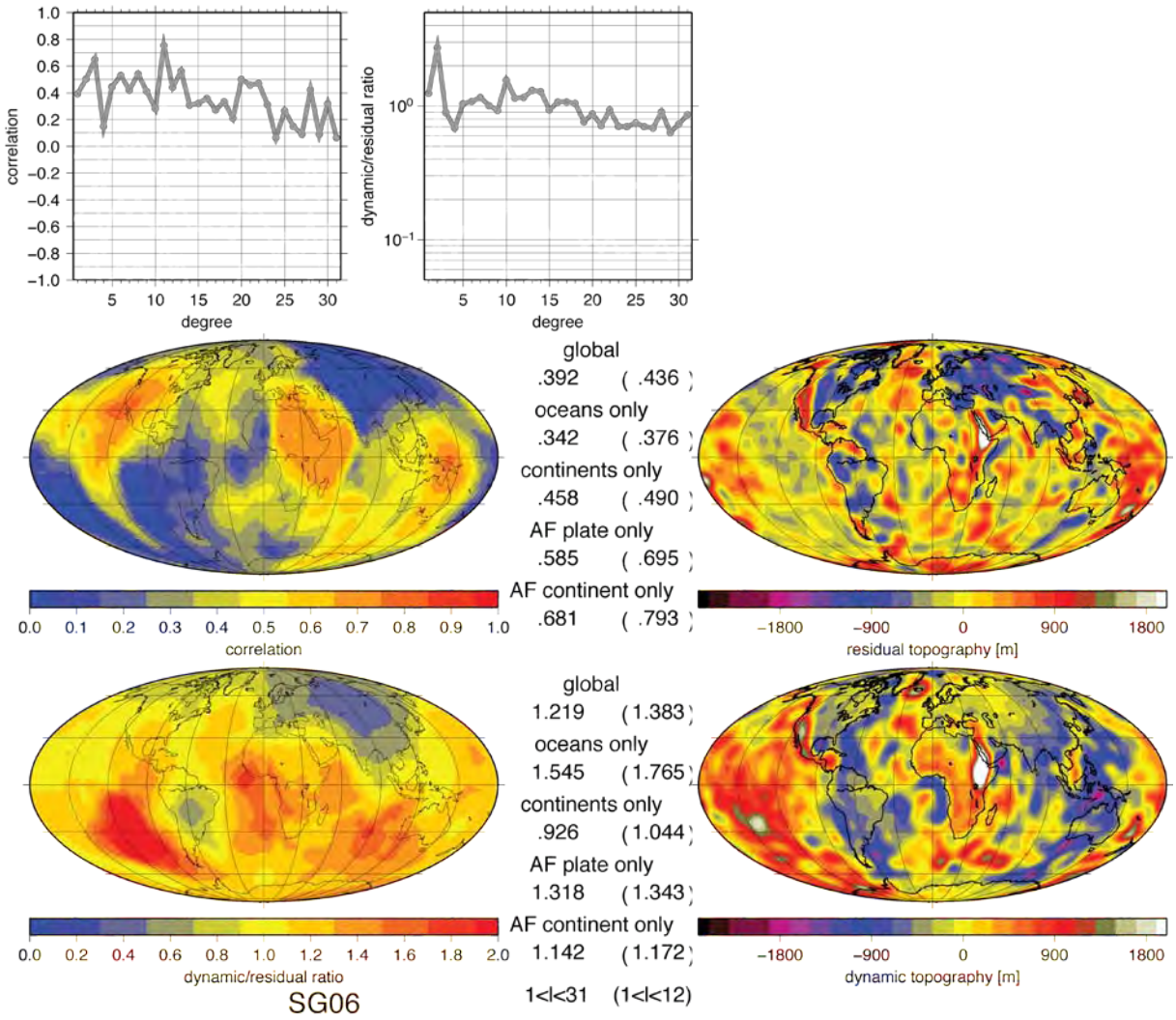

Figure S11: Results for the correlation and ratio between dynamic topography (computed based on tomography model SG06) and residual topography. Cut-off S-wave anomaly 0.1%.

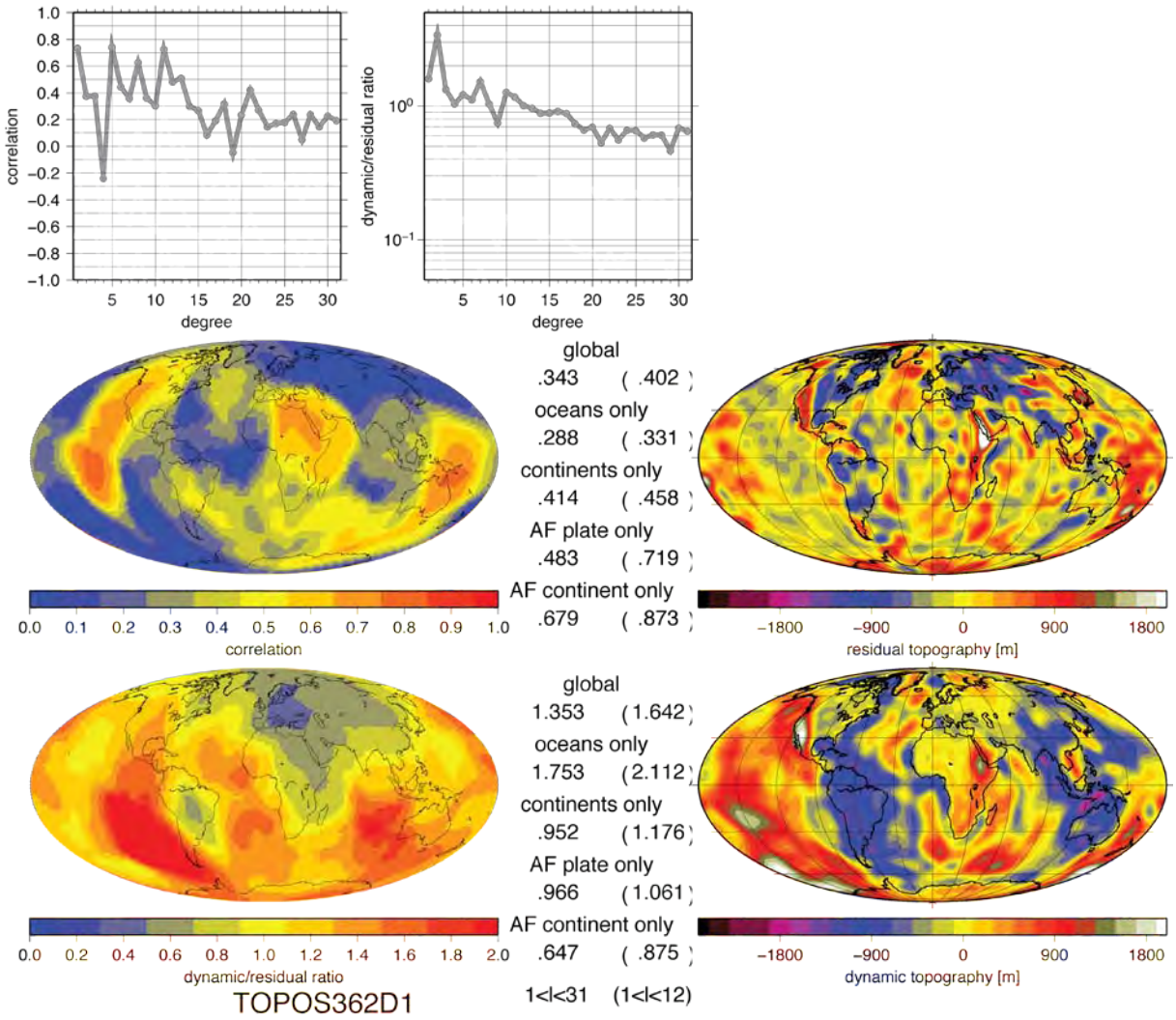

Figure S12: Results for the correlation and ratio between dynamic topography (computed based on tomography model TOPOS362D1) and residual topography. Cut-off S-wave anomaly 0.3%.

APPENDIX C: PRESENT-DAY DYNAMIC TOPOGRAPHY FOR INDIVIDUAL UPPER MANTLE TOMOGRAPHY MODELS

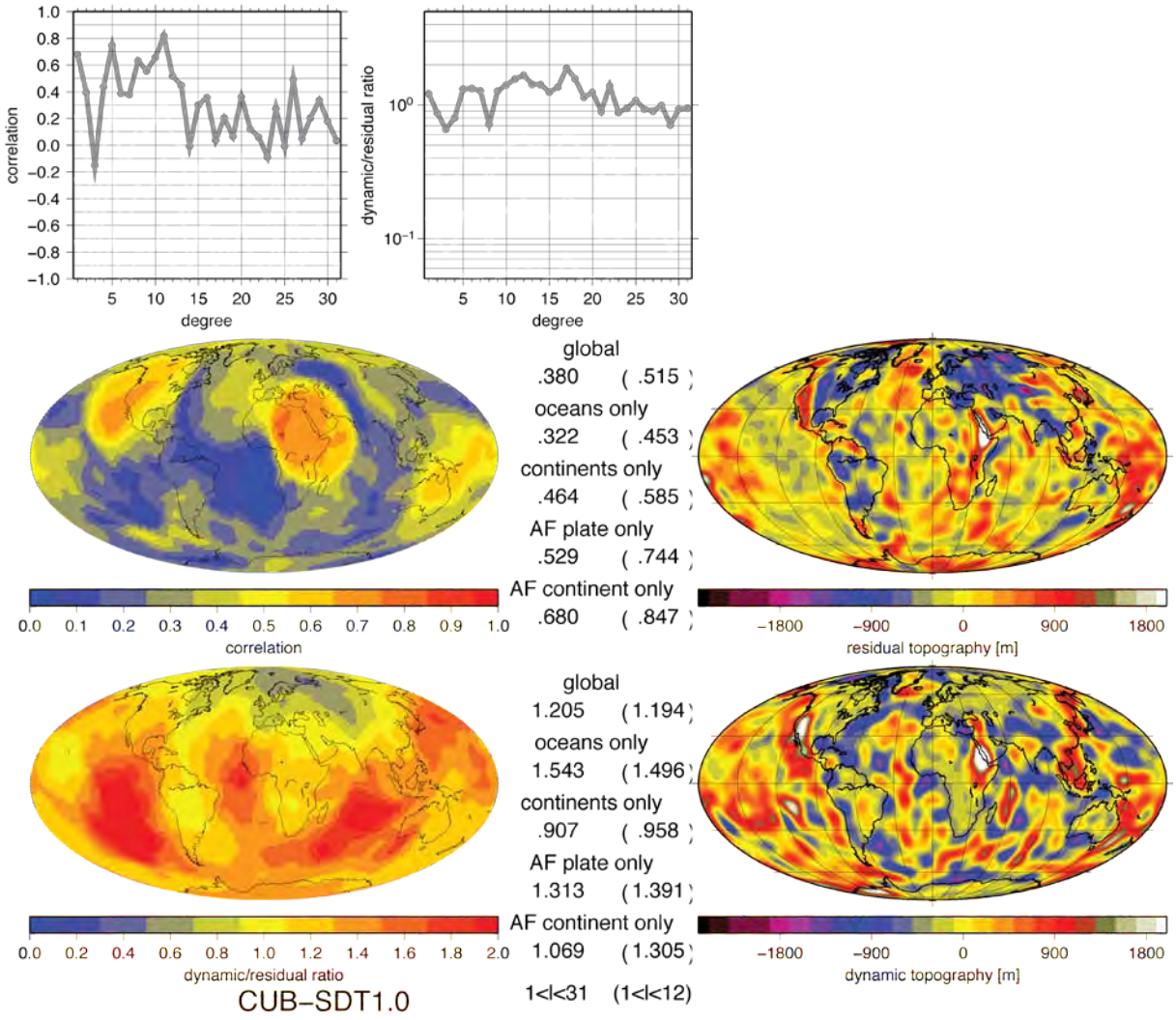

Figure S13: Results for the correlation and ratio between dynamic topography (computed based on tomography model CU_STD1.0 to depth 352 km and zero density anomalies beneath) and residual topography. Cut-off S-wave anomaly 0.3%.

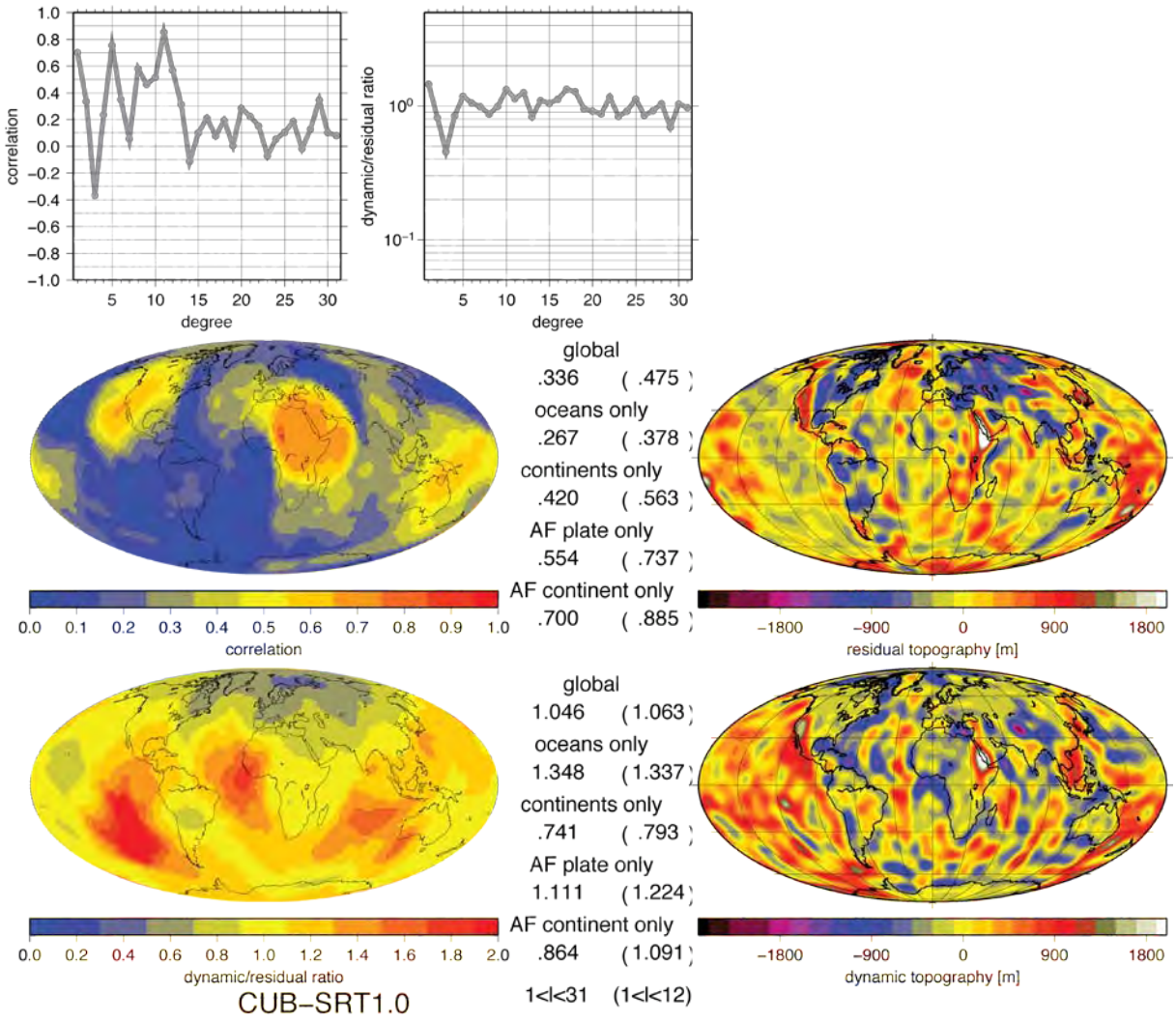

Figure S14: Results for the correlation and ratio between dynamic topography (computed based on tomography model CU_SRT1.0 to depth 352 km and zero density anomalies beneath) and residual topography. Cut-off S-wave anomaly 0.3%.

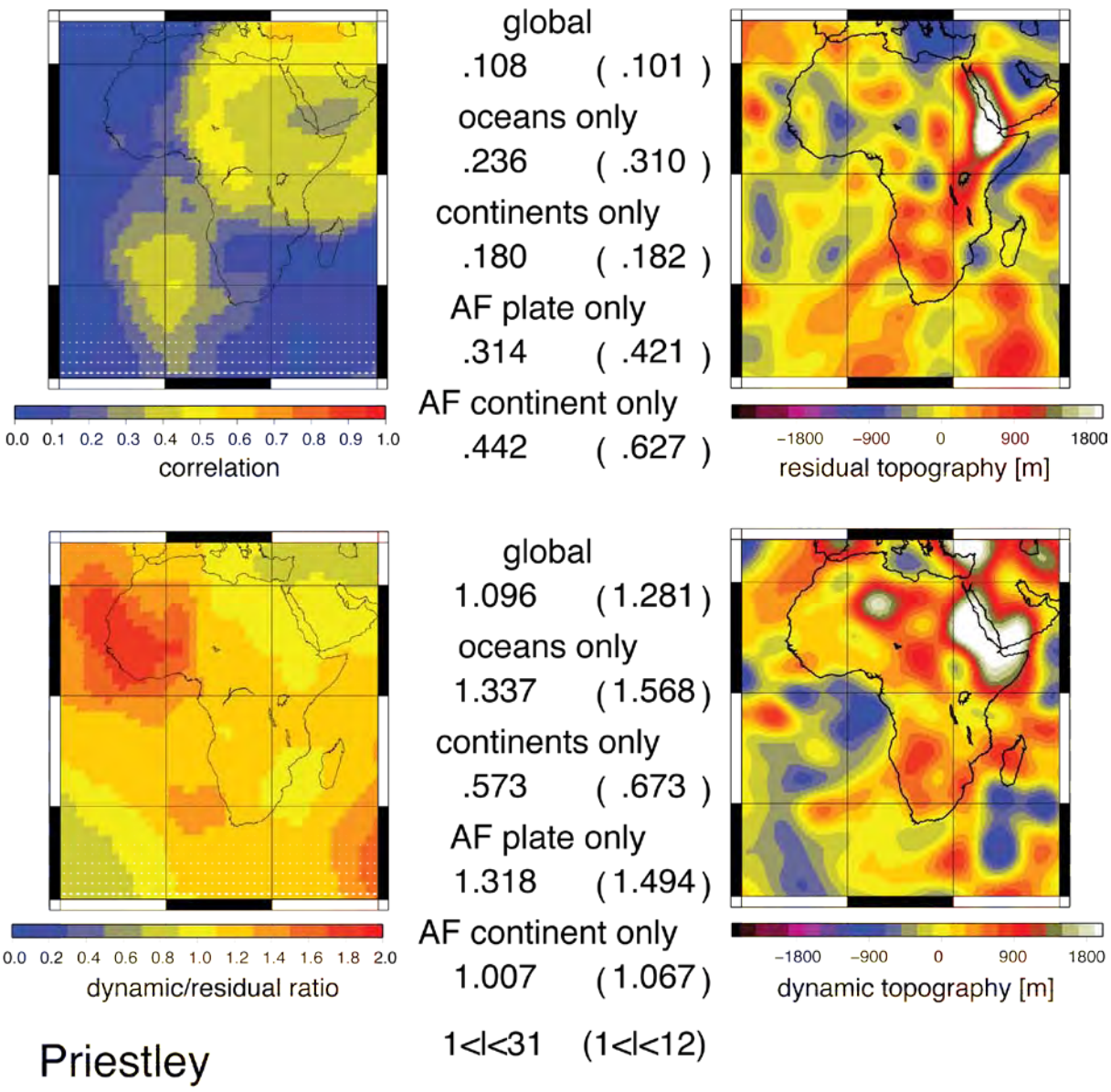

Figure S15: Results for the correlation and ratio between dynamic topography (computed based on tomography model KP08 to depth 400 km and zero density anomalies beneath) and residual topography. Cut-off S-wave anomaly 0.2%.

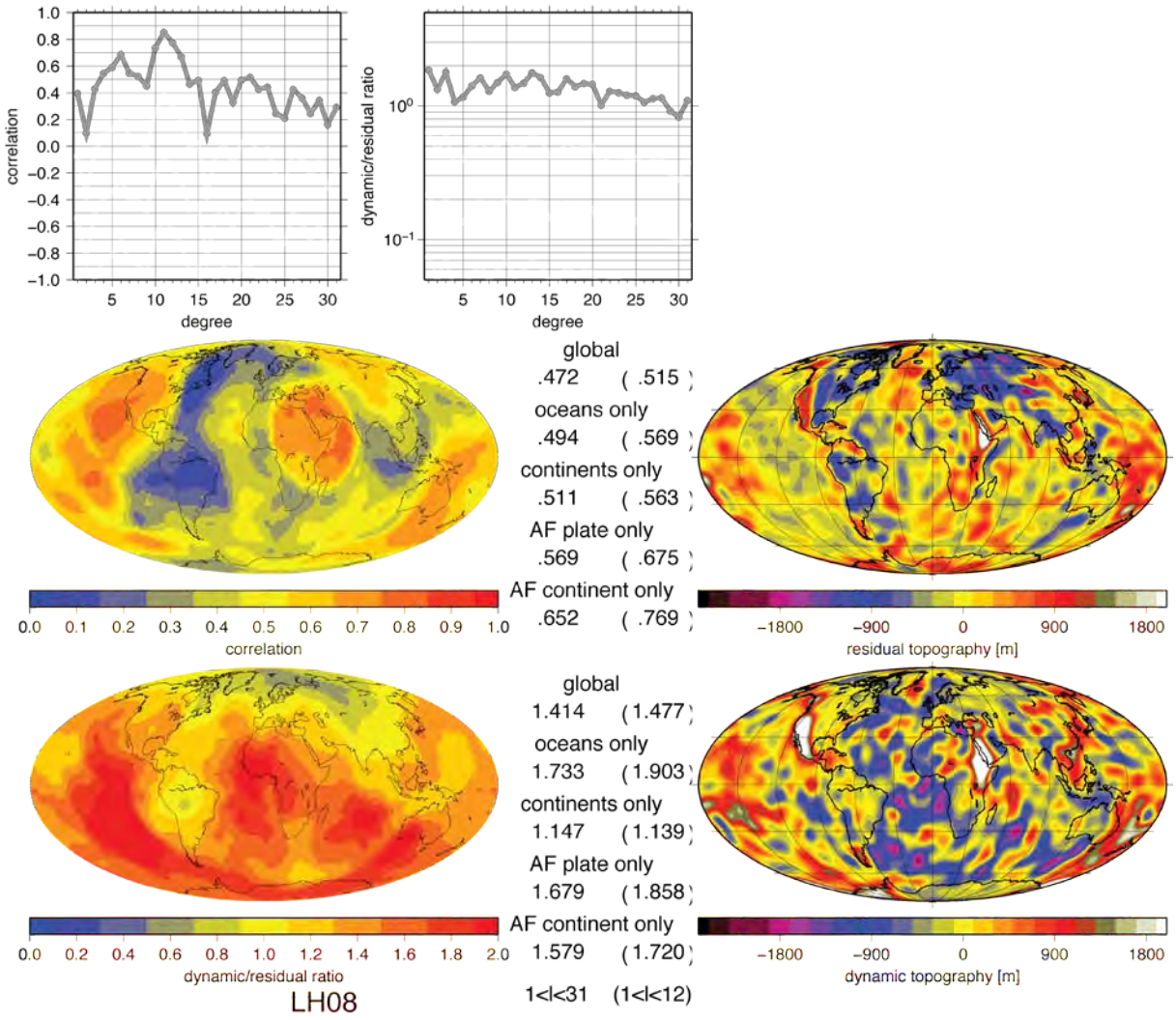

Figure S16: Results for the correlation and ratio between dynamic topography (computed based on tomography model LH08 to depth 660 km and zero density anomalies beneath) and residual topography. Cut-off S-wave anomaly 1%.

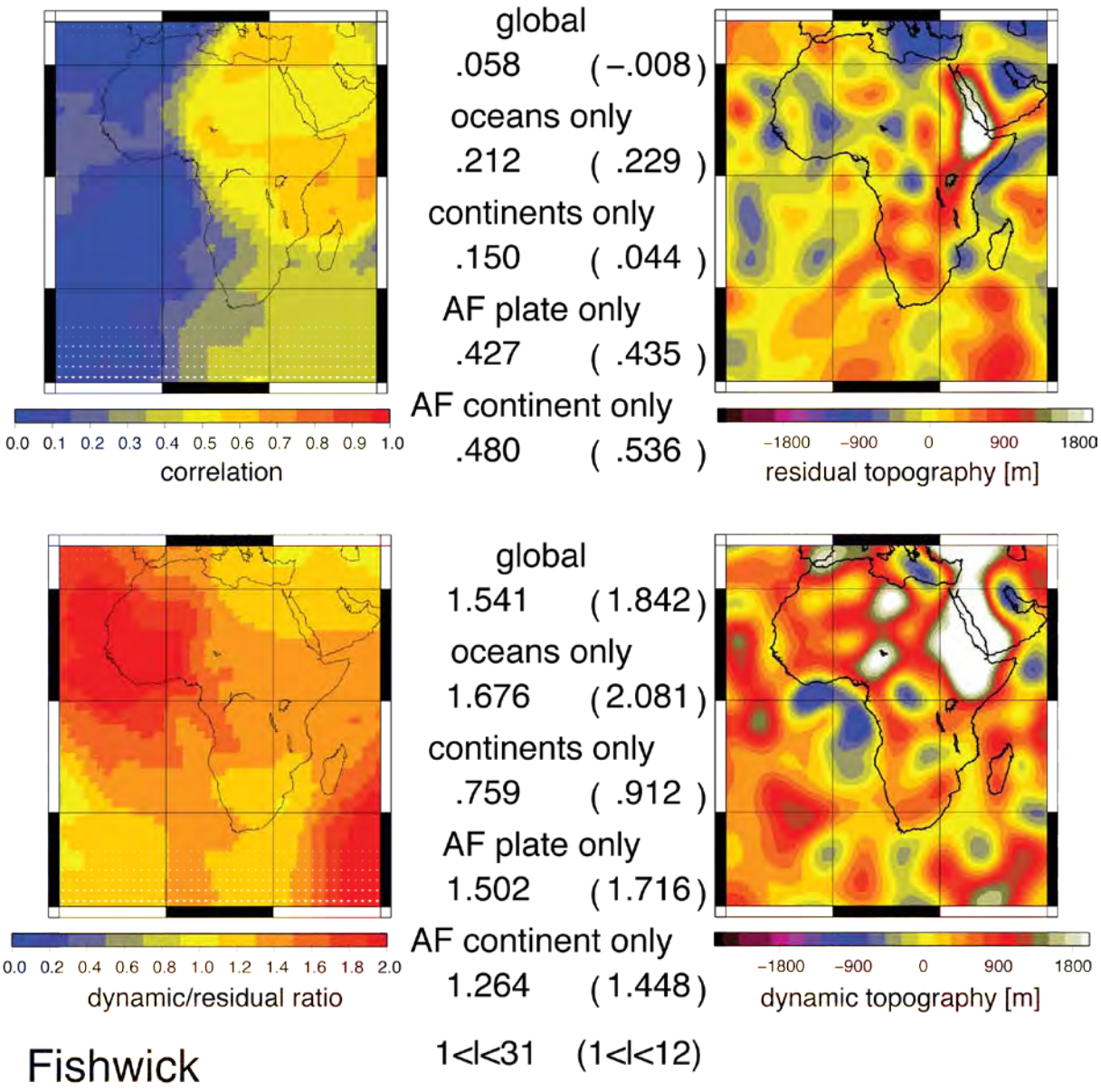

Figure S17: Results for the correlation and ratio between dynamic topography (computed based on tomography model SF09 to depth 250 km and zero density anomalies beneath) and residual topography. Cut-off S-wave anomaly -0.9%.

APPENDIX D: PRESENT-DAY DYNAMIC TOPOGRAPHY FOR ALTERNATIVE LITHOSPHERE AND CRUSTAL MODELS

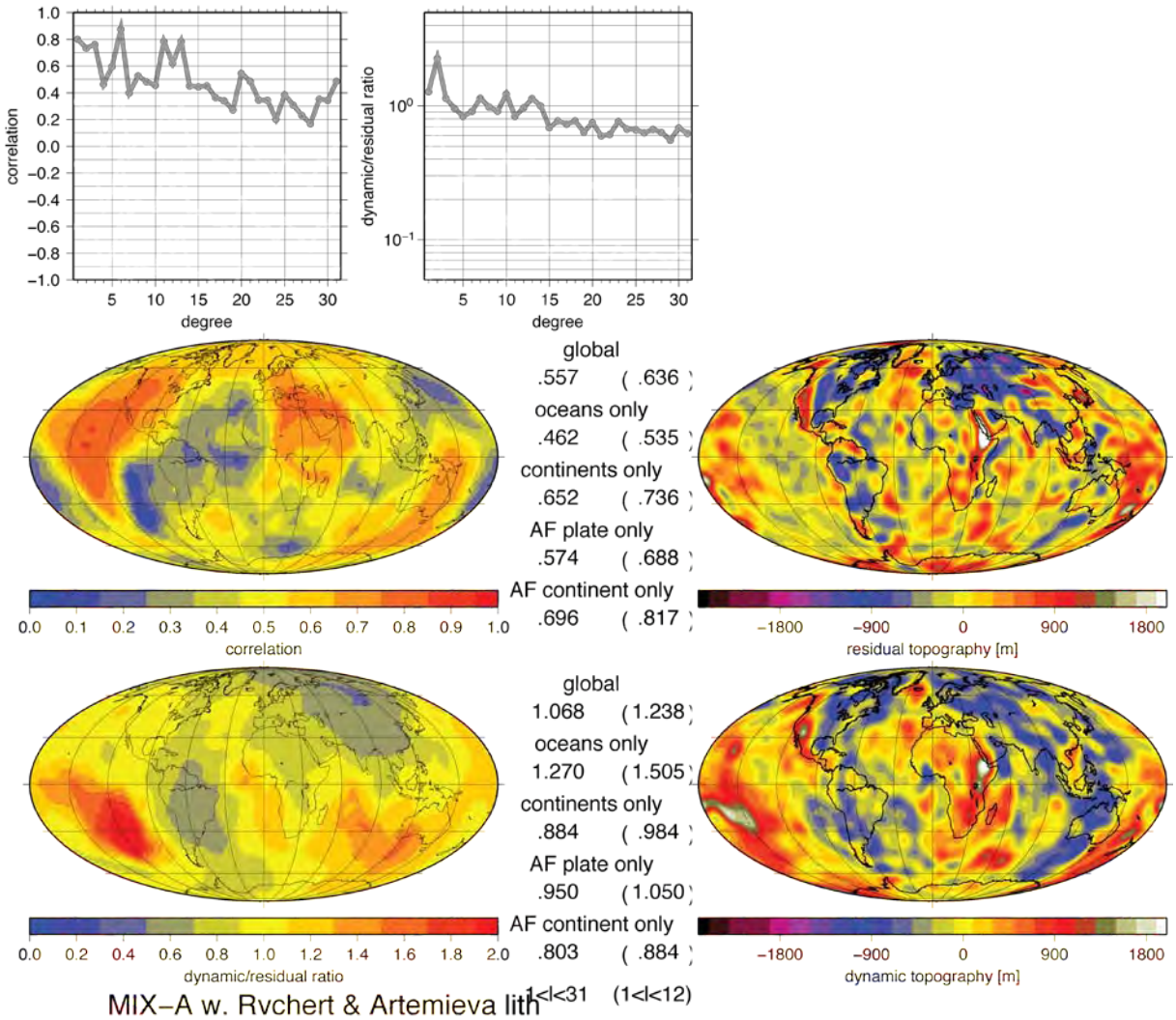

Figure S18: Results for the correlation and ratio between dynamic topography (computed based on the mean tomography model MIX-A) and residual topography. Lithosphere thicknesses from Rychert et al. (2010) are used. Wherever on the continents there is a measurement within 5 degrees, that value is used. Elsewhere on the continents, lithosphere thicknesses from Artemieva (2006) are used; S-wave anomaly is replaced by -0.8% within lithosphere.

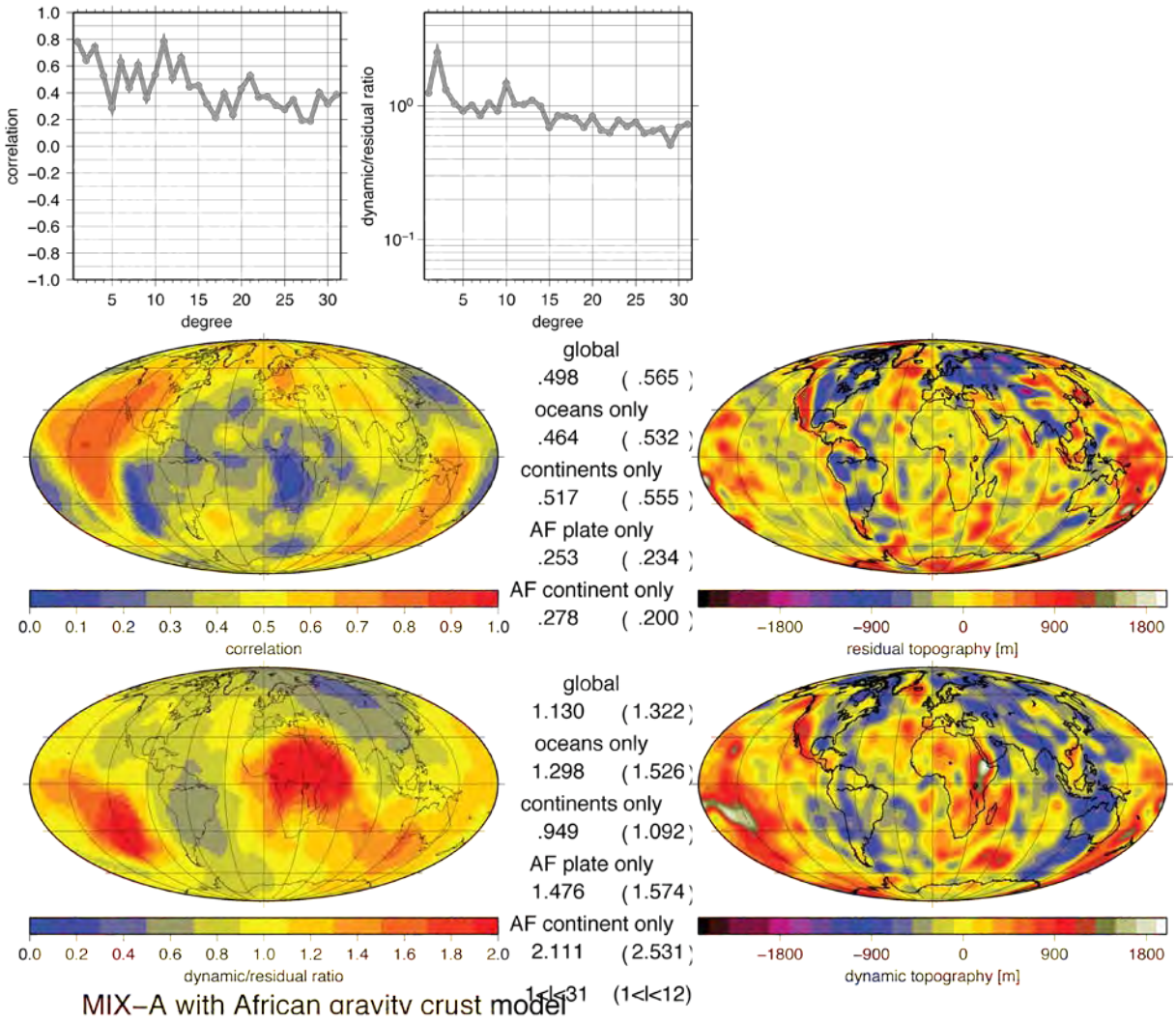

Figure S19: Results for the correlation and ratio between dynamic topography (computed based on the mean tomography model MIX-A) and residual topography. In the Africa region, the crustal model is replaced by a crustal model that is based on gravity inversion (pers. comm. S. Werner). Lithosphere model of Artemieva (2006) is used; S-wave anomaly is replaced by -0.6% within lithosphere.

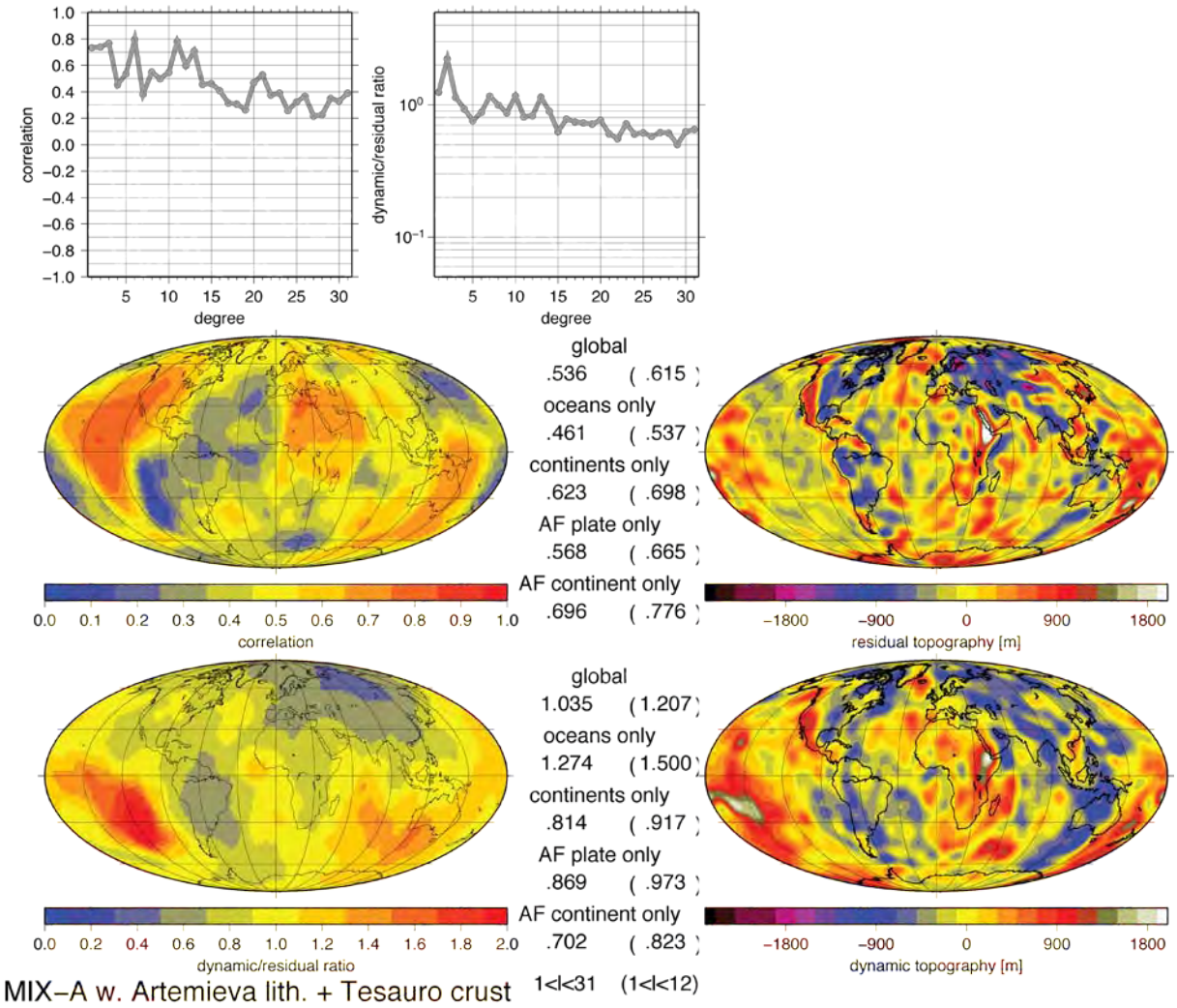

Figure S20: As Fig. 35 but crustal structure in Europe replaced by EuCRUST-07 (Tesauro et al., 2008).